Advances in Fluorescence Lifetime Imaging Microscopy: Techniques and Biomedical Applications

Fangrui Lin[a,#], Chenshuang Zhang[a,#], Zhenlong Huang[a], Yiqiang Wang[a], Min Yi[a], Jia Li[a], Xiaoyu Weng[a,*], Yu Chen[a], Puxiang Lai[b], and Junle Qu[a,*]

AFFILIATIONS

[a]State Key Laboratory of Radio Frequency Heterogeneous Integration; Key Laboratory of Optoelectronic Devices and Systems of Ministry of Education and Guangdong Province; College of Physics and Optoelectronic Engineering, Shenzhen University, Shenzhen, 518060, China

[b]Department of Biomedical Engineering, The Hong Kong Polytechnic University, Hong Kong SAR, China

[*]Corresponding authors. E-mail: xiaoyu@szu.edu.cn; jlqu@szu.edu.cn

[#]These authors contributed equally to this work.

ABSTRACT

Fluorescence lifetime imaging microscopy (FLIM) has emerged as a powerful biomedical imaging technique for the quantitative visualization of intricate molecular and cellular processes. Significant advancements in photonics, sensor technology, data acquisition systems, and computational algorithms have substantially improved the spatiotemporal resolution, imaging depth, and analytical throughput of FLIM. These developments have diversified FLIM methodologies, including time-domain techniques such as time-correlated single-photon counting (TCSPC), time-gated detection, streak cameras, and direct pulse-recording systems, as well as frequency-domain approaches. Concurrently, FLIM has been successfully integrated with advanced imaging modalities, such as multiphoton microscopy, light-sheet imaging, and endoscopy. This review provides a comprehensive synthesis of advanced FLIM technologies. We present in-depth discussions on the principles of lifetime quantification, recent innovations in hardware and algorithms for lifetime recovery, and state-of-the-art strategies to accelerate imaging speed while maintaining resolution and sensitivity. Moreover, we explore FLIM's unique capability to investigate dynamic metabolic states through endogenous autofluorescent cofactors, quantify physicochemical parameters of the cellular microenvironment (e.g., pH, polarity, viscosity, ion concentrations), and facilitate the diagnosis of diseases such as cancer and neurodegeneration. Finally, we discuss future directions for FLIM development, including integration with deep learning, miniaturized hardware for point-of-care applications, and real-time clinical translation. Collectively, this review aims to provide researchers, clinicians, and engineers with both fundamental knowledge and forward-looking perspectives to further unlock the potential of FLIM in advancing biomedical science.

I. INTRODUCTION

Fluorescence has long served as a foundational tool across diverse scientific fields, including cellular biology, materials science, and medical diagnostics. Among fluorescence properties—such as intensity, emission spectrum, and polarization—fluorescence lifetime provides a unique

time-resolved dimension for generating image contrast. Defined as the average time a fluorophore remains in the excited state, the fluorescence lifetime is inversely proportional to the sum of all radiative and non-radiative de-excitation rates. Crucially, as an intrinsic property of the fluorophore, it is independent of concentration, excitation intensity, and photobleaching effect. This robustness makes fluorescence lifetime a highly reliable parameter for quantitative analysis under standardized conditions. As a result, fluorescence lifetime imaging microscopy (FLIM) allows high-specificity visualization of dynamic biological processes, including:

1. Molecular interactions: Such as Förster resonance energy transfer (FRET) through donor/acceptor binding, and collisional quenching[1, 2].

2. Microenvironmental variations: Including pH[3], polarity[4], viscosity[5], mechanical stress[6], refractive index[7], temperature[8], and ion concentrations[9, 10].

3. Conformational dynamics: Including changes in fluorophore conformation[11] or its incorporation within macromolecular complexes[12, 13].

Fluorescence decay occurs on ultrafast timescales, typically spanning picoseconds to nanoseconds, necessitating sophisticated instrumentation and advanced data processing for accurate FLIM measurements. Since its inception in the 1980s, two primary FLIM modalities have been developed: time-domain FLIM, which captures decay kinetics using high-speed timing devices[14, 15], and frequency-domain FLIM, which deduces lifetimes from phase shifts under modulated excitation[16, 17]. Both approaches connect fundamental physical principles with transformative biomedical research, continually advancing through innovations in optoelectronics, algorithmic processing, and deep learning. Given the rapid development and great application potential, several recent reviews of FLIM have been emerged from different perspectives, such as a comprehensive overview[18], high-speed techniques[19, 20], materials science[21], and FRET-analysis in cells[1].

This review provides a comprehensive synthesis of recent methodological developments in FLIM. We begin by elucidating the fundamental principles and comparative instrumental strategies of both time-domain and frequency-domain modalities. We then dedicate core focus to summarizing technical advances in detection systems, excitation methods, and lifetime extraction algorithms, including the pivotal role of artificial intelligence, which have collectively enhanced the performance and versatility of FLIM. To ground these technological innovations in practical utility, we highlight how they unlock novel capabilities in biomedical research, with exemplar applications in probing metabolic activity, mapping microenvironmental parameters, and facilitating disease diagnosis. Finally, we discuss emerging trends such as hardware miniaturization and real-time processing. By integrating cross-cutting technological progress with impactful biomedical demonstrations, this review aims to equip researchers and engineers with a forward-looking perspective on FLIM's evolving potential as a powerful quantitative tool in life sciences and clinical translation.

II. PRINCIPLES OF FLUORESCENCE LIFETIME IMAGING MICROSCOPY

A. Basic Concepts of Fluorescence Lifetime

Fluorescence lifetime (τ) is formally defined as the average duration a fluorophore remains in

the excited state before returning to the ground state. This electronic transition process is characterized by the decay of fluorescence intensity over time $I(t)$, typically described as a mono-exponential function for a single fluorophore:

$$I(t)=I_0 e^{-t/\tau} \quad (1)$$

where I_0 is the initial fluorescence intensity after excitation. As shown in Fig. 1(a), this indicates τ is the time required for I_0 to decrease to I_0/e (approximately 36.8%), and it is independent of the imaging system and fluorophore concentration. In reality, biological samples often contain multiple fluorophores or a single fluorophore in different microenvironments, resulting in multiple lifetimes existing simultaneously. Consequently, equation (1) can be extended to a multi-exponential model:

$$I(t)=\sum_i a_i e^{-t/\tau_i} \quad (2)$$

where a_i represents the amplitude of the i-th component and τ_i is its corresponding lifetime. The average fluorescence lifetime (τ_m) is commonly calculated as[22]:

$$\tau_m=\sum_i a_i \tau_i \quad (3)$$

Overall, fluorescence lifetime offers a comprehensive indicator of fluorescence decay dynamics on a pixel-by-pixel basis, making FLIM a powerful tool for biomedical investigations. Currently, FLIM techniques are divided into two main modalities: time-domain and frequency-domain, each utilizing these lifetime principles in distinct ways.

B. Time-domain FLIM

The most direct way to measure the fluorescence decay curve is through time-domain techniques, which can be implemented in several ways. Time-domain FLIM methods captures the entire temporal profile of fluorescence decay following pulsed excitation, offering lifetime measurements through either time-tagging individual photons or by sampling emission intensity within discrete time intervals. In practice, the detected signal is influenced not only by the intrinsic fluorescence decay of the sample but also by the temporal properties of the system, which are collectively characterized by the instrument response function (IRF). The full width at half maximum of the IRF, denoted as ΔR_{IRF}, encompasses the finite duration of excitation pulses (ΔR_{EX}), the timing jitter of detectors (ΔR_J), and the response time of electronics (ΔR_E), as indicated by[23]:

$$\Delta R_{IRF}^2 = \Delta R_{EX}^2+\Delta R_J^2+\Delta R_E^2 \quad (4)$$

It therefore limits the shortest resolvable lifetime. Mathematically, the measured fluorescence signal $I_{meas}(t)$ can be expressed as the convolution ($\otimes$) between the true fluorescence decay $I(t)$ and the IRF $R(t)$:

$$I_{meas}(t) = I(t)\otimes R(t) = \int_0^t I(t')R(t-t')dt' \quad (5)$$

As illustrated in Fig. 1(b), the IRF-induced broadening of the measured decay necessitates either deconvolution procedures or fitting models that explicitly account for the IRF. Consequently, the accuracy of fluorescence lifetime estimation is highly dependent on the precision of the IRF

characterization; smaller ΔR_{IRF} values enable more precise determination of sub-nanosecond lifetimes. Typically, the IRF is obtained by recording the system's response to a scattered or reflected excitation pulse[24], serving as a crucial reference for fluorescence lifetime analysis.

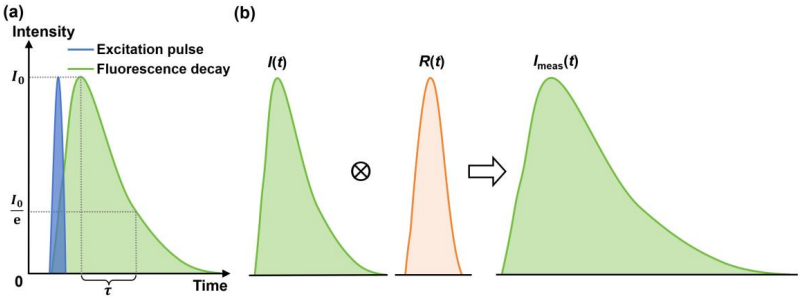

FIG. 1. Schematic illustration of fluorescence lifetime. (a) A fluorescence decay induced by an excitation pulse. (b) A broadened fluorescence decay registered by the measuring system with an instrument response function.

The primary advantages of time-domain FLIM reside in its remarkable temporal precision (attaining the picosecond scale) and uncomplicated interpretability. This is because the decay curve can be directly fitted to mono- or multi-exponential models. In practical applications, for a simple and rapid linear fitting, the least-squares algorithm (LSA) minimizes the squared residuals between the measured decay and IRF-convolved model. However, it presupposes homoscedastic errors and may be suboptimal for photon-counting data following Poisson statistics[25]. The Levenberg-Marquardt algorithm (LMA), a nonlinear least-squares solver, interpolates between gradient descent and the Gauss-Newton method through a damping parameter. It exhibits robustness in regions far from the optimum and rapid convergence in its vicinity[26]. It serves as a commonly employed baseline for intricate models. Maximum-likelihood estimation (MLE) explicitly takes Poisson counting statistics into account and generates statistically efficient estimates with well-founded uncertainty.

Despite the requirement for specialized hardware such as ultrafast detectors and precise timing electronics, time-domain FLIM remains unrivaled in handling complex decay kinetics, quantifying subtle lifetime shifts, and conducting absolute lifetime measurements. Nevertheless, these iterative estimators, in conjunction with hardware limitations, exacerbate a fundamental trade-off between temporal precision and photon throughput. This, in turn, restricts imaging speed and heightens the risk of photobleaching or phototoxicity in live samples.

Based on diverse strategies for acquiring the time-dependent fluorescence intensity decay, we summarize the operating principles of common techniques, including time-correlated single photon counting, time-gated detection, streak camera imaging, and direct pulse-recording.

1. Time-correlated single-photon counting (TCSPC)

Time-correlated single-photon counting (TCSPC) is extensively acknowledged as the preeminent technique for FLIM owing to its remarkable temporal precision, high photon efficiency, and well-established hardware accessibility. In a conventional TCSPC-FLIM configuration, a pulsed laser source excites the sample via a scanning microscope. The emitted

fluorescence photons are collected by a single-point detector, such as a photomultiplier tube (PMT) or avalanche photodiode (APD). The detected photons are time-stamped in relation to their corresponding excitation pulses utilizing a time-to-digital converter (TDC). Aggregating these timestamps across numerous excitation cycles yields a photon arrival time histogram, which directly depicts the fluorescence decay profile [Fig. 2(a)]. Contemporary detectors and electronics, distinguished by low temporal jitter, allow for the IRF width of less than tens of picoseconds, enabling reliable lifetime measurements down to several tens or hundreds of picoseconds[27].

Historically, a crucial limitation of TCSPC-FLIM is its comparatively low frame rate. Frequently, it takes seconds to minutes to acquire a megapixel image. This issue predominantly arises from strict photon count rate limitations. Detection modules generally have a dead time on the order of tens of nanoseconds. This implies that only the first photon arriving within each signal period can be recorded, while subsequent photons are disregarded. To alleviate photon pile-up artifacts, which distort the recorded photon histogram by under-counting later-arriving photons, the photon count rate should ideally be kept below 5-10% of the laser repetition rate[25]. Moreover, accurate multi-exponential fitting typically requires the detection of approximately 1000 photons per pixel. This compels TCSPC-FLIM implementations to rely on either repetitive scanning protocols or extended pixel dwell time. This inherent trade-off between temporal precision and imaging speed has long been a defining challenge for TCSPC-FLIM, constraining its applicability in scenarios that demand high-throughput or the imaging of fast-changing dynamics.

2. Time-gated (TG)

TG-FLIM is a typical wide-field lifetime measurement technique that determines fluorescence decay kinetics by recording emission intensity within precisely defined temporal windows following pulsed excitation[28]. In this method, a high-repetition-frequency pulsed light source excites the sample, and a gated array-detector is synchronized to collect fluorescence at controlled time delays after each excitation pulse [Fig. 2(b)]. Through the sequential adjustment of the gate delay and the acquisition of a series of intensity images, the temporal evolution of the decay curve can be reconstructed for each pixel.

Two critical temporal parameters delineate the operation of TG-FLIM: the gate delay, which specifies the temporal offset of each gate from the excitation pulse, and the gate width, which represents the effective exposure time of the detector. Narrow gate widths allow finer temporal discrimination; however, they necessitate a higher photon flux to maintain lifetime precision. In principle, the rapid determination of the lifetime for a mono-exponential decay only requires two images acquired at different gate delays with intensities I_1 and I_2, and the fluorescence lifetime can be derived according to the formula[29]:

$$\tau = \frac{t_2 - t_1}{\ln(I_1/I_2)} \tag{6}$$

The temporal resolution of TG-FLIM is ultimately limited by the minimum achievable gate width and the timing jitter of the gating electronics. Given that only a fraction of the emission is recorded in each gate, photon efficiency declines unless compensated by incorporation more gates, which comes at the expense of acquisition speed and data volume. Nevertheless, TG-FLIM benefits from parallel full-field acquisition, making it one of the fastest FLIM modalities.

3. Streak camera

Streak cameras operate by converting the temporal profile of fluorescence emission into a spatial intensity distribution on a two-dimensional (2D) detector, typically allowing an exceptional temporal resolution of a few picoseconds. As shown in Fig. 2(c), photons originating from a line within the sample strike the photocathode through a slit, generating photoelectrons that are subsequently accelerated by an electric field. A rapidly varying deflection voltage sweeps these electrons transversely across a microchannel plate (MCP) and phosphor screen, with the resulting optical signal recorded by a charge coupled device (CCD) or scientific complementary metal oxide semiconductor (sCMOS) camera. This process encodes the photon arrival time relative to the excitation pulse along one axis in a single measurement, while simultaneously mapping spatial position along the orthogonal axis, producing a time-space image of the fluorescence decay[30]. In general, its temporal precision is highly sensitive to instrumental time jitter and space-charge effects during electron deflection[31]. Consequently, streak camera-based FLIM (SC-FLIM) methods are well suited for capturing transient phenomena[32], but it is limited by the need for line-by-line scanning, bulky and expensive instrumentation, and artifacts such as space-charge effects and timing jitter, which restrict its practicality for routine or *in vivo* imaging.

4. Direct pulse-recording (DPR)

DPR-FLIM belongs to a unique category of time-domain techniques. It is characterized by the direct acquisition of the complete fluorescence decay waveform subsequent to each excitation pulse, utilizing high-speed electronics[33, 34]. This approach obviates the necessity for time-consuming photon counting, intricate time gating, and expensive streak cameras. A high-bandwidth digitizer (typically in the GHz order) is utilized to sample the analog transient fluorescence signal produced by photodetectors, such as a PMT, MCP-PMT, or APD. The sampling interval is determined by the overall system bandwidth [Fig. 2(d)].

DPR-FLIM enables exceptionally high photon detection rates, reaching up to hundreds of MHz. Consequently, it is highly suitable for biomedical applications that demand high frame rates and real-time visualization of lifetimes. Nevertheless, it is accompanied by the drawback of inferior temporal resolution, typically exceeding 1 ns. This is primarily restricted by the response times of the detector and amplifier.

Moreover, the analog front-end is inherently more susceptible to thermal noise, baseline drift, and sampling jitter. All these factors can significantly deteriorate lifetime precision, especially under photon-scarce conditions, such as autofluorescence imaging. These limitations can be alleviated through meticulous radio frequency (RF) shielding, frame averaging, and increasing pixel dwell time or excitation power. However, these measures may potentially cause light damage and reduce frame rates in biological imaging.

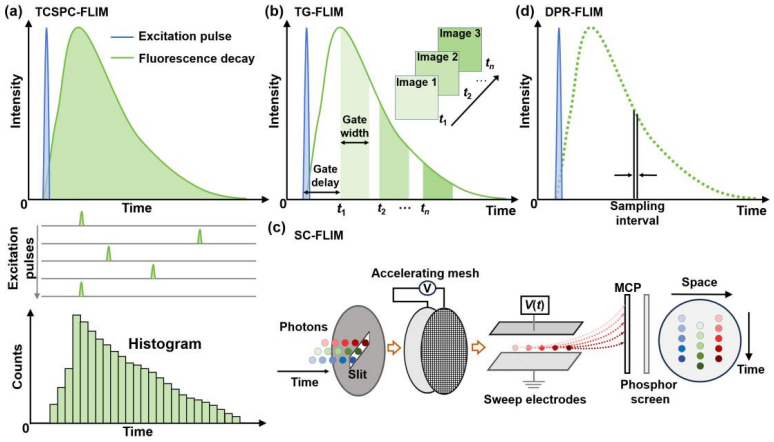

FIG. 2. Schematic illustration of the fundamental principles of time-domain FLIM methods. (a) Time-correlated single-photon counting (TCSPC) FLIM: A pulsed laser excites the sample. For each detected photon (e.g., via an APD or PMT), a time-to-digital converter (TDC) measures its arrival time relative to the corresponding excitation pulse. A histogram of these arrival times, built over thousands to millions of pulses, directly represents the fluorescence decay curve. (b) Time-gated (TG) FLIM: The excitation pulse triggers a gated detector. The detector is activated only during a brief, precisely delayed time gate. By recording the intensity images at multiple delay times (t_1, t_2, ... t_n), the fluorescence decay is sampled and reconstructed for each pixel. (c) Streak camera (SC) FLIM: Photons from a line in the sample are focused onto a photocathode via a slit. The generated photoelectrons are deflected by a rapidly varying electric field, converting their arrival time into a spatial displacement on a 2D detector. The resulting image encodes one spatial dimension along the slit and time along the deflection axis, capturing the entire decay profile across the line in a single shot. (d) Direct pulse-recording (DPR) FLIM: The analog fluorescence signal from a detector is digitized at high speed (GHz-order sampling rate) following each excitation pulse with settled sampling interval. The complete transient waveform is captured directly.

C. Frequency-domain FLIM

While time-domain FLIM captures the complete decay kinetics following pulsed excitation, frequency-domain FLIM offers a complementary approach by deducing lifetimes under modulated excitation. Fluorescence emission closely follows the excitation waveform but exhibits a reduced amplitude and a distinctive phase delay. Based on this principle, frequency-domain FLIM typically encodes lifetime information by sinusoidally modulating the excitation source and measuring the corresponding phase shift and demodulation in the emission[16], rather than recording the complete fluorescence decay profile.

For a fluorophore with lifetime τ excited at modulation frequency ω, the emission shows a delayed phase φ relative to the excitation and a reduced modulation depth M [Fig. 3(a)], which are quantitatively related as follows[35]:

$$\tau_M = \frac{\sqrt{(1/M^2\text{-}1)}}{\omega} \tag{7}$$

$$\tau_\varphi = \frac{\tan\varphi}{\omega} \tag{8}$$

$$M = \frac{(b/B)}{(a/A)} \tag{9}$$

Here, τ_M and τ_φ represent the lifetimes derived from modulation and phase measurements, respectively. For a single fluorophore in a homogeneous microenvironment, the fluorescence decay is ideally mono-exponential, resulting in $\tau_M = \tau_\varphi$. However, in biologically complex samples, it is common to observe $\tau_M \neq \tau_\varphi$. This discrepancy is a definitive indicator of a multi-exponential decay, signifying the presence of multiple distinct fluorescent species or a single fluorophore populating different microenvironments within the measurement volume. The physical origin of this inequality lies in the different weighting of the underlying lifetime components (τ_i) in the phase and modulation measurements. The τ_φ is disproportionately sensitive to components with shorter lifetime, while the τ_M is more heavily influenced by components with longer lifetime. Therefore, in a heterogeneous system, a single-frequency measurement yields two different apparent lifetimes, neither of which accurately represents the true kinetic landscape. This fundamental limitation means that analyzing data from a complex decay using a mono-exponential model can lead to misinterpretation of the sample's composition and physicochemical state. To overcome this and achieve accurate quantification, advanced strategies are required. These include performing measurements at multiple modulation frequencies to sample the decay kinetics more comprehensively or employing the model-free phasor analysis, which graphically resolves heterogeneous decays without prior assumptions about the number of components.

In practical implementations of frequency-domain FLIM, efficient excitation is achieved by modulating a laser or light-emitting diode (LED) at specific frequencies, typically ranging from tens to hundreds of MHz[36, 37]. Fluorescence emission is detected by either single-point detectors or array detectors[38, 39], depending on the spatial resolution and speed requirements. To extract lifetime information from the modulated fluorescence signal, a range of demodulation strategies are employed.

For wide-field imaging, a common approach involves the use of a gain-modulated image intensifier coupled to a CCD or CMOS camera. In this setup, the photocathode gain of the intensifier is driven by a radio-frequency signal that is synchronized with a controllable phase offset to the excitation source. This performs homodyne detection, converting the temporal phase delay into a spatial intensity pattern. To reconstruct a lifetime map, a series of intensity images are captured at different phase offsets between the excitation and detection modulations. The τ_M and τ_φ are then calculated pixel-wise from these images. As an alternative to homodyne detection, heterodyne detection can be employed, particularly in specialized applications requiring high phase-measurement precision. In this implementation, the detector is modulated at a frequency slightly offset from the excitation (e.g., $\omega + \Delta\omega$). This mixing process down-converts the high-frequency phase information into a low-frequency beat signal at $\Delta\omega$, which can be measured with high accuracy using standard electronics. However, due to its increased system complexity and sequential data acquisition nature, heterodyne detection is less commonly implemented in wide-field FLIM compared to the more straightforward homodyne approaches.

For point-scanning systems, alternative electronic demodulation is used. Conventional analog

methods, such as lock-in amplifiers or analog mixing circuits, directly multiply the PMT output with a reference signal in the electronic domain. The mixed signal is passed through a low-pass filter to output a DC level proportional to the phase shift. While this offers direct, real-time demodulation at each scanning point, the process is inherently sequential and can be susceptible to electronic drift and noise. In contrast, modern digital methods provide enhanced robustness and flexibility. The analog signal from the detector is first digitized by a high-speed analog-to-digital converter (ADC). Demodulation is then performed either via a field-programmable gate array (FPGA), which can implement a digital lock-in detection algorithm in parallel for high-speed real-time processing, or by applying discrete Fourier transforms (DFT) to the acquired waveform to directly extract the phase and amplitude information at the modulation frequency.

Lifetime-contrast images can also be generated without iterative fitting using the phasor approach. This model-free analysis maps the phase φ and modulation M of each pixel to phasor coordinates (g, s) in the complex plane according to[40]:

$$g = M\cos\varphi \tag{10}$$

$$s = M\sin\varphi \tag{11}$$

Each point in the resulting phasor plot corresponds to the harmonic response of the fluorescence decay at modulation frequency ω. As illustrated in Fig. 3(b), for a mono-exponential decay with lifetime τ_{mono}, the phasor coordinates lie on a universal semicircle defined by:

$$s^2+(g-0.5)^2 = 0.25 \tag{12}$$

The position along the semicircle depends solely on the product of ω and τ_{mono}. This geometric representation allows immediate visualization of lifetime distributions. For mixtures of fluorophores or multi-exponential microenvironments, phasors lie along straight lines (chords) connecting individual components, with the position along the chord reflecting the fractional contribution of each component.

Thus, the phasor approach provides not only a rapid, non-fitting method for generating lifetime contrast but also a powerful tool for resolving heterogeneous decay kinetics and quantifying species fractions within each pixel without prior assumptions about the number of components or computationally intensive fitting[40-42]. As a result, frequency-domain FLIM is compatible with both wide-field and scanning imaging modalities, even with short pixel dwell times, making it particularly suitable for studying dynamic changes in fluorophore properties or real-time biomedical processes[35, 43-47].

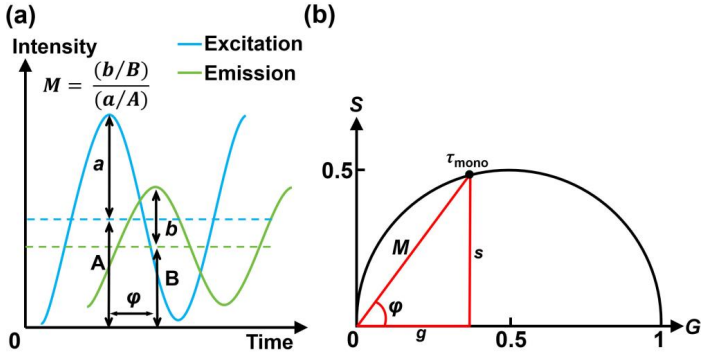

FIG. 3. Schematic representation of frequency-domain FLIM principles. (a) Phase shift and

demodulation between excitation and emission waveforms. The excitation light is intensity-modulated at a high frequency (ω). The resulting fluorescence emission is modulated at the same frequency but is delayed in phase by an angle (φ) and exhibits a reduced modulation depth (M). These parameters are quantitatively related to the fluorescence lifetime. (b) Phasor plot representation of lifetime data. Each measurement pixel is mapped onto a polar plot using coordinates (g, s). A mono-exponential decay maps onto a point on the universal semicircle.

III. ADVANCEMENTS IN DIVERSE FLUORESCENCE LIFETIME IMAGING MICROSCOPY TECHNIQUES

Building upon the fundamental principles of time-domain and frequency-domain FLIM outlined earlier, recent years have witnessed significant technological breakthroughs aimed at overcoming their traditional limitations in speed, sensitivity, and applicability. Over the past decades, continuous progress in instrumentation and computational methods has pushed each FLIM modality beyond its initial constraints, leading to systems that are faster, more versatile, and better suited to a wide range of experimental conditions. Notably, these advances have not followed a uniform path but have evolved in a modality-specific manner, yielding tailored solution for each type of FLIM technique. In the following subsections, we provide a detailed overview of these developments, highlighting how each methodological branch has evolved into more powerful and flexible imaging tools that broaden the scope of biomedical and clinical applications.

A. Advancements in TCSPC-FLIM

Although TCSPC provides a robust framework for fluorescence lifetime quantification, its conventional implementations have been hampered by limited photon throughput and slow acquisition speeds, restricting its use in dynamic or large-scale biomedical imaging. To address these inherent challenges, multiple technical innovations have been introduced. On the hardware side, improvements in detector design and timing electronics have substantially enhanced photon efficiency, timing accuracy, and parallel detection capabilities. Meanwhile, novel scanning strategies have been developed to accelerate image acquisition without compromising spatial or temporal resolution. Advances in algorithms are equally important, including model-based optimization and deep learning (DL) approaches, which enable reliable lifetime extraction under low-photon conditions and support real-time processing. Together, these developments are transforming TCSPC-FLIM into a high-throughput, adaptable technology capable of addressing applications previously limited by speed or photon availability.

1. Hardware

A direct strategy for increasing frame rates involves reducing the detector module's dead time, thereby improving the detection duty cycle. Recent advances in single-photon detection have led to the development of various low-latency detectors that significantly enhance photon throughput and imaging speed[48]. For instance, hybrid photomultiplier tubes (PMTs) are widely adopted in confocal laser scanning microscopes (CLSM) due to their extremely short dead time (<1 ns), high quantum efficiency of GaAsP cathodes[49], and negligible afterpulsing[50]. Coupling a hybrid PMT with a data acquisition card featuring similarly short dead time (e.g., TimeHarp 260 Nano,

PicoQuant GmbH) enables a method known as rapidFLIM. As illustrated in Fig. 4(a), this technique allows recording multiple photons within a single excitation pulse period, achieving photon count rates up to 40 MHz. Although rapidFLIM exhibits a slightly reduced temporal resolution (~250 ps) compared to conventional systems, it supports frame rates of up to 20 frames per second (fps) for regions of interest (ROIs) with 64×64 pixels[51]. By leveraging modern field-programmable gate array (FPGA) technology to implement a direct time-to-digital converter (TDC) architecture—replacing conventional constant fraction discriminators—Wahl et al.[52] developed a novel timing module with a dead time of only 650 ps and 80 ps temporal resolution. This module supports parallel multispectral processing across 16 independent detector channels and achieves a 50-fold increase in measurement speed compared to traditional TCSPC-FLIM (at 10% of the excitation rate). Parallel detection and readout represent an effective approach to mitigate photon pile-up and accelerate data acquisition, as further demonstrated through the integration of a hybrid PMT with four timing modules. In this configuration, a pulse-driven spinner distributes photons arriving at different times within the same excitation period to individual timing modules. As a result, each module records one-quarter of the photons, substantially reducing photon count loss and enabling a frame rate of ~6 fps (for 256×256 pixels) with 25 ps temporal resolution[53].

The combination of multidetector arrays and parallel photon counting can enhance both imaging speed and spatial resolution via image scanning microscopy (ISM)[54]. When one detector module is in its dead time, an incoming photon has a high probability of being captured by another idle detector in the array, significantly increasing the system's effective count rate. Building on this concept, Liu et al.[55] developed a parallelized FLIM system that uses a fiber bundle to redirect photons to a 7-APD/TCSPC array, achieving a 2.5-fold increase in speed and a 1.5-fold improvement in spatial resolution. More recently, they incorporated polarization modulation to enable rapid switching between solid and donut beams for fluorescence emission difference imaging, thereby realizing dual-color super-resolution TCSPC-FLIM[56]. This refined system retains the benefits of parallel detection while reducing the inter-frame temporal gap to the millisecond level, effectively minimizing motion artifacts in live-cell imaging. However, both approaches are constrained by system complexity and limited scalability due to their reliance on multidetector arrays and sophisticated optical modulation, which may hinder widespread adoption in standard biological laboratories. Alternatively, photocathode-based arrays (e.g., APD or PMT) with low dark counts and large photosensitive areas can maximize collection efficiency in super-resolution or spectrally resolved applications[57-60], though the limited availability of such sensors (e.g., 16- or 32-channel) restricts their utility in high-throughput imaging.

Superconducting nanowire single-photon detectors (SNSPDs) represent an emerging technology with short dead time, excellent temporal resolution, and higher quantum efficiency in the second near-infrared (NIR-II) window compared to InGaAs cathodes[61-63], showing great promise for TCSPC applications[64]. The NIR-II region contains several optical windows that enable deeper light penetration[65, 66], making SNSPDs particularly suitable for *in vivo* TCSPC-FLIM. Compared to commercial NIR-II PMTs, Zheng et al.[67] demonstrated more reliable *in vivo* FLIM measurements using a custom SNSPD with a significantly narrower IRF (~109 ps vs. ~367 ps), which is crucial for imaging NIR probes with short fluorescence lifetimes, such as indocyanine green (ICG). SNSPDs with IRFs as narrow as ~4.3 ps at 1550 nm have been reported[68], and SNSPD arrays comprising tens[62] to hundreds of thousands[69] of sensors offer

unprecedented potential for high-speed TCSPC-FLIM with superior temporal resolution through parallel multipixel photon counting. Despite these advantages, the requirement for extremely low operating temperature and the high cost of SNSPD systems continue to limit their biomedical applications. Moreover, further development of biocompatible NIR-II probes with lifetime sensibility is essential to fully exploit SNSPD capabilities for *in vivo* imaging[21, 70, 71].

Single-photon avalanche diodes (SPADs) are widely employed in FLIM due to their high single-photon sensitivity and excellent temporal resolution, making them ideal for precise lifetime measurements. Farina et al.[72] introduced a hardware-based method that eliminates pile-up distortion by synchronizing the SPAD dead time with an integer multiple of the laser period within a single-pixel camera framework. This enables distortion-free fluorescence lifetime imaging at photon count rates up to 40% of the excitation frequency, as depicted in Fig. 4(b). While this approach improves data fidelity and acquisition speed, its single-pixel architecture may constraint throughput for large-format imaging and adaptability to dynamic or multi-frequency excitation scenarios. SPADs can also be fabricated into arrays, enabling parallel detection through compact, low-cost, CMOS-compatible architectures suited for high-throughput imaging. SPAD arrays integrated with parallel multichannel TDCs allow simultaneous readout of numerous single-photon events across all pixels or pixel rows, with temporal resolution on the order of tens of picoseconds[73-77]. However, a key trade-off of multi-pixel integration is a relatively low fill factor, often below 10% in standard 2D SPAD arrays, which limits photon collection efficiency and reduces the signal-to-noise ratio (SNR)—particularly in low-light biomedical imaging[78]. To address this, recent studies have explored the use of microlens arrays to concentrate fluorescence onto the photosensitive region, thereby improving the effective fill factor without increasing pixel pitch[79-81]. Furthermore, 3D-stacked SPAD architectures decouple the photodetector layer from the readout electronics, allowing more complex processing circuitry while maintaining a small form factor[82]. In contrast, SPAD line arrays permit electronics to be placed alongside pixel rows, resulting in a higher fill factor[83, 84]. Erdogan et al.[76] developed a 512×16 SPAD line array with a 49.31% fill factor and pixel-wise TDCs to overcome I/O bottlenecks and pile-up constraints. The incorporation of on-pixel 32-bin histogram memory with programmable timing widths (51.2 ps to 6.55 ns) enables high-throughput time-resolved multispectral imaging at rates up to 16.5 G-events/s, equivalent to an 85-fold improvement over conventional TCSPC modes. Subsequently, Williams et al.[85] used this advanced platform to construct a full-spectral TCSPC-FLIM system capable of simultaneously capturing 512 spectral channels at 256×256 pixels resolution. The system achieved remarkable spectral resolution (0.5 nm) and temporal resolution (50 ps), allowing rapid acquisition of spectral-lifetime data cubes without mechanical filter switching or sequential scanning. On-chip histogramming significantly reduced data volume and improved photon efficiency, enabling applications in complex biological samples such as unstained lung tissue, where subtle spectral-lifetime signatures distinguished cancerous from healthy regions [Fig. 4(c)]. However, the practical implementation of such data-intensive techniques remains challenged by the data transfer bottleneck between the FPGA and computer, as well as the substantial computational demand for processing millions of lifetime fits, which currently limits real-time visualization and full utilization of acquired datasets.

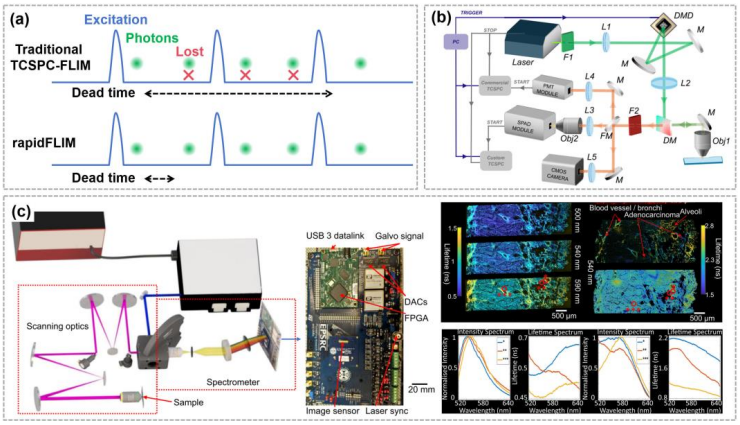

FIG. 4. Advances in TCSPC-FLIM hardware. (a) The rapidFLIM technique uses ultrashort dead time electronics to improve the detection duty cycle. (b) Pile-up-free FLIM implementation using a SPAD-based single-pixel camera system, with a PMT providing reference lifetime measurements and a CMOS camera offering structural guidance[72]. Reproduced with permission from Optics Express, **33**, 22296-22307 (2025). Copyright 2025 Optica Publishing Group. (c) Schematic of a full-spectral TCSPC-FLIM system based on a SPAD array (Left). Lifetime images of a lung tissue section at different wavelengths are shown (Right)[85]. G. O. S. Williams, E. Williams, N. Finlayson, A. T. Erdogan, Q. Wang, S. Fernandes, A. R. Akram, K. Dhaliwal, R. K. Henderson, J. M. Girkin and M. Bradley, Nature Communications, **12**, 6616 (2021); licensed under a Creative Commons Attribution (CC BY) license.

2. Excitation strategies

Beyond advancements in hardware aimed at increasing effective photon count rates, innovations in both wide-field and point-scanning excitation modalities have significantly contributed to the progress of advanced TCSPC-FLIM techniques. Wide-field illumination uniformly excites the sample surface, enabling the acquisition of two-dimensional information in a single exposure. Although this approach entails trade-offs in spatial resolution and imaging depth, wide-field TCSPC-FLIM remains a classical high-speed methodology renowned for its excellent temporal resolution. It commonly employs time-resolved detectors such as microchannel plates (MCPs) coupled with cameras or delay-line anodes, or single-photon avalanche diode (SPAD) arrays[86-90]. Light-sheet microscopy enhances this strategy by providing optical sectioning within a wide-field framework. It illuminates the sample with a thin, planar light sheet orthogonal to the detection axis, thereby minimizing out-of-focus excitation[91]. As a key strategy for achieving volumetric FLIM, this approach enables 3D mapping of lifetime contrasts in optically sectioned specimens. The pursuit of volumetric lifetime imaging has driven the development of diverse methodologies, including multi-focal scanning and point spread function engineering, to comprehensively visualize dynamics within tissues and cells, as discussed in a recent specialized review[20]. As shown in Fig. 5(a), Hirvonen et al.[92] utilized a double-MCP detector[86] to construct a light-sheet system capable of volumetric TCSPC-FLIM at approximately 3 fps per slice, with

photon count rates in the tens of kHz under 10 MHz repetition rate excitation. This system demonstrated applicability for low-light-dose imaging, essential for long-term observations of light-sensitive specimens such as cancer cell spheroids and Caenorhabditis elegans. Similarly, Samimi et al.[93] implemented a light-sheet FLIM system employing a 192×128 pixel SPAD array, where each pixel incorporated an independent time-to-digital converter (TDC) with a temporal resolution of ~41 ps. Applied to autofluorescence studies in zebrafish neutrophils, this configuration achieved a 6 - 30-fold improvement in acquisition speed compared to conventional point-scanning methods. Nevertheless, the lateral resolution in such setups is limited by light-sheet thickness, and lifetime precision can be compromised by scattering and absorption in deeper tissue regions, constraining the performance of wide-field TCSPC-FLIM in highly heterogeneous or optically dense samples.

Conventional confocal laser scanning microscopy (CLSM) and multiphoton fluorescence microscopy achieve high spatial resolution by raster-scanning a focused spot across the entire field of view (FOV). Multiphoton microscopy, in particular, is widely adopted for deep-tissue imaging due to its inherent optical sectioning capability[94]. However, in applications involving sparsely labeled or dispersed samples, a significant portion of the FOV may comprise non-informative background, leading to inefficient use of acquisition time. To address this, random-access scanning offers an effective alternative to conventional raster scanning by selectively targeting irregularly shaped regions of interest (ROIs)[95]. Acousto-optic deflectors (AODs) are especially advantageous for this purpose, providing inertialess beam steering at rates up to MHz through variable radio frequency (RF), thereby enabling high-speed, random-access imaging[96]. While other beam-scanning mechanisms—such as polygon mirrors, resonant mirrors, and double-prism systems[97, 98]—are also employed, these inertial methods often waste dwell time on non-informative regions and increase unnecessary light exposure. The use of orthogonal AOD pairs allows flexible and rapid TCSPC-FLIM measurements of arbitrarily defined 2D ROIs[99, 100]. Recently, an addressable scanning FLIM system incorporating feedback control via an electron-multiplying CCD (EMCCD) was developed. This system captures real-time intensity images to localize moving single particles and dynamically adjusts the AOD scanning region to track the target[101]. Leveraging this setup and an alternating descent conditional gradient (ADCG) algorithm, Lin et al.[102] demonstrated a high-speed FLIM technique capable of tracking moving particles within a 16×16 pixel region at 7.8 fps, offering a practical solution for dynamic biological imaging. A mosaic FLIM acquisition mode was also introduced, storing multiple consecutive lifetime images in a single dataset to minimize inter-frame time gaps, as depicted in Fig. 5(b). Despite these advantages, AODs present certain limitations that hinder their broader adoption in multiphoton FLIM[103]. The most notable issue is spatiotemporal dispersion of ultrafast laser pulses, arising from the wavelength-dependent deflection angle, which typically necessitates compensatory prisms[100]. Additionally, constraints in aperture size and diffraction efficiency limit the usable FOV and maximum optical throughput. Although wide-band AODs have been designed for large-FOV imaging[104], their application in fast multiphoton FLIM remains relatively unexplored.

Multifocal excitation represents a complementary strategy for proportionally increasing imaging speed by generating an array of excitation foci. This can be achieved using beam splitters[105], microlens array[106], diffractive optical elements[107], spatial light modulator (SLM)[108], or digital micromirror device (DMD)[109]. Multifocal excitation enables enhanced optical sectioning

and higher focal energy density, making it particularly suitable for multiplane or multiphoton microscopy[110-114]. Owing to integrated digitization and scalable pixel counts, SPAD arrays are frequently employed as detectors in multifocal TCSPC-FLIM systems[112, 115, 116]. For instance, a doubly weighted Gerchberg-Saxton (DWSG) algorithm was developed to generate a uniform 8×8 excitation array via computational holography implemented on an SLM[117]. Poland et al.[113] demonstrated a high-speed multifocal multiphoton FLIM system that scans a 64-foci array across the sample using a pair of galvanometric mirrors, with fluorescence signal collected descanned onto a SPAD array, as shown in Fig. 5(c). This approach effectively achieves 100% optical fill factor, mitigating photon losses associated with the low physical fill factor of 2D SPAD arrays[112]. While maintaining high spatiotemporal resolution, this method achieves a 64-fold increase in acquisition speed compared to single-beam scanning. Further advancements enabled volumetric FLIM imaging without axial scanning, where a modified DWSG algorithm generated at least four multifocal planes (4×4 beamlets) to obtain 3D projections[118]. Scanning a laterally stretched Gaussian beam in one dimension can also effectively increase the number of excitation foci along the scan axis. Recently, Poland et al. developed a FLIM technique that is 33 times faster than prior reports[119] by conjugating a one-dimensional scanning beam with a 1024×8 SPAD line detector featuring on-chip histogramming in a confocal system [Fig. 5(d)]. This setup achieved a maximum photon count rate of 32.23 MHz per pixel, enabling accurate lifetime determination at up to 4 fps (without pixel binning) in heterogeneous specimens at 512×512 resolution[116]. However, multifocal excitation generates substantial data flow, constrained by the transfer rates of histogrammed decay data from the SPAD array to a computer. Moreover, the computational burden of conventional fitting methods, such as the Levenberg-Marquardt algorithm, becomes prohibitive for high-throughput FLIM applications requiring real-time lifetime determination[120-122]. This has spurred the adoption of faster, non-fitting algorithms—such as the center of mass method (CMM)[123] and its variants[114, 124]—which enable rapid lifetime estimation and can be implemented directly on FPGA hardware or application-specific integrated circuits (ASICs)[125].

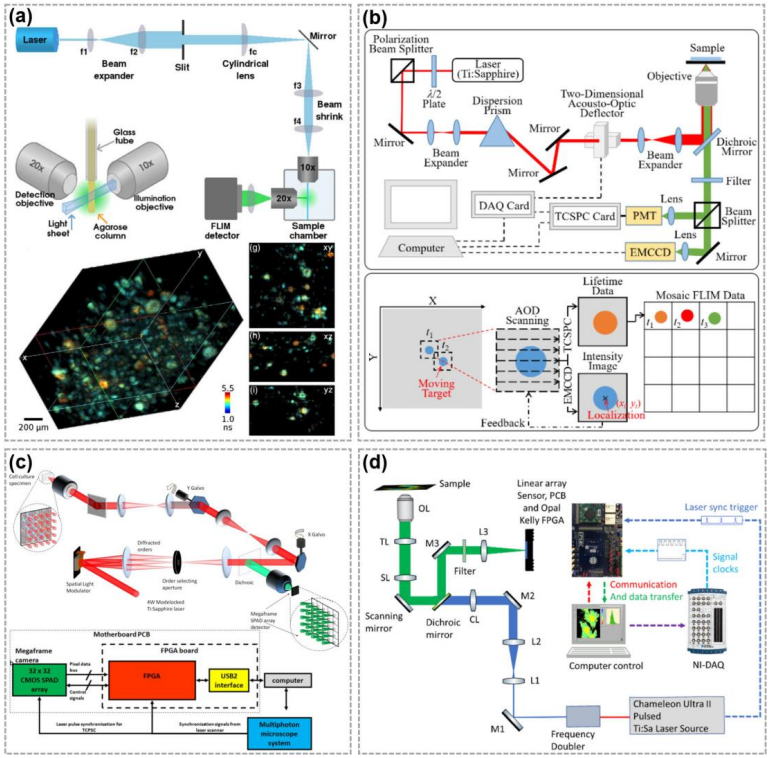

FIG. 5 Advanced excitation strategies for high-speed TCSPC-FLIM. (a) Integration of light-sheet microscopy with TCSPC-FLIM enables volumetric imaging at 3 fps in a 3D bead sample[92]. L. M. Hirvonen, J. Nedbal, N. Almutairi, T. A. Phillips, W. Becker, T. Conneely, J. Milnes, S. Cox, S. Stürzenbaum and K. Suhling, Journal of Biophotonics, **13**, e201960099 (2020); licensed under a Creative Commons Attribution (CC BY) license. (b) AOD-based addressable scanning facilitates dynamic single-particle tracking using a mosaic data acquisition strategy[102]. Reproduced with permission from Biomedical Optics Express, **14**, 1718-1731 (2023). Copyright 2023 Optica Publishing Group. (c) Multifocal array scanning system for parallel imaging, illustrating the internal structure of a SPAD array detector[113]. Reproduced with permission from Biomedical Optics Express, **6**, 277-296 (2015). Copyright 2015 Optical Society of America. (d) Fast line-scanning imaging achieved with a SPAD line array detector[116]. H. Mai, A. Jarman, A. T. Erdogan, C. Treacy, N. Finlayson, R. K. Henderson and S. P. Poland, Optics Letters, **48**, 2042-2045 (2023); licensed under a Creative Commons Attribution (CC BY) license.

3. Algorithms and deep learning (DL)

With hardware and excitation strategies continuously advancing photon budgets and acquisition speed, the persistent bottleneck remains the efficient and accurate conversion of

time-stamped photons into fluorescence lifetime estimates with well-controlled uncertainty and low latency. Classical model-based estimators, such as LMA and MLE, remain the accuracy baseline for exponential decays. Current practices emphasize the use of Poisson noise models, global or linked-parameter fitting across pixels or spectral channels, and various engineering optimizations including careful initialization, trust-region updates, and GPU-based parallelization to significantly reduce computation time[126, 127]. Pushing the boundaries of optimization, Li et al.[128] introduced a data compression strategy based on histogram clustering, which groups pixels by decay profile similarity. This method drastically reduces the number of required fitting operations, achieving up to a 106-fold speed enhancement over conventional iterative algorithms without loss of accuracy. While these refinements maintain high precision and interpretability, iterative solvers still introduce considerable latency when processing megapixel or multifocal datasets.

To fundamentally address the photon-counting bottleneck, recent algorithmic innovations have pursued two complementary strategies: one aimed at improving the statistical efficiency of existing fitting frameworks, and the other seeking to directly bypass iterative fitting. Representing the first approach, Wang et al.[129] developed a nonparametric empirical Bayesian framework that jointly estimates population-level lifetime distributions and pixel-level parameters by leveraging spatial correlations and global photon statistics across the entire image. Using a nonparametric MLE to infer an empirical prior distribution directly from the detected photons, this method integrates Bayesian inference for pixel-wise lifetime estimation or direct computation of integrated properties (e.g., mean lifetime or fractional contributions). This technique enhances accuracy under low-photon-count conditions and reduces computational load compared to pixel-wise fitting, though it depends on the separability of multi-exponential components and may exhibit bias when lifetime populations overlap. More recently, a novel alternating descent conditional gradient (ADCG) algorithm has been applied to the low-photon-count regime[102]. By formulating lifetime recovery as a compressed sensing problem that exploits the inherent sparsity of fluorescence components, ADCG combines rapid local search with globally stable convex optimization. It achieves robust fitting with as few as 45 photons—scenarios where traditional MLE fails—though the performance may decline for multi-exponential models with unknown components.

In contrast, with the inspiration of TCSPC-based flight times detection[130], Sun et al.[131] exemplified the second strategy with a fitting-free, low-photon-count FLIM technique that utilizes the statistics of laser pulses required to detect a photon. This statistical count value is a random variable drawn from a geometric distribution whose parameter is directly governed by the fluorescence lifetime. Intuitively, a shorter lifetime means a high probability of photon emission per pulse, typically resulting in a low pulse count, and vice versa. Therefore, direct lifetime extraction was achieved via a non-iterative rapid lifetime determination algorithm[132]. This approach reduces acquisition time to one-fifth of that required by conventional TCSPC-FLIM while maintaining accuracy under photon-limited conditions, offering a compelling alternative to traditional fitting.

In parallel, deep learning (DL) methods are increasingly pivotal in TCSPC-FLIM, enhancing the accuracy, robustness, and real-time capability of lifetime estimation—particularly under photon-starved conditions. As data-driven approaches, DL models apply nonlinear transformations to raw inputs—such as time-stamped photon streams or decay histograms—to hierarchically extract features and directly map them to lifetime parameters. An early demonstration used an

artificial neural network (ANN) structured as a multilayer perceptron with two hidden layers[133]. This model accepts fluorescence decay curves (with input nodes matching the time channels of the acquisition system) and outputs four parameters for bi-exponential decay (amplitudes and lifetimes). It achieved a 180-fold increase in processing speed while delivering image quality comparable or superior to conventional LSA, though its neglect of the IRF may limit accuracy under conditions with significant temporal broadening. Yao et al.[134] combined compressed sensing with a convolutional neural network (CNN) to efficiently process time-resolved single-pixel data. Trained on extensive synthetic datasets, this hybrid framework rapidly reconstructs both intensity and lifetime images, reaching a speedup of ~7000× over traditional fitting while preserving quantification accuracy at low photon counts. Another major innovation, FLI-Net, employs a 3D-CNN architecture to process TCSPC-FLIM data[135]. As illustrated in Fig. 6(a), the network ingests 3D tensors (time × 28 × 28 pixels) of IRF-convolved bi-exponential decays and outputs lifetime parameter maps, operating ~30× faster than the commercial software SPCImage. To improve efficiency and hardware compatibility, Xiao et al.[136] developed a streamlined 1D-CNN that operates solely on temporal decay vectors. This FPGA-friendly architecture reduces training time by 8× compared to FLI-Net. Subsequent modifications introduced a spatial super-resolution task [Fig. 6(b)], enabling the network to enhance spatiotemporal resolution and decouple lifetime and intensity information. By training on paired high- and low-resolution images generated via a physical degradation model, the network successfully reconstructed high-resolution FLIM images from low-resolution inputs, as validated on experimental data from mouse macrophages[137].

In biomedical imaging, photon budgets are often severely constrained due to limits on light exposure (to avoid photobleaching and phototoxicity), low fluorophore concentrations, short pixel dwell times, and signal attenuation in tissue. To address these challenges, Chen et al.[138] developed flimGANE, a generative adversarial network (GAN)-based framework that fed low-photon-count decay histograms into a Wasserstein GAN to generate high-photon-count equivalents. For 512×512 pixel images, flimGANE achieved a processing speed 258× faster than LSA and 2800× faster than MLE. However, its end-to-end training is time-consuming (up to 500 hours) and changes in the IRF may necessitate retraining, limiting generalizability. More recently, a dual-subnetwork architecture named FPFLI was introduced [Fig. 6(c)], comprising a local lifetime estimation (LLE) module and a neural implicit image interpolation (NIII) module[139]. FPFLI reliably estimates lifetimes with fewer than 10 photons per pixel by aggregating information from neighboring pixels and integrating intensity and locally estimated lifetimes to reconstruct the final image. Leveraging spatial correlations in both intensity and lifetime, it generates 512×512 pixel images in 2 seconds. Similarly, Shen et al.[140] proposed SparseFLIM, which uses a coupled bidirectional propagation network to reconstruct high-fidelity lifetime images from highly sparse measurements. By exploiting spatiotemporal correlations and fusing features across sequential frames, the method achieved over 10× photon enrichment and significantly improved SNR and lifetime accuracy without explicit fitting [Fig. 6(d)]. It effectively handles spatiotemporal undersampling and generalizes well across diverse imaging modalities—including multispectral and *in vivo* endoscopic FLIM—though performance may require retraining for substantially different optical systems or sample types. Together, these advances underscore the potential of data-driven methods to overcome photon sparsity and accelerate FLIM analysis while retaining critical biological information.

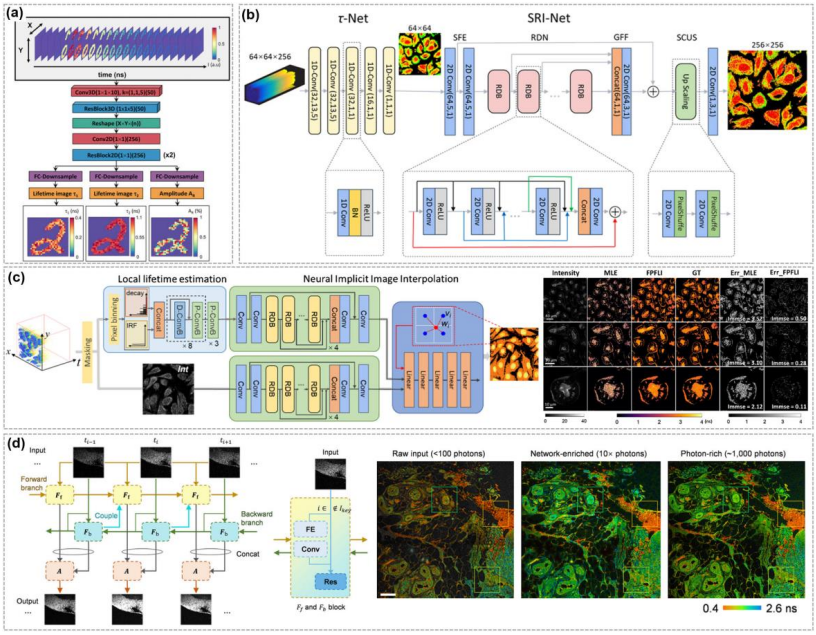

FIG. 6 DL-based TCSPC-FLIM analysis strategies. (a) FLI-Net architecture processes 3D input tensors (X, Y, t) for end-to-end estimation without interative fitting[135]. Reproduced with permission from Proceedings of the National Academy of Sciences, **116**, 24019-24030 (2019). Copyright 2019 PNAS License. (b) A hybrid network architecture improves spatiotemporal resolution by integrating spatial upsampling and temporal feature extraction[137]. D. Xiao, Z. Zang, W. Xie, N. Sapermsap, Y. Chen and D. D. U. Li, Optics Express, **30**, 11479-11494 (2022); licensed under a Creative Commons Attribution (CC BY) license. (c) FPFLI framework comprising LLE and NIII subnetworks (Left), with comparative lifetime imaging results of a mouse kidney section processed via different methods (Right)[139]. D. Xiao, N. Sapermsap, Y. Chen and D. D. U. Li, Optica, **10**, 944-951 (2023); licensed under a Creative Commons Attribution (CC BY) license. (d) SparseFLIM network architecture utilizing coupled bidirectional propagation (Left), alongside enhanced FLIM reconstructions of human skin tissue under extreme photon-sparse conditions (Right)[140]. B. Shen, Y. Lu, F. Guo, F. Lin, R. Hu, F. Rao, J. Qu and L. Liu, Communications Biology, **7**, 1359 (2024); licensed under a Creative Commons Attribution (CC BY) license.

B. Advancements in TG-FLIM

TG-FLIM methods offer marked advantages in acquisition speed, particularly in wide-field implementations[141-143], which bypass point scanning and typically outperform raster or multifocal configurations[29, 144]. Although out-of-focus fluorescence can limit TG-FLIM when imaging thick samples, several studies have demonstrated achievable optical sectioning through strategies such as Nipkow disk[145, 146], structured[147, 148] or light-sheet[149] illumination. In the following, we organize

recent advances according to the gating mechanism: electronic shutters (e.g., gain-modulated intensifiers and SPAD sensors) and optical shutters (e.g., Pockels cell-based time slicing). State-of-the-art electronics now enable sub-nanosecond or even tens of picoseconds control over gating parameters[74, 150-152], significantly enhancing the temporal discrimination of fluorescence signals.

1. Electronic shutter

Electronic shutter-based TG-FLIM employs detector-level temporal gating to measure fluorescence lifetimes, eliminating the need for external optical modulators. The two predominant architectures are gated optical intensifier (GOI) systems coupled with a CCD (ICCD) or sCMOS camera, and SPAD arrays integrated with CMOS readout. In GOI-based TG-FLIM, temporal selection is achieved by rapidly switching the photocathode bias to convert weak fluorescence photons into photoelectrons. These are amplified via a MCP cascade and reconverted to photons on a phosphor screen before being captured by a camera[28, 145, 153-156]. sCMOS sensors provide both global and rolling shutter modes; TG-FLIM generally uses global shutter mode to ensure uniform exposure timing across all pixels. Rolling shutter introduces row-to-row delays substantially longer than typical gate widths, preventing accurate decay acquisition. For example, Li et al.[157] combined an sCMOS camera with a GOI to construct a TG-FLIM system integrated with digital light-sheet microscopy, where a virtual light sheet was generated by rapid scanning of a focused laser beam. Using a 1 ns gate width, they acquired time-gated image stacks at multiple delays and depths, enabling millimeter-scale 3D lifetime mapping in EGFP-labeled zebrafish, as illustrated in Fig. 7(a). Another emerging approach, light-field tomography (LIFT), captures 3D spatial and spectral information by recording frontal projections and computationally reconstructing them[158, 159]. As shown in Fig. 7(b), Ma et al.[160] recently developed a multidimensional wide-field FLIM platform combining LIFT with both TCSPC-FLIM using a SPAD linear array and spectrum-resolved TG-FLIM using a GOI-sCMOS pair. A diffractive grating placed before the GOI enabled hyperspectral FLIM detection, a strategy also adopted in earlier studies using array sensors[57, 83, 161, 162]. However, the dual photon-electron-photon conversion and subsequent camera readout still limit overall temporal resolution to the sub-nanosecond scale[163]. Additionally, the pixellation of MCPs is coarser than that of modern cameras, limiting spatial resolution, and external modulation circuits introduce position-dependent delays across the field of view, necessitating pixel-wise IRF calibration for accurate lifetime fitting in GOI architectures[152].

In contrast, SPAD arrays with CMOS readout have emerged as a competitive alternative, offering single-photon sensitivity, inherent electronic gating, and potential for miniaturization. Unlike multipixel SPAD arrays operated in TCSPC mode[77, 83, 164], TG-FLIM typically employs large-format 2D arrays for full-field imaging[165]. The SwissSPAD series represents a state-of-the-art example[150, 166], featuring arrays of up to 500×500 pixels, minimum gate widths of 0.99 ns, and a temporal resolution of 17.9 ps using a dual-gate architecture[74]. Smith et al.[167] utilized the 512×512 pixel SwissSPAD2[75] for NIR TG-FLIM in both *in vitro* and *in vivo* settings[Fig. 7(c)], comparing sub-nanosecond lifetimes of several NIR dyes measured by SPAD arrays and ICCD. Their results confirmed the suitability of SwissSPAD2 for non-invasive preclinical TG-FLIM while overcoming limitations of ICCD such as photocathode degradation, vulnerability to overexposure, and high cost. A key advantage of SPAD arrays is their compatibility with miniaturization, making them highly valuable for applications such as

endoscopy. Matheson et al. developed a handheld TG-FLIM system incorporating a <2 mm^2 SPAD array (120×128 pixels) within a ~4.5 cm^3 enclosure, achieving >1 Hz imaging of animal tissues with an IRF of ~550 ps[168]. Subsequently, as depicted in Fig. 7(d), an endoscopic TG-FLIM system was realized by addressing critical challenges in optical alignment, stray light suppression, and miniaturized electronic interfacing. The successful acquisition of label-free lifetime images from *in vitro* tissues further demonstrated its ability to differentiate between tissue types[169].

2. Optical shutter

Optical shutters-based TG-FLIM performs temporal gating within the optical path, modulating the fluorescence signal before it reaches the detector. The Pockels cell, leveraging the linear electro-optic effect in anisotropic crystals, is currently the most widely used optical shutter for wide-field TG-FLIM in biological imaging. By applying a high-voltage, fast-rising electrical pulse to the crystal, the Pockels cell alters the polarization state of transmitted fluorescence on a nanosecond timescale[170]. This modulated signal is then converted into an intensity gate using a pair of crossed polarizers in the detection path. In TG-FLIM, synchronization of this voltage pulse with the fluorescence decay window allows selective transmission of photons within a precisely defined temporal slice, which is subsequently recorded by a camera. Compared to electronic shutter-based TG-FLIM, this approach enables sub-nanosecond gating without the two-stage photoelectric conversion losses inherent to GOI systems and avoids the geometric fill factor limitations of SPAD arrays, thereby offering higher theoretical photon utilization efficiency.

Bowman et al. first proposed the use of a Pockels cell combined with polarizing beam splitters (PBS) to achieve nanosecond temporal resolution with high photon collection efficiency in wide-field TG-FLIM[142]. For systems constrained by the Pockels cell aperture, they demonstrated that two crystals could be operated independently to generate four temporal bins. Using either Gaussian or step-function pulses to modulate the Pockels cell, fluorescence lifetimes can be rapidly obtained either by scanning the gate delay to directly sample the decay or by calculating intensity ratios between gated and ungated channels covering the entire decay in a single snapshot. A resonant driving method achieved a gating frequency of 39 MHz with dual Pockels cells, enabling sub-nanosecond resolution without the need for multiple sampling[171]. More recently, they developed a coaxial pair of Pockels cells with transverse crystal geometry, arranged with a 90° relative rotation and driven resonantly with a reversed electric field to compensate for static and off-axis birefringence [Fig. 7(e)]. This configuration enabled pixel-wise lifetime extraction at 1 kHz frame rates with approximately 3 ps sensitivity, allowing *in vivo* recording of neuronal action potentials[141]. These advances underscore the capability of optical shutters to provide sub-nanosecond gating precision and enhanced photon efficiency, making them particularly suitable for dynamic biomedical applications requiring both high temporal resolution and maximal signal preservation. Furthermore, novel analysis strategies, such as rapid lifetime determination using compressed sensing approaches[57, 134, 161], have been proposed to accelerate data acquisition while maintaining accuracy, paving the way for real-time, high-resolution TG-FLIM in both benchtop and miniaturized endoscopic systems.

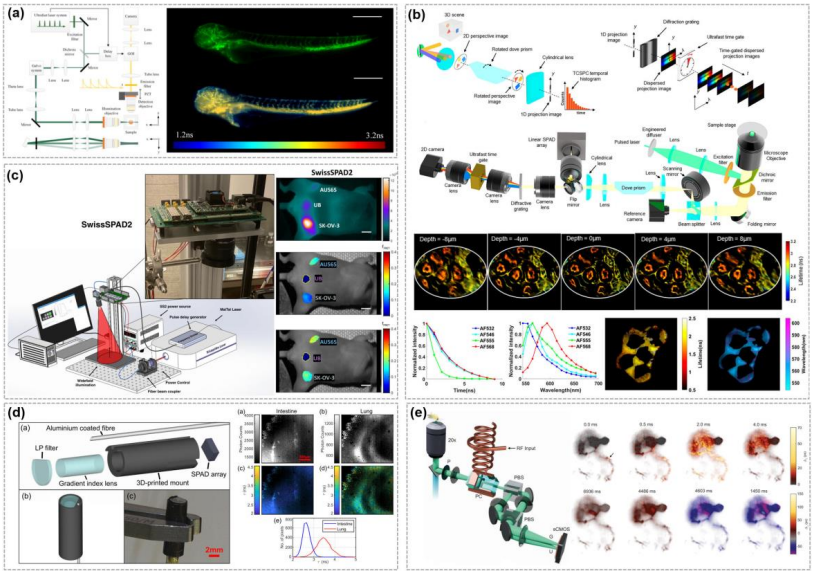

FIG. 7. Advanced TG-FLIM techniques based on electronic or optical shutters. (a) A TG-FLIM system with digital light-sheet scanning enables millimeter-scale 3D imaging of zebrafish[157]. R. Li, A. Liu, T. Wu, W. Xiao, L. I. Tang and L. Chen, Journal of Microscopy, **279**, 69-76 (2020); licensed under a Creative Commons Attribution (CC BY) license. (b) Multidimensional LIFT based on a SPAD linear array and a GOI-camera pair; reconstructed lifetime images of a mouse kidney tissue slice at various depths and spectral-resolved lifetimes images of lung organoids[160]. Y. Ma, J. Park, L. Huang, C. Sen, S. Burri, C. Bruschini, X. Yang, Q. Cui, R. B. Cameron, G. A. Fishbein, B. N. Gomperts, A. Ozcan, E. Charbon and L. Gao, Proceedings of the National Academy of Sciences, **121**, e2402556121 (2024); licensed under a Creative Commons Attribution (CC BY) license. (c) Schematic of TG-FLIM using the SwissSPAD2 camera for *in vivo* imaging[167]. Reproduced with permission from Optica, **9**, 532-544 (2022). Copyright 2022 Optica Publishing Group. (d) AMiniaturized endoscopic TG-FLIM design based on a SPAD array (Left) and corresponding imaging results of sheep lung and intestine samples *in vitro* (Right)[169]. D. Angelone, N. Nudds, A. B. Matheson, A. T. Erdogan, W. Messina, R. Burke, R. K. Henderson, S. Andersson-Engels and S. K. Venkata Sekar, Optics Letters, **50**, 4230-4233 (2025); licensed under a Creative Commons Attribution (CC BY) license. (e) Schematic of an optical shutter-based TG-FLIM platform (Left) and *in vivo* recording of spike propagation at 1-kHz frame rate (Right)[141]. A. J. Bowman, C. Huang, M. J. Schnitzer and M. A. Kasevich, Science, **380**, 1270-1275 (2023); licensed under a Creative Commons Attribution (CC BY) license.

C. Advancements in SC-FLIM

Beyond the fundamental time-to-space conversion principle, recent developments in streak camera-based fluorescence lifetime imaging microscopy (SC-FLIM) have primarily focused on

overcoming the limitations imposed by line-scanning acquisition. Two complementary strategies have emerged: hardware multiplexing coupled with adaptive sweep control, and computational or optical encoding for snapshot acquisition. These approaches enhance dimensionality and effective frame rates, albeit with trade-offs in spatial resolution and reconstruction complexity.

Early work by our group demonstrated the feasibility of multiplexed SC-FLIM using a customized streak camera in which the conventional entrance slit was replaced with a pinhole array. By incorporating a dispersive element, this system achieved simultaneous temporal and spectral imaging across 4×4 spatial points within a single snapshot, delivering resolutions of 6.5 ps and 3 nm, respectively—though at the cost of reduced spatial resolution[172]. To accommodate varying lifetime ranges in biological samples, Liu et al.[173] implemented multiple sweep-circuit configurations within the streak camera, enabling adaptation to specific time windows. This hardware-oriented approach was further refined through the integration of galvanometer mirrors for rapid line-scanning and slower frame-scanning, achieving planar imaging with a temporal resolution of approximately 50 ps[174]. Nevertheless, a fundamental constraint remains: one detector axis is permanently dedicated to temporal information, necessitating extensive scanning and sequential readout that limit the practical application of SC-FLIM for volumetric or high-speed multidimensional imaging.

To address this inherent limitation, Ma et al.[175] introduced an innovative compressed sensing-based SC-FLIM method that enables wide-field lifetime imaging through spatial encoding, effectively bypassing the need for mechanical scanning. This strategy employs a dual-camera setup: a reference camera captures a time-integrated fluorescence image, while a streak camera records wide-field emission patterns encoded by a DMD using two-dimensional complementary pseudorandom binary patterns [Fig. 8(a)]. These patterns are projected onto a fully opened entrance slit, allowing the streak camera to convert photon arrival times into spatial displacements of both encoded channels within a single exposure. Computational reconstruction—incorporating spatial priors from the reference image—decodes this spatiotemporally multiplexed data into high-resolution lifetime maps (500×400 pixels) at a remarkable speed of 100 Hz, limited primarily by camera readout. This snapshot capability minimizes motion artifacts and photobleaching, facilitating robust imaging of rapid dynamic processes such as neural spiking in live cells. However, as a wide-field technique, it lacks inherent optical sectioning, making measurements vulnerable to out-of-focus background in thick specimens. This drawback could be mitigated in the future by integrating structured illumination or light-sheet techniques, supported by large-format streak tubes with enhanced spatial information capacity[176].

In a parallel development, Chen et al.[177] devised a scan-free SC-FLIM strategy for four-dimensional multi-particle tracking by encoding fluorescence lifetime into the spatial properties of an engineered point spread function (PSF). They utilized a double-helix PSF[178]—generated via a phase mask in the Fourier plane—that causes a point emitter to appear as two lobes whose rotational angle varies monotonically with axial position. This enables nanoscale spatial localization across a 4 μm depth without mechanical scanning. A slit-removed streak camera was employed to capture multiple two-lobe patterns containing both spatial and temporal information, demonstrating the method's potential for tracking phagocytosis in living cells [Fig. 8(b)].

Together, these advances illustrate how modern SC-FLIM is transcending traditional line-scanning paradigms through innovations in computational optics and PSF engineering. By

enabling wide-field, high-speed, and multidimensional lifetime imaging, these developments are transforming SC-FLIM from a specialized ultrafast tool into a more photon-efficient, large-field-of-view, and dynamically capable platform. This expanded functionality makes it particularly suited for investigating transient biophysical processes that are beyond the reach of slower time-correlated single-photon counting (TCSPC) or time-gated (TG) detection systems.

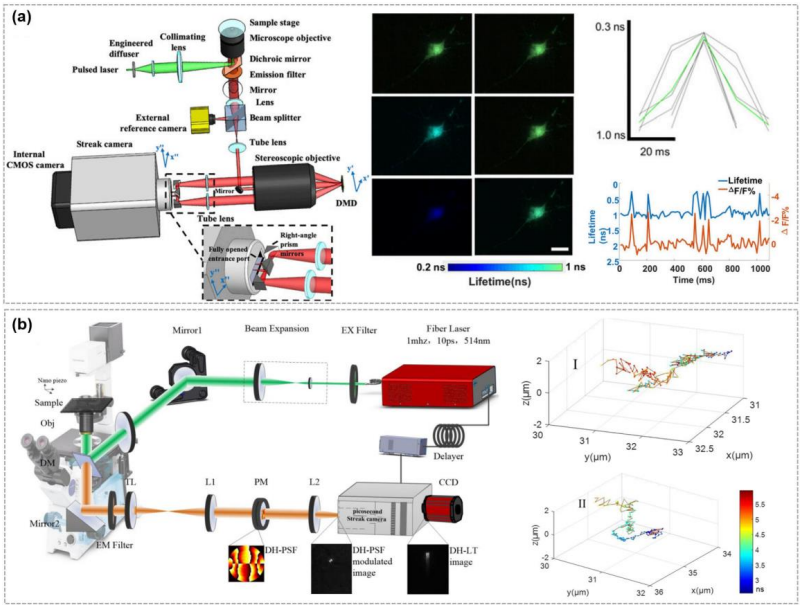

FIG. 8. Advanced 2D or 3D SC-FLIM based on scanning-free strategies. (a) Schematic of a compressed sensing-based SC-FLIM system (Left); reconstructed lifetime images of the neuron and time-lapse lifetime recording of neural spiking at 100-Hz frame rate (Right)[175]. Reproduced with permission from Proceedings of the National Academy of Sciences, **118**, e2004176118 (2021). Copyright 2021 PNAS License. (b) Schematic of the 4D (X, Y, Z, and τ) tracking system (Left), and traces of two particles during endocytosis in living RAW cells (Right)[177]. D. Chen, H. Li, B. Yu and J. Qu, Nanophotonics, **11**, 1537-1547 (2022); licensed under a Creative Commons Attribution (CC BY) license.

D. Advancements in DPR-FLIM

DPR-FLIM techniques achieve high frame rates by directly digitizing analog fluorescence pulse waveforms using advanced data acquisition (DAQ) modules. When fluorescence signals are sufficiently intense, a single excitation pulse can yield a reliable decay profile suitable for subsequent fitting or rapid lifetime determination[179]. Recent advancements in DPR-FLIM have focused on overcoming inherent limitations in temporal resolution, noise susceptibility, and data processing, while further leveraging its high-speed acquisition capabilities. Key developments include the refinement of rapid lifetime determination algorithms that bypass computationally intensive fitting procedures, the design of novel system architectures for improved temporal

accuracy and real-time processing, and integration with single-cell analysis platforms. These innovations collectively enhance the robustness and versatility of DPR-FLIM for high-throughput biological research and clinical translation.

1. Core computational paradigms: lifetime extraction via moment analysis

A representative implementation of DPR-FLIM is pulse sampling (PS), which enables multiparametric analysis of tissue autofluorescence. Marcu et al. pioneered the foundational concepts[34, 180] and demonstrated significant clinical potential[181]. In this approach, free-hand point scanning is performed using a multimode fiber that transmits intense excitation pulses and collects fluorescence, facilitating fluorescence lifetime imaging mesoscopy (PS-FLIm) for large-scale clinical diagnostics[182]. To simultaneously map lifetimes of key endogenous fluorophores, temporal multiplexing via delayed fibers is employed, allowing detection across four spectral channels within a single pulsed cycle using a single microchannel plate photomultiplier tube (MCP-PMT)[183]. Following background subtraction, signals undergo Laguerre basis expansion and constrained least-squares approximation (LSA) deconvolution to extract the fluorescence impulse response function without a priori assumptions about decay complexity[184]. The average fluorescence lifetime (τ_j) for each spectral channel j is then rapidly computed as the temporal centroid[185]:

$$\tau_j = \frac{\sum_k I_j(k) \cdot t_k}{\sum_k I_j(k)} \tag{13}$$

where $I_j(k)$ is the deconvolved fluorescence intensity at discrete time sample k, and t_k is the corresponding time. This moment analysis enables rapid lifetime determination within 1 ms per sampling point, eliminating the need for computationally intensive exponential fitting. The combination of τ_j, spectral intensity ratios, and Laguerre coefficients provides a comprehensive framework for seamless integration into optical biopsy workflows[186-189]. Furthermore, the inherent high speed of PS-FLIm supports compatibility with various scanning-based imaging modalities, including optical coherence tomography (OCT)[190-192], ultrasound[193, 194], and Raman imaging[195, 196]. These multimodal integrations offer profound insights into tissue heterogeneity, highlighting strong potential for precise *in vivo* disease diagnosis.

Recently, a galvo-scanning PS-FLIm system was developed to enable rapid large-field imaging (6×15 cm^2) at high resolution (~17.5 μm), utilizing independent APDs for multispectral signal collection [Fig. 9(a)][197]. This approach, however, requires additional IRF calibration to maintain lifetime accuracy due to nonlinear temporal response associated with individual APD gain levels. Despite this, the strategy offers significant advantages in detection efficiency over temporal multiplexing with a single MCP-PMT, including higher quantum efficiency, reduced noise, lower coupling losses, and independent per-channel gain control. These improvements result in a 5-fold reduction in variability and a 4-fold increase in measurement speed[198]. Additionally, PS-FLIm effectively rejects ambient light due to its extremely low acquisition duty cycle (<0.01%) combined with high instantaneous photon flux per excitation pulse, making it exceptionally suitable for robust intraoperative applications[199].

PS-FLIm is typically implemented with low-repetition-rate pulsed lasers, which align well

with temporal and spectral multiplexing in GHz-bandwidth electronics. However, at high repetition rates, the per-pulse sampling window shrinks while the pulse rate increases, demanding higher sampling bandwidth and continuous throughput from the digitizer—often becoming a system bottleneck. Moreover, preprocessing signals before moment analysis is relatively time-consuming, limiting real-time lifetime readout in point-scanning applications with large pixel counts.

In contrast, the analog mean delay (AMD), based on center-of-mass method (CMM), offers an alternative DPR-FLIM method by intentionally broadening fluorescence pulses via low-pass filtering. This allows mean lifetime (τ_m) extraction in MHz-bandwidth systems at minimal cost[200]. The value of τ_m is calculated by subtracting the mean delay of the instrument impulse response function $I_{\mathrm{irf}}(t)$ from that of the fluorescence decay waveform $I_{\mathrm{fl}}(t)$:

$$\tau_m = \left(\frac{\int t \cdot I_{fl}(t)dt}{\int I_{fl}(t)dt}\right) - \left(\frac{\int t \cdot I_{irf}(t)dt}{\int I_{irf}(t)dt}\right) \tag{14}$$

This approach leverages the intrinsic deconvolution property of temporal centroids to counteract system-induced temporal broadening. AMD-FLIM thus enables high-photon-economy lifetime determination using a PMT, achieving imaging at 7.7 fps with 158×127 pixel resolution[201]. Its computational simplicity facilitates real-time lifetime processing and display in fast-scanning systems. Kim et al.[202] advanced this paradigm through a CPU-parallelized architecture that attained 3.8 fps at 1024×1024 pixels with lifetime errors below 10%. They proposed a hardware-level synchronization circuit using D flip-flops and logic gates to align laser pulses, resonant scanner positions, and digitizer triggers, while a dual-PMT configuration concurrently acquired both fluorescence and IRF signals through parallel optical paths to eliminate temporal jitter. Integration of Intel Threading Building Blocks (TBB) with mutex-protected ring buffering ensured concurrent data acquisition and processing without frame loss. Subsequently, Ryu et al.[203] demonstrated a two-photon AMD-FLIM technique based on resonant-scanning [Fig. 9(b)], introducing a sample-point skipping algorithm to compensate for accumulated timing errors caused by non-integer ratios between the laser repetition period (~13.16 ns at 76 MHz) and the digitizer sampling interval (1 ns). When errors exceeded 1 ns, temporal offsets were reset by discarding the next scheduled sample point, retaining fluorescence pulses within digitization windows. A pre-measured look-up table further mitigated laser repetition frequency fluctuations, enabling real-time quantitative visualization of autofluorescence lifetimes in deep tissues at approximately 68 ns per pixel.

However, this high-speed capability constrains measurable lifetimes (e.g., typically <~1.6 ns for 76 MHz excitation). For longer lifetimes, extended decay tails overlap with subsequent excitation pulses, leading to underestimated values as only the initial decay phase is captured within each excitation period. Employing a laser with adaptive repetition frequency via a pulse picker or cavity dumper could expand the method's applicability. Recently, a temporally and spectrally multiplexed AMD-FLIM strategy was developed for cardiovascular disease studies, incorporating multiparametric analysis based on machine learning [Fig. 9(c)]. Using a kHz-rate laser, sufficient interpulse windows were provided to simultaneously record fluorescence signals from three spectral channels with the same PMT[204]. This strategy can also be integrated with OCT for multiparametric analysis[205].

A fundamental limitation of moment-based analysis is its inability to resolve distinct lifetimes

in multi-exponential decays, as complex dynamics are simplified into an average lifetime. This restricts AMD-FLIM's applicability in real-time analysis of multiexponential signals, such as dynamic FRET measurements. Although iterative fitting has been attempted to resolve bi-exponential decays, it requires sampling rates as low as 300 MHz[206].

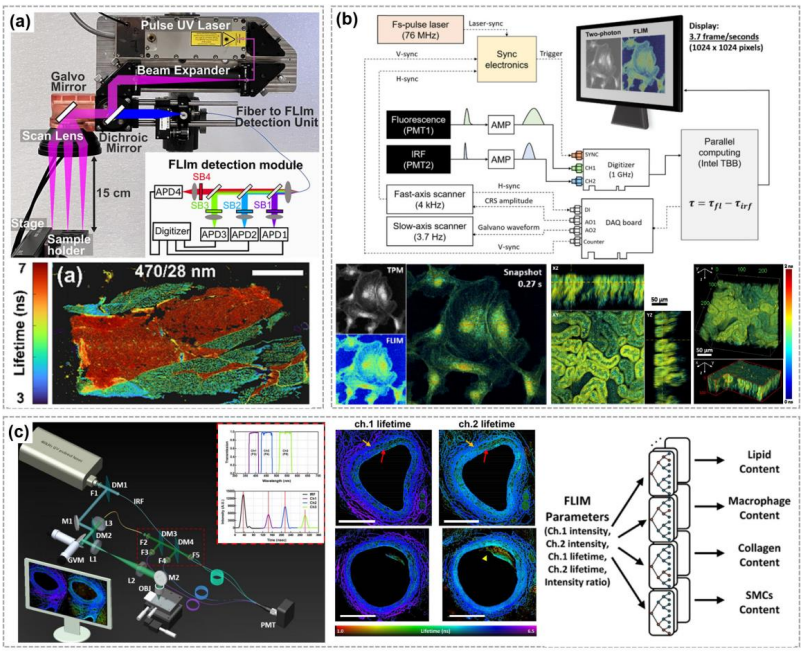

FIG. 9. Illustrations of several DPR-FLIM methodologies. (a) Instrument schematic of a scanning PS-FLIm system using APDs (Upper) and an intensity-weighted lifetime image of frozen bovine tissue (Lower)[197]. Reproduced with permission from Optics Letters, **50**, 900-903 (2025). Copyright 2025 Optica Publishing Group. (b) Schematic of a two-photon AMD-FLIM system (Upper) and lifetime images acquired from fixed cells and mouse kidney tissue (Lower)[203]. Reproduced with permission from Biomedical Optics Express, **9**, 3449-3463 (2018). Copyright 2018 Optical Society of America. (c) Schematic of a multispectral AMD-FLIM system (Left), corresponding results from normal (Upper) and plaque-enriched (Lower) porcine coronary artery slices (Middle), and architecture of the regressor model training process (Right)[204]. J. Han, S. Kim, H. Jung Kim, H. Soo Nam, M. W. Lee, J. W. Song, J. W. Kim and H. Yoo, Arteriosclerosis, Thrombosis, and Vascular Biology, **43**, 1295-1307 (2023); licensed under a Creative Commons Attribution (CC BY) license.

2. Enabling technologies: technical solutions for high-throughput acquisition and real-time processing

Beyond the core paradigms of PS and AMD, significant efforts have been directed toward

overcoming hardware and computational bottlenecks to achieve high-throughput acquisition and real-time processing in DPR-FLIM. For instance, to capture full fluorescence decay profiles using moderate-speed digitizers, Dow et al.[207] developed an interleaved digitization technique. This method leverages the inherent beat pattern between 80-MHz laser pulses and a 500-MHz digitizer clock, enabling temporal sampling across four consecutive pulses to reconstruct a complete decay curve within a 50-ns pixel dwell window. Combined with binomial photon counting[208] and minimal electronic modifications, this streaming approach achieves 15-fps imaging with a 4-fold improvement in temporal resolution while remaining compatible with conventional two-photon microscopes.

GHz-bandwidth digitizers offer the capability to directly capture transient autofluorescence signals in live cells under ultrafast excitation, eliminating the need for signal stretching or digital oversampling. While providing better temporal resolution, these systems require simplified fitting analyses due to constrained sampling parameters and substantial computational load[209, 210]. Phasor analysis has emerged as an effective model-free alternative, enabling rapid fluorescence lifetime visualization and multicomponent resolution through linear unmixing of decay dynamics without iterative fitting[211]. Sorrells et al.[212] implemented a video-rate DPR-FLIM platform (25 fps at 256×256 pixels) incorporating GPU-accelerated real-time phasor analysis [Fig. 10(a)], which supports simultaneous acquisition, processing, and interactive visualization of lifetime data without post-processing latency. Their system performs pixelwise phasor transformations within the acquisition pipeline, compressing raw GHz-waveform data via spatial binning while retaining full temporal information for online quantitative analysis.

Within this integrated hardware-software framework, computational single-photon counting techniques further extend the dynamic range of DPR-FLIM. The Single-Photon Peak Event Detection (SPEED) method, for example, achieves count rates exceeding 160 Mcps with a dead time of ~625 ps by algorithmically extracting photon events from raw waveforms recorded with PMT[213] or hybrid photodetector[214]. This enables both accelerated photon throughput (>2-fold) and accurate lifetime quantification, even under photon-saturating conditions[213]. These advances support a new paradigm for investigating multicomponent microenvironments using multimodal optical systems with real-time feedback[215]. Furthermore, the SPEED with Time-domain Analog Multiplexing (STAMP) technique eliminates clock-synchronization artifacts by directly embedding the laser trigger into silent intervals of the fluorescence decay using impedance-matched analog circuits[216]. This allows precise photon registration without additional digitizer channels and facilitates real-time multispectral lifetime mapping with low-repetition-rate lasers. Although STAMP introduces analog noise that requires computational compensation and remains reliant on specialized high-bandwidth hardware, it effectively bridges the precise synchronization of TCSPC with the high imaging speed of DPR-FLIM, broadening the applicability of high-throughput FLIM in biomedical research.

Flow cytometry represents a classic high-throughput technique for single-cell analysis, with capable of processing thousands of events per second and having profoundly impacted immunology and clinical diagnostics[217]. While earlier integrations with time-domain fluorescence lifetime measurements showed promise for screening biomolecular interactions[122, 218], their limited spatial resolution restricted the interrogation of complex cellular microenvironments. Recently, Karpf et al.[219] introduced a two-photon DPR-FLIM method that achieves 88 million pixels per second (equivalent to ~2,000 fps at 256×170 pixels) through spectro-temporal encoding while

maintaining sub-micron lateral resolution. As illustrated in Fig. 10(b), the system employs a wavelength-swept Fourier Domain Mode-Locked (FDML) laser[220], combined with diffraction-grating angular dispersion to spatially encode one imaging axis spectrally. A high-speed electro-optic modulator (EOM) digitally segments each wavelength sweep into 256 discrete pulses of 65 ps duration, enabling inertia-free, pixel-resolved scanning via programmable pulse modulation. A galvanometer scanner covers the orthogonal axis, allowing direct recording of fluorescence decays across the entire FOV using a high-bandwidth digitizer at unprecedented frame rates. Although photon collection efficiency ultimately governs the trade-off between imaging speed and lifetime accuracy, these advanced DPR-FLIM techniques establish a critical foundation for future high-throughput screening with multicomponent resolution.

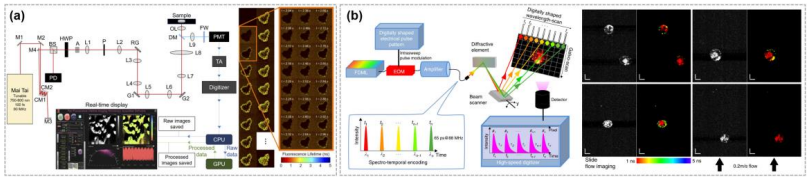

FIG. 10. High-speed DPR-FLIM systems for high-throughput applications. (a) GPU-accelerated real-time phasor analysis system (Left) and a 25-fps recording of Rhodamine B diffusion dynamics in live cells (Right)[212]. Reproduced with permission from Biomedical optics express, **12**, 4003-4019 (2021). Copyright 2021 Optical Society of America. (b) Spectro-temporal encoded DPR-FLIM integrated with flow cytometry (Left) and imaging of Euglena gracilis algal cells at a flow speed of 0.2 m/s (Right)[219]. S. Karpf, C. T. Riche, D. Di Carlo, A. Goel, W. A. Zeiger, A. Suresh, C. Portera-Cailliau and B. Jalali, Nature Communications, **11**, 2062 (2020); licensed under a Creative Commons Attribution (CC BY) license.

E. Advancements in Frequency-Domain FLIM

Despite significant advantages in imaging speed and analysis simplicity, frequency-domain FLIM techniques face inherent trade-offs in photon efficiency and measurement precision. Since lock-in detection relies on averaging signals over multiple modulation cycles, low-intensity fluorescence components often suffer from reduced phase accuracy[185], while resolving multi-exponential decays ($\tau_M \neq \tau_\phi$) typically requires multi-frequency modulation or iterative unmixing techniques[221]. Consequently, a central theme in modern frequency-domain FLIM development has been to create systems that not only detect but also quantitatively resolve this complexity. Furthermore, the absence of explicit fitting procedures necessitates meticulous calibration of modulation frequency, detector response, and reference phase stability to minimize systematic errors. Recent innovations have focused on transforming these inherent characteristics into robust and practical performance through two complementary approaches: advanced demodulation/data acquisition architectures and application-specific system designs. The following subsections detail these developments which empower frequency-domain FLIM to accurately deconvolve multi-exponential decays, thereby establishing frequency-domain FLIM as a powerful tool for rapid, application-oriented biomedical measurements.

1. Demodulation and data acquisition architectures

The accuracy of frequency-domain FLIM fundamentally depends on the faithful capture of modulated fluorescence waveforms. While the Nyquist theorem dictates a minimum sampling rate of 20 MHz for a 10 MHz modulation signal, such sampling provides only two data points per cycle—insufficient for resolving subtle phase shifts and modulation depths that encode fluorescence lifetimes. Practical implementations therefore employ substantial oversampling, significantly exceeding the modulation frequency to suppress timing jitter, enhance noise robustness, and enable precise extraction of phase delays and modulation ratios. Complementing this strategy, high bit-depth digitization (typically 14 or 16 bits) expands dynamic range and improves SNR, further refining lifetime measurement accuracy.

Demonstrating the effective implementation of these principles, Serafino et al.[222] developed a novel frequency-domain FLIM system utilizing FPGA with 14-bit digitization at 250 MS/s to simultaneously capture fluorescence signals across three spectral bands. This design significantly oversampled modulation frequencies ranging from 1 to 83 MHz. Crucially, they implemented direct discrete Fourier transform (DFT) computation on the FPGA, enabling real-time calculation of phase and modulation lifetimes at each pixel (12.5-kHz pixel rate) without requiring lock-in amplifiers or gain-modulated detectors. While achieving clinically relevant imaging speeds and simplifying instrumentation, the system's upper modulation frequency limit constrained its optimal sensitivity to lifetimes above approximately 2 ns.

This limitation was addressed in a subsequent advancement [Fig. 11(a)], where the integration of simultaneous dual-wavelength excitation and four-channel multispectral detection significantly enhanced system capabilities[223]. The implementation of alternating excitation modes eliminated cross-talk between dual wavelengths, while multi-harmonic DFT analysis improved measurement robustness, extending the reliably measurable lifetime range down to 0.5 ns. These enhancements were achieved within a simplified, single-FPGA architecture, further reducing system cost and complexity while maintaining the core advantages of real-time processing for clinical imaging under ambient light conditions.

While FPGA-based digitization enables real-time computation of FLIM parameters, an alternative paradigm utilizes analog signal processing to achieve instantaneous lifetime extraction, dramatically simplifying hardware requirements and eliminating computational latency. As illustrated in Fig. 11(b), Zhang et al.[46] pioneered this approach with their "instant FLIM" system based on a two-photon scanning microscope. By splitting the fluorescence signal into four paths, mixing each with phase-shifted reference signals (80 MHz) from the mode-locked laser using analog RF components, and performing basic matrix operations on the resulting DC signals, their system simultaneously streams intensity, lifetime, and phasor images at 83.3-kHz pixel rates. This throughput was limited only by galvo scanner bandwidth, while analog signal processing introduced negligible latency (2 ns/pixel). Comparative studies demonstrated that two-photon frequency-domain FLIM requires nearly half the photons of conventional one-photon implementations to achieve equivalent SNR, with incorporation of harmonic components potentially doubling the effective measurement rate[47]. Although optimal for fluorophores with lifetimes below 4.5 ns due to the fixed modulation frequency and requiring careful electronic shielding to minimize noise, the cost-effectiveness and open-source software framework of instant FLIM significantly enhance accessibility for dynamic studies. Furthermore, the scalability of this

approach was demonstrated by Li et al.[224] through integration of instant frequency-domain FLIM with Bessel-beam volumetric excitation and deep-learning denoising to achieve high-speed 3D neurodynamics mapping.

2. Application-specific system designs

Beyond core demodulation technologies, the flexibility of frequency-domain FLIM has enabled its adaptation to specialized imaging modalities that leverage its inherent advantages in speed and parallel detection capability. A prominent application emerges in polarization-sensitive imaging, where the ability to simultaneously acquire multiple phase-sensitive measurements proves particularly valuable. Time-resolved fluorescence anisotropy (TR-FA) monitors the temporal decay of fluorescence polarization to probe molecular rotational dynamics and local microenvironmental viscosity[225]. Conceptually, this requires simultaneous acquisition of fluorescence lifetime signals in orthogonal polarization channels and analysis of their anisotropy decay kinetics. Conventional implementations face significant limitations: TCSPC-FLIM typically necessitates two hybrid photomultiplier tubes and extended acquisition times[226], while TG-FLIM often provides inadequate temporal resolution of several hundred picoseconds[227].

To overcome these constraints, Yahav et al.[228] developed a novel TR-FA methodology based on wide-field frequency-domain FLIM, integrating simultaneous polarization-resolved detection via a PBS with homodyne phase-sensitive imaging. As shown in Fig. 11(c), their system employs multi-frequency LED modulation at tens of MHz and gain-modulated image intensifier detection to concurrently extract phase shifts and modulation depths for both vertical and horizontal polarization components. The system quantified viscosity-dependent rotational correlation times in fluorescein-glycerol solutions with 80-ps temporal resolution and revealed nanoscale rotational dynamics in carbon dot-gold conjugates. However, reliance on mono-exponential anisotropy decay models may oversimplify complex rotational behaviors in heterogeneous microenvironments, and the PBS optical path requires meticulous leakage correction for quantitative accuracy. This approach establishes a robust framework for high-speed microviscosity mapping in synthetic systems, though cellular applications remain to be explored.

Benefiting from rapid and simplified lifetime extraction, frequency-domain methods show significant promise for high-throughput flow cytometry. Historical implementations lacked spatial resolution due to extremely short cell transit times through the detection volume[229-231]. Kanno et al.[232] recently overcame this limitation by developing a high-throughput frequency-domain FLIM flow cytometer [Fig. 11(d)]. Their platform employs AODs to generate and scan dual intensity-modulated continuous-wave laser beam arrays with complementary frequency pairs spanning 21-222 MHz. A Wollaston prism separates these orthogonally polarized beams, enabling spatial inversion of one beam array to interrogate identical cellular positions simultaneously. Fluorescence signals are resolved by two avalanche photodiodes detecting spatially separated emission channels, permitting parallel acquisition of amplitude and phase image pairs. This strategy enabled frequency-domain FLIM at rates exceeding 10,000 cells/s with sub-micrometer resolution in a 3-m/s flow system, while maintaining robustness against intensity artifacts. Although constrained to lifetimes of a few nanoseconds due to the modulation frequency range and potentially underestimating absolute lifetime values for multi-exponential decays compared to time-domain methods, this approach represents a transformative advance in high-throughput, image-based cellular analysis using frequency-domain FLIM. In general, frequency-domain FLIM

is particularly well-suited for applications prioritizing rapid, qualitative lifetime mapping over the highest-precision, fully quantitative kinetic analyses.

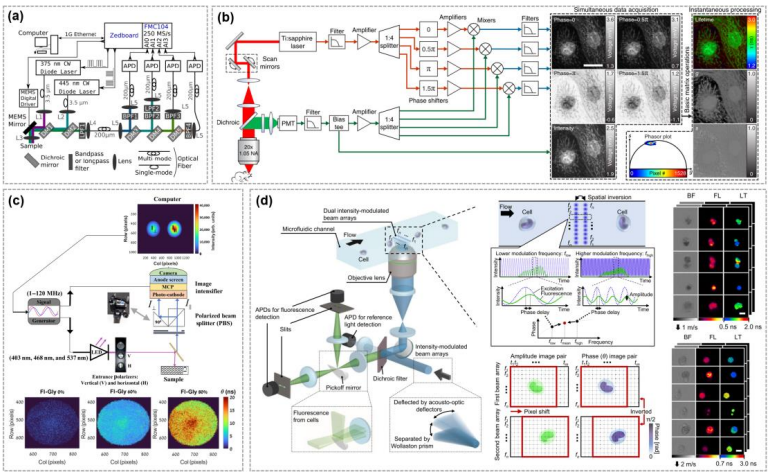

FIG. 11. Recent advances in frequency-domain FLIM techniques. (a) Schematic of digital frequency-domain strategy exploiting dual-wavelength excitation with four detection channels in a single FPGA architecture[223]. Reproduced with permission from Biomedical Optics Express, **14**, 1608-1625 (2023). Copyright 2023 Optica Publishing Group. (b) Schematic of the instant FLIM system (Left) and step-by-step operations to obtain lifetime images of BPAE cells (Right)[46]. Reproduced with permission from Optica, **8**, 885-897 (2021); Copyright 2021 Optical Society of America. (c) Schematic of TR-FA based on frequency-domain FLIM (Upper), and imaging results of rotational correlation time in fluorescein-glycerol solutions with different glycerol concentrations (Lower)[228]. Y. Gilad, P. Shweta, W. Yitzchak, A. Bar, D. Hamootal and F. Dror, Journal of Biomedical Optics, **28**, 056001 (2023); licensed under a Creative Commons Attribution (CC BY) license. (d) Schematic of the high-throughput flow cytometry based on frequency-domain FLIM (Left), and imaging results of rat glioma cells (Upper) and human Jurkat cells (Lower) stained with SYTO16 (Right)[232]. H. Kanno, K. Hiramatsu, H. Mikami, A. Nakayashiki, S. Yamashita, A. Nagai, K. Okabe, F. Li, F. Yin, K. Tominaga, O. F. Bicer, R. Noma, B. Kiani, O. Efa, M. Büscher, T. Wazawa, M. Sonoshita, H. Shintaku, T. Nagai, S. Braun, J. P. Houston, S. Rashad, K. Niizuma and K. Goda, Nature Communications, **15**, 7376 (2024); licensed under a Creative Commons Attribution (CC BY) license.

F. Comparison of Advanced FLIM Techniques

The rapid evolution of FLIM has led to a diverse system of advanced techniques, each offering distinct trade-offs in temporal resolution, acquisition speed, photon efficiency, and system complexity. As detailed throughout this chapter, both time-domain and frequency-domain FLIM modalities have seen substantial improvements. To provide a clear overview of these developments and guide researchers in selecting the appropriate technology for specific biological or clinical applications, we present a comparative summary in Table I. This table synthesizes key

performance metrics and features of each advanced FLIM technique, highlighting their respective advantages, limitations, and ideal use cases within modern bioimaging. Reported values are indicative ranges drawn from the literature rather than hard limits, since performance depends on fluorophore properties, sample optics, and configuration choices. Similarly, typical photon rate and lifetime range represent its optimal performance for biomedical applications with common fluorescence probes.

As evidenced by the comparative data in Table I, the selection of a FLIM modality is fundamentally a process of balancing these core performance parameters. For instance, TCSPC-FLIM remains the gold standard for applications demanding the high temporal precision and quantitative accuracy for complex decay kinetics, such as FRET analysis, although often at the cost of frame rate. In contrast, time-gated and frequency-domain methods offer superior imaging rates, making them ideal for capturing dynamic physiological processes or for high-throughput screening, though sometimes with compromises in lifetime resolution or the handling of multi-exponential decays. The unparalleled temporal resolution of streak camera positions it as the premier tool for investigating ultrafast phenomena. Furthermore, its integration with computational imaging approaches, such as compressed sensing, is actively expanding its utility into high-speed wide-field biological imaging. Meanwhile, direct pulse-recording techniques excel in high-throughput scenarios where extreme speed is paramount and single-exponential or average lifetime readouts are sufficient. Ultimately, the convergence of advanced detectors (e.g., SPAD arrays), parallel processing, and computational algorithms is progressively blurring these traditional boundaries, enabling newer systems to offer improved combinations of speed, sensitivity, and resolution.

TABLE I. Comparison of advanced FLIM techniques.

Methods	Light source	Detector	Temporal resolution	Frame rate	Typical Photon rate range (s^{-1})	Typical lifetime range	Advantages	Main limitations	Suitable applications
TCSPC	Pulsed laser	APD; Hybrid PMT; SPAD array; SNSPD	~250 ps[51]; 25 ps[53]; ~109 ps[67]; 50 ps[85];	20 fps @ 64×64 pixels[51]; ~6 fps @ 256×256 pixels[53]; 7.8 fps @ 16×16 pixels[102]; 4 fps @ 512×512 pixels[116]	~1 - 10 MHz	~20 ps - 50 ns	High timing accuracy; High photon efficiency; Well-established hardware	Low frame rate; Pile-up effect; Counting loss by dead time	High-precision *in vitro* research; FRET analysis
Time-gated		ICCD; SPAD array; Pockels cell and camera	~550 ps[168]; ~3 ps[141]; ~17.9 ps[74]	1 fps @ 120×128 pixels[168]; 1000 fps[141]	~0.1 - 100 MHz	~1 ns - 50 ns (Capable of measuring phosphorescence lifetime)	Good compatibility with wide-field imaging; High frame rate	Restricted optical section capability and multi-exponential analysis	Large field of view imaging; High-throughput screening; Voltage dynamics in live neurons
Streak camera		Streak camera with/without a slit	6.5 ps[172]; ~50 ps[174]; 0.8 ps[233]	100 fps @ 500×400 pixels[175]	~1 - 100 MHz	~100 ps - 50 ns	High timing accuracy; High imaging speed in one-dimensional space	Expensive and complex system; Additional decoding under wide-field imaging	Transient physical/ chemical events
Direct pulse-		MCP-PMT; APD;	> 1 ns[212]	7.7 fps @ 158×127 pixels[201];	>200 MHz[199]	~1 ns - 20 ns	High frame rate;	Requires high-speed	Clinical real-time

recording		PMT		3.8 fps @ 1024×1024 pixels[202, 203]; 25 fps @ 256×256 pixels[212]; 2000 fps @ 256×170 pixels[219]			Applicable to ambient light	digitizer; Incompetent multi-exponential analysis	diagnosis; Flow cytometry imaging
Frequency-domain	Modulated continuous wave/pulsed laser or LED	CCD/sCMOS camera; PMT	~80 ps[228]	~1.3 fps @ 256×256 pixels[46]; ~12 fps @ 1008×1008 pixels[43]; ~16,000 fps @ 190×231 pixels [234]	~1 - 100 MHz	~500 ps - 10 ns	High frame rate; Well-established hardware	Requires precise modulation and demodulation	Rapid, qualitative lifetime test *in vivo*; Flow cytometry imaging

IV. BIOMEDICAL APPLICATIONS

FLIM provides a powerful, label-free, and non-invasive platform for visualizing biochemical dynamics in living systems. The technological advancements detailed in the preceding sections, including the development of low-dead-time detectors and parallelized acquisition schemes for high-throughput TCSPC, the refinement of wide-field implementations via electronic and optical gating, the emergence of snapshot lifetime imaging through compressed sensing and SPAD arrays, the evolution of frequency-domain techniques enabling real-time phasor analysis, and the integration of deep learning for robust lifetime extraction under photon-starved conditions, have collectively empowered FLIM to overcome traditional limitations in speed, sensitivity, interpretability, and practicality. By quantifying the fluorescence decay kinetics of endogenous or exogenous fluorophores, FLIM achieves spatiotemporal resolution of cellular events that are often indiscernible with intensity-based imaging alone. This unique capability, now accessible in real-time and within complex physiological environments, unlocks broad and impactful biomedical applications. These are exemplified by its particularly strong utility in mapping cellular metabolism, probing microenvironmental parameters, and enhancing disease diagnosis. The following subsections detail key advances in these areas.

A. Metabolism Monitoring

1. Label-free quantitative metabolism

Metabolic activity is central to cellular function, and its dysregulation is a hallmark of numerous diseases—including cancer, neurodegeneration, and immune disorders[235]. FLIM enables quantitative visualization of metabolic processes by leveraging the intrinsic fluorescence lifetimes of key metabolic cofactors such as nicotinamide adenine dinucleotide (NADH), nicotinamide adenine dinucleotide phosphate (NADPH), and flavin adenine dinucleotide (FAD). These molecules exhibit distinct lifetime signatures in their free versus enzyme-bound states, allowing FLIM to report on cellular redox status and metabolic pathway activity, such as the balance between glycolysis and oxidative phosphorylation[236, 237].

For example, ultraviolet A1 (UVA1, 340-400 nm) irradiation induces metabolic stress in reconstructed human skin, resulting in increased protein-bound NAD(P)H and decreased bound FAD [Fig. 12(a)][238]. This shift suggests a transition toward oxidative phosphorylation or oxidative stress, potentially linked to reactive oxygen species (ROS) generation. These results underscore FLIM's sensitivity to subtle, dynamic changes in redox metabolism. Similarly, adipogenesis has been studied using FLIM to examine NAD^+ bioavailability and its regulatory role in differentiation via NAD^+-dependent deacetylases[239]. FLIM captured spatial reorganization of NADH lifetime distributions during adipogenic differentiation, offering insights into subcellular redox compartmentalization and transcriptional regulation. This non-invasive strategy provides a unique view of abnormal adipocyte differentiation and suggests therapeutic targets for metabolic disorders.

Cellular redox status and ROS levels are also critical in cancer cell proliferation and apoptosis resistance[240]. In apoptotic colorectal cancer cells, researchers concurrently imaged caspase-3 activity and NAD(P)H/FAD autofluorescence using FLIM [Fig. 12(b)][241]. The technique resolved stimulus-specific redox responses, linking ROS accumulation to elevated

mitochondrial-bound NADH and caspase-3 activation. These observations highlight the potential of redox-targeted therapies to improve drug efficacy and overcome apoptotic resistance.

In immunology, FLIM has been used to dynamically track metabolic switching in T lymphocytes upon activation [Fig. 12(c)][242]. T cell activation rapidly enhances glycolytic activity, marked by a pronounced decrease in bound NAD(P)H fraction. Three-dimensional FLIM further revealed spatial reordering of NADH lifetimes—particularly at the immune synapse—implying crosstalk between actin remodeling and metabolic reprogramming[242]. In tumor immunology, T cell metabolism is closely tied to tumor infiltration and cytotoxic function[243], positioning FLIM as a valuable tool for assessing tumor-specific T cell activity and supporting immunotherapy development.

In Alzheimer's disease (AD), significant metabolic alterations occur in both cerebrospinal fluid and blood[244, 245]. Phasor-FLIM has distinguished free and bound NADH within mitochondria, nuclei, and cytoplasm of neurons from young and aged mice as well as Alzheimer's disease models under oxidative or reductive conditions [Fig. 12(d)]. Aging and Alzheimer's disease decreased mitochondrial free NADH under oxidative stress, whereas reductive treatment restored it toward levels observed in young neurons, highlighting reversible subcellular redox deficits associated with aging and neurodegeneration[246]. FLIM has also revealed drug-induced perturbations of mitochondrial metabolism in the rat cerebral cortex, uncovering region-specific differences and providing a framework for monitoring therapeutic interventions[247]. Collectively, these findings demonstrate FLIM's ability to uncover reversible, subcellular redox deficiencies linked to aging and neurodegeneration.

Microglia, the resident immune cells of the central nervous system, undergo metabolic reprogramming during Alzheimer's disease progression[248]. Specific microglial phenotypes align with distinct metabolic programs, and activation shifts metabolism from oxidative phosphorylation to glycolysis while promoting release of pro-inflammatory mediators that drive neurodegeneration[248, 249]. FLIM analysis showed that lipopolysaccharide-induced microglial activation significantly altered NADH fluorescence lifetime and the free-to-bound NADH ratio, confirming NADH lifetime as a sensitive, label-free indicator of microglial activation[250].

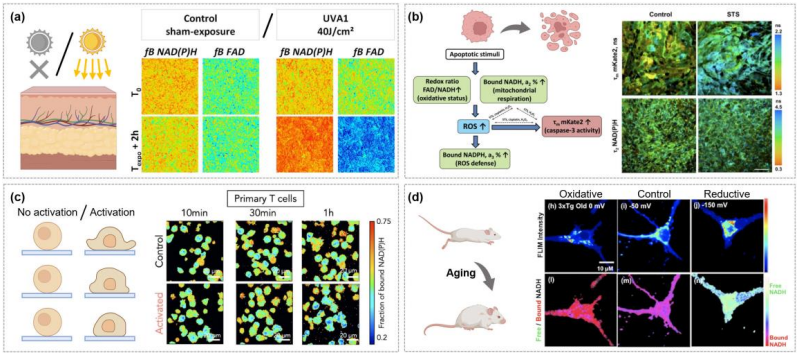

FIG. 12. Applications of label-free FLIM in quantitative metabolic analysis. (a) Representative NAD(P)H and FAD FLIM images of keratinocytes under control (sham-exposure) and UVA1 irradiation (40 J/cm^2) conditions. FLIM images revealed a progressive increase in the fraction of bound NAD(P)H and a decrease in bound FAD

following UVA1 exposure, indicating metabolic stress[238]. T. P. L. Ung, S. Lim, X. Solinas, P. Mahou, A. Chessel, C. Marionnet, T. Bornschlgl, E. Beaurepaire, F. Bernerd and A. M. Pena, Scientific Reports, **11**, 1-15 (2021); licensed under a Creative Commons Attribution (CC BY) license. (b) FLIM imaging of FRET-based sensor of caspase-3 activity (mKate2) and NAD(P)H in CT26 tumors before (control) and after treatment with staurosporine (STS). Apoptotic cells in treated tumors showed prolonged mKate2 fluorescence lifetime[241]. M. V. Shirmanova, A. I. Gavrina, T. F. Kovaleva, V. V. Dudenkova, E. E. Zelenova, V. I. Shcheslavskiy, A. M. Mozherov, L. B. Snopova, K. A. Lukyanov and E. V. Zagaynova, Scientific Reports, **12**, 4476 (2022); licensed under a Creative Commons Attribution (CC BY) license (c) NAD(P)H FLIM of primary T cells before and after activation. Activation induced a time-dependent reduction in bound NAD(P)H fraction, reflecting a metabolic shift toward glycolysis[242]. N. Paillon, T. P. L. Ung, S. Dogniaux, C. Stringari, C. Hivroz and A. August, Molecular Biology of the Cell, **35**, ar11 (2024); licensed under a Creative Commons Attribution (CC BY) license. (d) External oxidative (0 mV) and reductive (−150 mV) perturbations shifted the NADH redox state in neurons from 3xTg-AD mice. Oxidative conditions increased the bound NADH fraction, while reductive conditions elevated free NADH, compared to the control (−50 mV)[246]. Y. Dong, S. Sameni, M. A. Digman and G. J. Brewer, Scientific Reports, **9**, 11274 (2019); licensed under a Creative Commons Attribution (CC BY) license.

2. Enhanced quantitative metabolism

While NAD(P)H and FAD provide intrinsic readouts of cellular metabolism, accurate detection can be limited by modest fluorescence yield, spectral overlap, and short-wavelength emission that is prone to scattering and background. To address these challenges, engineered optical probes and complementary electrochemical sensors have been developed for NADH and other redox metabolites[251, 252]. Notably, small-molecule probes, NIR fluorophores, and nanomaterial-enhanced electrodes have significantly broadened the applicability of FLIM within complex biological environments[252].

Among these exogenous probes, a red fluorescent probe with high selectivity and sensitivity has enabled nanomolar-level detection of NADH in living cells, offering real-time readouts of subtle fluctuations associated with hypoxic stress[253]. Similarly, a novel NIR-emitting fluorescent probe designed for NAD(P)H detection demonstrates exceptional selectivity over potential biological interferents, with a detection limit as low as 12 nM[254]. Its low cytotoxicity and efficient membrane permeability facilitate successful NAD(P)H bioimaging both in live cells and *in vivo*. The use of red and NIR excitation minimizes autofluorescence interference from biological tissues, thereby improving the SNR and enabling metabolite detection in complex environments.

Beyond optical and electrochemical innovations, advances in data analysis algorithms have further improved the interpretability and specificity of FLIM-derived metabolic information. Recent developments, such as the Fluorescence Lifetime Induced Redox Ratio (FLIRR), have refined metabolic readouts by enabling multi-exponential fitting of NAD(P)H and FAD signals[255]. This allows more precise quantification of protein-bound and free redox coenzymes, enhancing the discrimination between normal and tumor cells based on redox characteristics. In addition, user-friendly software tools like the Fluorescence Lifetime Ultimate Explorer (FLUTE) for phasor-based FLIM analysis have greatly simplified the interpretation and visualization of lifetime

data. FLUTE supports intuitive exploration of large datasets, lowering the technical barrier for non-specialist laboratories and accelerating the adoption of FLIM in biomedical research[256].

Collectively, these advancements illustrate how FLIM—especially when integrated with novel optical probes, electrochemical strategies, and sophisticated data analysis—has become an indispensable technique for metabolic imaging. It now offers precise, dynamic, and spatially resolved insights into cellular bioenergetics across diverse biological contexts.

Importantly, metabolic alterations are seldom confined to individual cells; rather, they engage in dynamic reciprocal interactions with the surrounding microenvironment[257]. Shifts in redox balance, nutrient utilization, and energy flux can remodel extracellular properties such as pH, ion gradients, and mechanical stiffness. Conversely, microenvironmental stressors—including hypoxia, acidosis, and matrix stiffening—can drive metabolic reprogramming in cells. By leveraging molecular-scale insights from FLIM-based metabolic imaging, this technique can be extended to map the cellular microenvironment, offering a powerful tool for understanding the physicochemical landscape that critically regulates cell fate and therapeutic responses.

B. Microenvironment Mapping

A pivotal strength of FLIM in dissecting cellular function lies in its unique capability to map both biochemical and biophysical parameters of microenvironment with high spatial resolution. The realization of this capability, however, usually depends on the development of specially designed fluorescent probes whose fluorescence lifetimes are exquisitely sensitive to specific local conditions. Recent years have witnessed the rational design of a diverse array of such FLIM-optimized probes. These include molecular rotors that report on microviscosity, environment-sensitive dyes that shift their lifetime in response to polarity or pH, and genetically encoded biosensors that transduce ion concentration or protein-protein interactions (via FLIM-FRET) into lifetime changes. Some representative applications of these probes are summarized in Table II, which serves as a guide for considering the appropriate molecular tool for specific microenvironmental parameters. The following subsections detail how the probes are revolutionizing our understanding of cellular microenvironments.

TABLE II. Summary of fluorescent probes optimized for FLIM.

Microenvironment		Examples	Applications	Category
Biochemistry	pH	mApple[258]	Quantitative analysis of pH in subcellular organelles	Protein
		Carbon Dots[3]		Nanoprobe
		Fluorescein[259]	Tumor recognition by endomicroscopy	Dye
	Enzyme	LSS-mOrange-DEVD -mKate2[260]	Quantitative analysis of cell apoptosis	Protein
		paCaMKII[261]	Manipulation of synaptic plasticity	Protein
		Turquoise2- mVenus[1]	Study the conformational changes of Lck in cells	Protein
	Serum albumin	Squaraine[12]	Dynamics of tumor cell endocytosis	Dye

		Indocyanine green[262]	Tumor recognition in vitro or *in vivo*	Dye
	Amyloid-β	ZW800-1C[263]	Study of Alzheimer's disease *in vivo*	Dye
	ATP	mTurquoise2[264]	Energy changes within living cells	Protein
		FX2-$MnCl_2$[265]	Lysosome-targeted ATP migration	Dye
	Ca^{2+}	Oregon Green BAPTA1[10]	Characteristic of nanomolar-range concentrations in acute brain slices	Dye
		WHaloCaMP[266]	Ca^{2+} imaging *in vivo*	HaloTag
Biophysics	Density	mCherry[267]	Depletion of heterochromatin protein 1α condensates during cellular differentiation	Protein
		AlexaFluor 546 and AlexaFluor 647[268]	DNA compaction and gene activities during cell cycle	Dye
	Tension	A family of Flipper[6]	Measurement of mechanical forces in subcellular organelles	Protein
	Temperature	HPS/Butter/DSPE-PEG-Biotin[269]	AIE-based nano-thermometer sensing in living cells	Nanoprobe
	Viscosity	BODIPY[270]	Membrane lipid composition of differentiated cells	Dye
	Polarity	TBPCPP[4]	Changes of polarity with lipid droplets accumulation in living cells	Dye
		SiR-Aβ[271]	Characteristic of amyloid-β plaques *in vivo*	Dye

1. Biochemical microenvironment

The cellular microenvironment is tightly regulated by various biochemical parameters, including pH, adenosine triphosphate (ATP), ion concentration, redox state, protein crowding and so on, all of which orchestrate cellular metabolism, signaling, and survival[272]. Subtle fluctuations in these variables reshape enzymatic activity, influence ion-channel function, and modulate gene-expression programs, ultimately determining cell fate in health and disease. Dysregulation of these biochemical cues is frequently observed in diseases such as cancer, neurodegeneration, and

metabolic disorders[273]. FLIM enables quantitative, subcellular mapping of these parameters, either via intrinsic lifetime readouts of endogenous cofactors or through rationally designed, environment-sensitive probes, thereby supporting real-time visualization of biochemical dynamics in living systems[127, 274].

Intracellular pH regulates enzyme activity, ion transport, and signaling, and its dysregulation accompanies cancer progression, hypoxia, and therapy resistance[275]. FLIM-based pH sensing leverages the pH-dependent lifetimes of fluorescent proteins or synthetic dyes to overcome intensity-based uncertainties and achieve quantitative, spatially resolved maps. For instance, genetically engineered pH-sensitive proteins targeted to the cytosol, endosomes, and lysosomes have enabled precise quantification of pH within individual vesicles and revealed compartment-specific acidification dynamics in response to drugs [Fig. 13(a)][258]. In tumor, lifetime-based pH imaging has visualized hypoxia-associated acidification in tumor cores and tracked chemotherapy-induced pH shifts alongside metabolic state. Additionally, quantum-dot lifetime probes further extend pH measurements to very low probe concentrations with high photostability[276]. Collectively, these advances establish FLIM as a robust platform for probing pH heterogeneity in living systems.

In the cellular microenvironment, bovine serum albumin (BSA) binds, transports, and delivers fatty acids, porphyrins, bilirubin, and steroids. A recent study reported the development of squaraine dye that selectively detects BSA using FLIM, thereby enabling real-time monitoring of BSA endocytosis in live cells [Fig. 13(b)][12]. This approach revealed that BSA uptake process is concentration-dependent, highlighting the potential of using FLIM to quantify BSA concentrations and investigate physiological mechanisms relevant to chemotherapeutic drug action.

ATP provides energy to drive many essential biological processes in living organisms. ATP biosensors are valuable tools for evaluating the spatiotemporal dynamics of ATP within a single cell. Recently, a FLIM biosensor for ATP detection was established by integrating specific sensing domains into the fluorescent protein [Fig. 13(c)][264]. The ATP-dependent conformational changes alter the chromophore microenvironment and modulate fluorescence lifetime, enabling quantitative ATP imaging.

In brain science, maintaining low intracellular calcium (Ca^{2+}) concentration is essential for neuronal and glial function, yet the underlying mechanisms remain incompletely understood[277]. Modern Ca^{2+} indicators have enabled high-resolution monitoring of resting Ca^{2+} levels and Ca^{2+} dynamics in neurons and astroglia in situ, revealing heterogeneous baseline landscapes that depend on age and prior activity. Such landscapes, obtained in acute slices and *in vivo*, promise to uncover previously unexplored aspects of brain cell physiology[277]. More recently, the chemigenetic indicator WHaloCaMP, which couples bright synthetic dye-ligands to protein sensor domains, has supported *in vivo* Ca^{2+} imaging across drosophila, mice, and zebrafish [Fig. 13(d)][266]. These advances underscore the potential of chemigenetic, FLIM-compatible indicators to expand both the spectral and functional space of calcium imaging, thereby enabling multiplexed and quantitative measurements of cellular physiology in complex tissues[266]. It is important to note that the kinetics of Ca^{2+} are generally slower than the dynamics of cellular electrical activity. Quantitative characterization of these fast action potential propagation places greater demands on high-speed FLIM imaging. As mentioned above, Bowman et al. proposed the wide-field TG-FLIM with Pockels cell to achieve kilohertz frame-acquisition rates[141]. This approach can directly visualize the propagation of action potentials along axons and map subthreshold

depolarizations that were localized to specific neuronal compartments such as dendrites. Furthermore, the lifetime readout clearly distinguished two distinct classes of spikes based on amplitude and, importantly, revealed that the larger-amplitude spikes were strongly phase-locked to an external mechanical stimulus, a finding obscured in traditional intensity-based measurements. Together, these strategies continuously offer insight into how biochemical cues shape cellular behavior in native microenvironments.

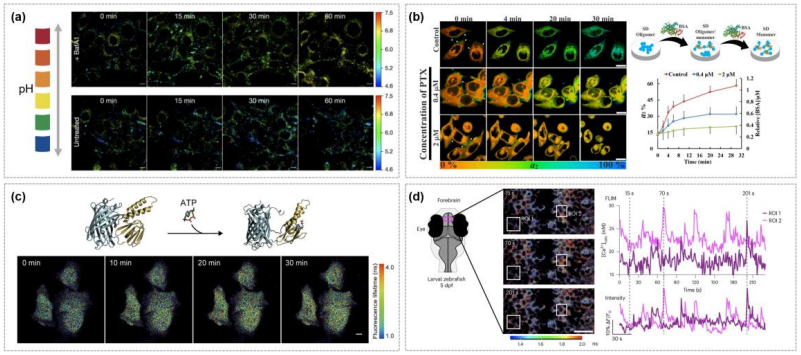

FIG. 13. Applications of FLIM in quantitative analysis of biochemical microenvironments. (a) Time-course FLIM images of cells expressing pH sensor treated or untreated with a drug[258]. J. J. Rennick, C. J. Nowell, C. W. Pouton and A. P. R. Johnston, Nature Communications, **13**, 6023 (2022); licensed under a Creative Commons Attribution (CC BY) license. (b) FLIM analysis revealed that paclitaxel treatment alters BSA endocytosis dynamics in cells. In untreated cells, BSA uptake occurred rapidly, accompanied by binding of free intracellular squaraine dye molecules, whereas paclitaxel-treated cells showed delayed endocytosis accompanied by apoptosis[12]. Reproduced with permission from Biomedical Optics Express, **11**, 149-159 (2020). Copyright 2019 Optical Society of America. (c) Schematic representation of the structural domain and three-dimensional structure models of an ATP biosensor. Sequential pseudo-color images of HeLa cells expressing the ATP biosensor in response to 2-deoxy-D-glucose[264]. C. Zhong, S. Arai and Y. Okada, Cell Reports Methods, **4**, 100902 (2024); licensed under a Creative Commons Attribution (CC BY) license. (d) Quantitative Ca^{2+} measurements by FLIM using WHaloCaMP. FLIM shows spontaneous neuronal activity in the forebrain of live zebrafish larvae[266]. H. Farrants, Y. Shuai, W. C. Lemon, C. Monroy Hernandez, D. Zhang, S. Yang, R. Patel, G. Qiao, M. S. Frei, S. E. Plutkis, J. B. Grimm, T. L. Hanson, F. Tomaska, G. C. Turner, C. Stringer, P. J. Keller, A. G. Beyene, Y. Chen, Y. Liang, L. D. Lavis and E. R. Schreiter, Nature Methods, **21**, 1916-1925 (2024); licensed under a Creative Commons Attribution (CC BY) license.

2. Biophysical microenvironment

Whereas biochemical parameters define molecular activities, the physical attributes of the microenvironment, including membrane tension, intracellular viscosity, polarity, refractive index, and temperature, provide an equally critical layer of regulation[278]. These properties shape membrane trafficking, organelle function, mechanotransduction, and stress adaptation, and many are dynamically coupled to biochemical states; for instance, changes in pH or Ca^{2+} flux often

coincide with alterations in membrane order or cytoplasmic viscosity[279, 280]. Building on advances in biochemical FLIM sensing, recent studies have extended the technique to quantify biophysical properties employing molecular rotors, polarity-sensitive probes, or thermosensitive fluorophores to directly visualize how the cellular microenvironment responds to stress, signaling, or therapeutic interventions.

Mechanical forces at the plasma membrane are central to endocytosis, exocytosis, cytoskeletal remodeling, and mechano-chemical signal pathways[281, 282]. Lifetime-based probes sensitive to lipid packing or membrane order have enabled quantitative mapping of these mechanical changes, revealing how immune cells, stem cells, or cancer cells dynamically regulate their membrane mechanics in response to external stimuli or therapeutic agents. Recently, a robust mechanosensitive fluorescence lifetime probes was introduced that supports simultaneous imaging of the plasma membrane and nuclear envelope [Fig. 14(a)][283]. FLIM readouts uncovered a dynamic mechanism of ferroptosis, in which membrane tension in both organelles decreases with the nuclear envelope exhibiting budding at advanced stages.

Temperature is a fundamental variable influencing enzyme activity, gene expression, cell division, and energy metabolism. FLIM-based thermometry has matured into a practical tool for intracellular temperature mapping with subcellular resolution and sub-degree sensitivity. A fluorescent polymeric thermometer, whose lifetime varies predictably with temperature, has enabled diffraction-limited temperature mapping and approximately 0.18–0.58°C precision. These results revealed physiologically meaningful gradients, such as nuclear, centrosomal, and mitochondrial temperatures associated with localized biochemical activity[8]. To broaden dynamic range and sensitivity, lanthanide complexes and selected molecular fluorophores with temperature-dependent excited-state kinetics have been employed, resulting in nanosecond-to-microsecond lifetime changes detectable by FLIM[284]. Such probes can be engineered for NIR excitation and emission, facilitating deeper tissue penetration. Recently, materials-driven designs have also simplified probe fabrication while maintaining performance. For example, an aggregation-induced emission (AIE)-based nanothermometer achieved high temperature resolution with reversible lifetime and intensity readouts independent of pH and ionic strength [Fig. 14(b)]. This design can incorporate diverse AIEgens with different emission wavelengths, offering versatile and customizable options for biological thermometry[269].

Viscosity is an inverse of fluidity that critically influences cell morphology and physiology[285]. Lifetime-based molecular rotors report microviscosity via concentration-independent lifetime shifts, enabling quantitative maps of intracellular crowding[286]. These approaches have revealed dynamic viscosity remodeling during cell cycle progression, oxidative stress responses[287], and apoptosis[288]. These measurements provide valuable insights into the regulation of cellular homeostasis and the mechanistic basis of pathological changes. In one report, viscosity-sensitive boron dipyrromethene-based molecular rotors quantified plasma membrane microviscosity in cancer cells undergoing cisplatin treatment [Fig. 14(c)][288]. High-resolution FLIM measurements showed a sustained increase in membrane viscosity in viable cancer cells, both in monolayers and tumor spheroids, after prolonged cisplatin treatment, as well as in a cisplatin-adapted cell line. These findings underscore the potential of FLIM-based biophysical measurements to uncover subcellular mechanisms of treatment response.

Polarity-sensitive probes exhibit lifetime shifts in response to changes in lipid packing, enabling quantification of membrane order and tension during processes such as immune cell

activation. Lysosomal polarity is another key microenvironmental parameter that changes during organelle interactions, autophagic flux, and aging. Recent FLIM studies with polarity probes have visualized these subtle dynamics in real-time[283]. For instance, a red-emission fluorescent probe rapidly labels lysosomes within one minute after incubation, providing polarity-dependent long lifetimes with excellent photostability and biocompatibility[289]. FLIM revealed increases in lysosomal polarity during lipophagy and mitophagy [Fig. 14(d)]. Imaging in cancer cells further indicated that lysosomal polarity can sensitively report pathological state. These findings illustrate how polarity-sensitive FLIM probes expand the toolkit for probing organelle dynamics and microenvironmental regulation in both physiological and disease contexts.

Collectively, FLIM-based mapping of biophysical cues provides quantitative, noninvasive, and subcellular readouts that complement biochemical lifetime sensors. This integrated view helps decode how physical and chemical signals co-regulate cellular behavior in native microenvironments and supports translational applications in diagnosis, therapy monitoring, and drug screening.

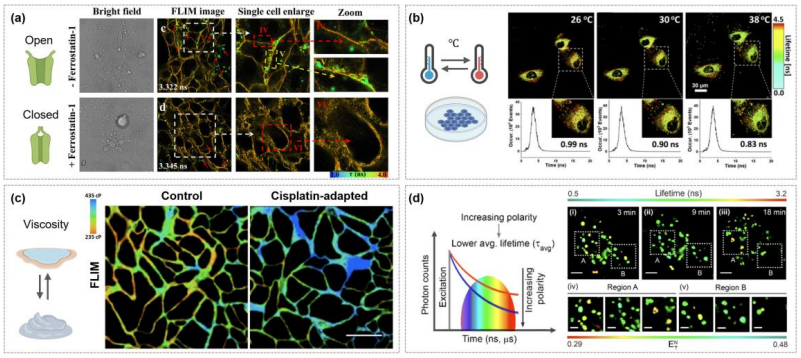

FIG. 14. Applications of FLIM in quantitative analysis of biophysical microenvironment. (a) FLIM imaging revealed distinct membrane repair responses during ferroptosis. After erastin treatment, cells without ferrostatin-1 exhibited only slow, localized membrane repair mediated by exocytosis, whereas supplementation with ferrostatin-1 enabled global and continuous membrane restoration[283]. X. Liang, Y. Zhao, J. Yan, Q. Zhang, T. D. James and W. Lin, Proceedings of the National Academy of Sciences, **121**, e2316450121 (2024); licensed under a Creative Commons Attribution (CC BY) license. (b) *In vitro* fluorescence lifetime images and corresponding fluorescence decay curves of live cells measured at indicated temperature[269]. H. Gao, C. Kam, T. Y. Chou, M.-Y. Wu, X. Zhao and S. Chen, Nanoscale Horizons, **5**, 488-494 (2020); licensed under a Creative Commons Attribution (CC BY) license. (c) Mapping cisplatin-induced viscosity alterations in cancer cells. Cisplatin-adapted cells maintained similar morphology and proliferation rates compared to non-adapted counterparts; however, the plasma membrane viscosity was significantly higher in cisplatin-adapted cells[288]. L. E. Shimolina, A. A. Gulin, M. Paez-Perez, I. López-Duarte, I. N. Druzhkova, M. M. Lukina, M. V. Gubina, N. J. Brooks, E. V. Zagaynova, M. K. Kuimova and M. V. Shirmanova, Journal of Biomedical Optics, **25**, 126004 (2020); licensed under a Creative Commons Attribution (CC BY) license. (d) Schematic illustration of the relative variation in average fluorescence lifetime as a function of solvent polarity. Time-lapse FLIM

images of HeLa cells demonstrate dynamic changes in lysosomal polarity[289]. S. Das, A. Batra, S. Kundu, R. Sharma and A. Patra, Chemical Science, **15**, 102-112 (2024); licensed under a Creative Commons Attribution (CC BY) license.

C. Disease Diagnosis

The diagnostic utility of FLIM lies in its ability to provide quantitative, label-free, and spatially resolved information about the biochemical and structural state of biological tissues. By leveraging the distinct lifetime signatures of endogenous autofluorophores and targeted exogenous probes, FLIM enables early disease detection, objective pathological grading, and real-time treatment monitoring. Current applications span cancer[290], neurodegenerative disorders[291], cardiovascular disease[292], and inflammatory conditions. This subsection highlights recent advances in these major domains, progressing from *in vitro* to *in vivo* applications and from label-free to targeted strategies.

1. Label-free histopathological diagnosis in vitro

Endogenous fluorophores such as NAD(P)H, FAD, and lipofuscin have emerged as powerful intrinsic reporters for tissue characterization without the need for exogenous stains. These reporters are integral to cellular metabolism, making FLIM a particularly attractive modality for histopathological evaluation with quantitative biochemical contrast[293].

In oncology, FLIM of NAD(P)H and FAD has been applied to frozen or paraffin-embedded tissue sections to discriminate malignant from normal tissue based on redox state and enzyme-binding differences. Malignant tissue commonly shows a shift towards glycolytic metabolism known as Warburg effect[294], which manifests as decreased bound-NADH lifetimes and altered FAD lifetimes[257]. For example, by exciting endogenous FAD in frozen sections and analyzing its fluorescence decay, FLIM quantified the mean lifetime and the free-to-bound FAD ratio to probe tumor microenvironment metabolism [Fig. 15(a)]. Coupling FLIM with spectral phasor analysis further corroborated metabolic distinctions and collagen degradation patterns, demonstrating noninvasive, real-time discrimination of basal cell carcinoma progression from FAD lifetime signatures[58]. FLIM has also differentiated brain tumors from freshly excised healthy tissue[295]. Specifically, glioblastomas exhibited a statistically significant increase in the relative amplitude of the short-lifetime component compared to non-infiltrated peritumoral white matter[296]. Similarly, lifetime-based metabolic signatures in human breast biopsy specimens enabled stratification by tumor grade[297]. In colorectal cancer[298], NADH lifetime heterogeneity has been quantified in patient tissues [Fig. 15(b)], highlighting the potential of FLIM to inform clinical decision-making from early diagnosis to treatment planning by providing noninvasive biomarkers of heterogeneity, aggressiveness, and therapeutic response.

Lipofuscin, a heterogeneous mixture of oxidized proteins and lipids accumulating with age and oxidative stress, is another valuable endogenous fluorophore for diseases assessment[299]. Its characteristically long lifetime distinguishes it from metabolic cofactors, and lifetime maps have revealed differential accumulation between tumor and non-tumor regions in melanoma and hepatocellular carcinoma[300]. This intrinsic signal can serve as a surrogate marker of cell death, complementing metabolic readouts from NAD(P)H/FAD.

In summary, label-free FLIM of endogenous fluorophores is non-destructive, preserves tissue for downstream analyses, and provides molecular-level information beyond morphology[299, 301].

Across multiple disease contexts *in vitro*, FLIM has shown substantial diagnostic value and is poised to complement or enhance conventional histopathology for more precise diagnosis and prognosis.

2. Probes-based histopathological diagnosis in vitro

When endogenous contrast is insufficient for definitive diagnosis, FLIM combined with targeted fluorescent probes offers enhanced biochemical specificity. Tumor sections stained with microenvironment-sensitive dyes reveal lipid-metabolic reprogramming through lifetime mapping[302]. In neurodegenerative pathology, amyloid-binding dyes exhibit disease-specific lifetime shifts that improve plaque discrimination[303]. Such lifetime readout is largely decoupled from probe concentration, supporting reproducible, quantitative comparisons across samples, and making FLIM-compatible staining a powerful complement to routine histology.

For instance, Hematoxylin and Eosin (H&E)-stained sections analyzed by FLIM have been used to trace infiltration trajectories of basophils and other immune cells in preneoplastic and neoplastic skin lesions [Fig. 15(c)][304]. Integrating the phasor approach with standard histology demonstrated practical value for skin-cancer early detection. FLIM has also been applied to quantify HER2-HER3 heterodimerization formation in paraffin-embedded breast cancer tissues. High dimerization predicted metastatic relapse within 10 years post-surgery, identifying HER2-HER3 dimerization as a prognostic biomarker for metastasis risk[305]. Notably, FLIM for ICG has been confirmed availability of high-contrast recognition in several human solid tumors, including liver, head and neck, bone and soft tissue sarcomas, glioblastoma, and in metastatic lymph nodes[262]. ICG binds serum proteins and preferentially accumulates in cancer cells. FLIM revealed significantly longer ICG lifetimes in tumor than in adjacent normal tissue[306], suggesting a broadly applicable, real-time intraoperative marker to guide precise resection across diverse tumor types.

In summary, FLIM has expanded diagnostic and prognostic capabilities through both endogenous and exogenous contrast. A key caveat is that standard tissue processing—notably formalin-fixation and paraffin-embedding—can alter or obscure endogenous NAD(P)H lifetime signatures critical for metabolic assessment[307], which limits analysis of metabolic dysfunction in processed clinical samples.

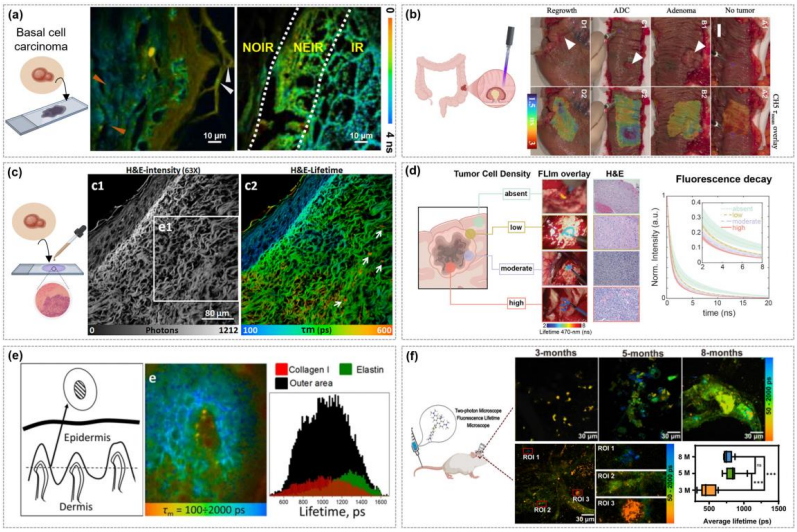

FIG. 15. Applications of FLIM in diagnosis and therapeutic assessment. (a) In normal skin, epidermal and dermal layers showed significantly different average lifetimes. The regions indicated by orange arrows showed prolonged lifetimes, whereas the particles in the stratum corneum exhibited shorter ones. NOIR: non-invasive region; NEIR: near-invasive region; IR: invasive region[58]. F. Guo, F. Lin, B. Shen, S. Wang, Y. Li, J. Guo, Y. Chen, Y. Liu, Y. Lu, R. Hu, J. He, C. Liao, Y. Wang, J. Qu and L. Liu, Nanophotonics, **13**, 217-227 (2024); licensed under a Creative Commons Attribution (CC BY) license. (b) Autofluorescence lifetime maps of colorectal tissues with and without tumors are shown. Average lifetime parameters were calculated for normal, adenoma, and adenocarcinoma tissues across all non-irradiated specimens[298]. A. I. Herrando, L. M. Fernandez, J. Azevedo, P. Vieira, H. Domingos, A. Galzerano, V. Shcheslavskiy, R. J. Heald, A. Parvaiz, P. G. da Silva, M. Castillo-Martin and J. L. Lagarto, Scientific Reports, **14**, 24575 (2024); licensed under a Creative Commons Attribution (CC BY) license. (c) Intensity and FLIM images were directly obtained from H&E-stained basal-cell carcinoma sections. Shorter lifetimes originate from the epidermis, while longer lifetimes come from the dermis[304]. T. Luo, Y. Lu, S. Liu, D. Lin and J. Qu, Analytical chemistry, **89**, 9224-9231 (2017); licensed under a Creative Commons Attribution (CC BY) license. (d) Schematic of the tumor margin measurements performed around the resection margins showing areas of various degrees of tumor cell density (absent, low, moderate, and high) and corresponding H&E images, and a representative fluorescence decay curve for each group[308]. Reproduced with permission from Biomedical Optics Express, **14**, 2196-2208 (2023). Copyright 2023 Optica Publishing Group. (e) Schematic of skin structure showing the papillary dermis cross-section (dashed line) and dermal papilla with surrounding capillary (outer and inner circles). FLIM image maps pixel colors to mean fluorescence lifetimes and their distributions[309]. E. A. Shirshin, Y. I. Gurfinkel, A. V. Priezzhev, V. V. Fadeev, J. Lademann and M. E. Darvin, Scientific Reports, **7**, 1171 (2017); licensed under a Creative Commons Attribution (CC BY) license. (f) FLIM tracked Aβ

plaque dynamics through the cranial window in age-specific mice with Alzheimer's disease. Plaque number and size increased with age, eventually forming larger aggregates[310]. Z. Huang, Y. Wang, F. Lin, Z. Luo, H. Xu, N. Alifu, J. Li, X. Weng, Y. Sun, J. Song, L. Liu, Y. Chen and J. Qu, Matter, **8**, 102102 (2025); licensed under a Creative Commons Attribution (CC BY) license.

3. Label-free disease diagnosis in vivo

Metabolic imaging technology is rapidly transitioning from laboratory research to clinical applications, emerging as a precise metabolic navigation tool that opens new avenues for diagnosis and treatment. The development of intelligent surgical navigation systems now enables surgeons to accurately delineate tumor boundaries during operations. These translational applications not only enhance diagnostic precision but also redefine the evaluation of treatment outcomes[308]. The capacity to image intrinsic fluorescence lifetimes in living tissues minimizes preparation steps and preserves physiological context. The translation of label-free FLIM from benchtop to *in vivo* settings has created opportunities for real-time functional diagnostics by directly capturing intrinsic lifetime contrasts from NAD(P)H and FAD under physiological conditions[311].

Specifically, accurate identification of glioblastoma's infiltrative edge during neurosurgery remains clinically challenging and contributes to rapid tumor recurrence[308]. FLIM analysis has demonstrated a correlation between tumor cell density and lifetime shortening accompanied by spectral red shifts, establishing its feasibility for intraoperative brain mapping [Fig. 15(d)]. Across neurological, head-and-neck, and gastrointestinal applications, the consistent shift toward shorter NAD(P)H components and altered FAD lifetimes has been associated with malignant infiltration, hypoxia, and aggressive phenotypes. This enables real-time margin assessment and complements conventional intensity-guided fluorescence or white-light visualization in oncology. In transoral robotic surgery for head and neck carcinoma, FLIM of endogenous fluorophores combined with machine learning achieved 95% sensitivity and 89% specificity in detecting occult primary tumors[312]. Similarly, intraoperative FLIM distinguished malignant from normal mucosa through redox lifetime signatures and protein-binding patterns while maintaining compatibility with practical surgical workflows[313]. Beyond oncology, FLIM detected altered NADH lifetimes near amyloid-β (Aβ) plaques in an Alzheimer's disease mouse models, providing a minimally invasive exploration of plaque-induced metabolic dysfunction[314]. In connective-tissue disease, two-photon FLIM of skin capillaries revealed distinct lifetime distributions linked to collagen III, extending multiphoton imaging toward noninvasive skin diagnostics [Fig. 15(e)][309].

Collectively, label-free FLIM *in vivo* reduces sample preparation, preserves physiology, and contributes a quantitative biochemical dimension that complements structural imaging modalities. Key enablers include faster detectors and scanning systems, robust phasor-based analysis to avoid over-fitting, and miniaturized fiber-optic probes/endoscopes with sufficient photon budgets for clinical translation.

4. Probes-based disease diagnosis in vivo

In scenarios requiring specific molecular targeting or microenvironmental parameter resolution *in vivo*, FLIM-compatible targeted probes offer significant quantitative advantages. Molecular beacons with lifetime-sensitive reporters have been employed to quantify protease

activity in tumor microenvironments, while pH- and oxygen-sensitive probes enable high-spatial-resolution mapping of tumor hypoxia[315]. Quantitative FLIM readouts of probe lifetimes facilitate not only disease detection but also therapeutic monitoring, as demonstrated in studies tracking metabolic normalization during chemotherapy or immunotherapy[290].

High-speed FLIM has been used to detect breast cancer in xenograft mouse models. Following subcutaneous injection of sodium fluorescein, its pH-dependent lifetime was measured[316]. Tumor tissue exhibited significantly shorter lifetimes (2.36–3.18 ns) compared to normal tissue (4.15–4.28 ns), reflecting tumor microenvironment acidosis. This clear contrast establishes sodium fluorescein as a pH-sensitive indicator with potential utility for enhancing cancer detection in confocal or endoscopic imaging[316, 317]. In neurodegeneration research, while photobiomodulation (PBM) promotes Aβ plaque clearance in Alzheimer's disease, its early effects remained poorly understood. To address this, a polarity-sensitive FLIM probe with high blood–brain barrier permeability and selective Aβ binding affinity was developed for *in vivo* monitoring [Fig. 15(f)][310]. FLIM revealed progressively longer lifetimes during plaque formation, consistent with reduced environmental polarity. Remarkably, 40 Hz visible light PBM induced polarity reversal within plaques—independent of plaque size and preceding clearance—providing mechanistic insight into PBM's mode of action and suggesting plaque polarity shifts as an early biomarker for treatment efficacy in Alzheimer's disease. Another NIR-emitting specific dye with lifetime contrast enables monitoring Aβ deposits and neurofibrillary tangles through the intact skull of Alzheimer's disease mice *in vivo*[263].

Whether investigating metabolic reprogramming in cancer or energy disturbances in neurodegeneration, these FLIM studies significantly deepen our understanding of disease mechanisms[318]. By enabling spatiotemporal maps of metabolic and microenvironmental dynamics, FLIM supports precision-medicine strategies. Overall, FLIM represents a versatile platform that bridges biochemical contrast with clinical relevance, evolving from static, *in vitro* characterization to dynamic, *in vivo* functional mapping, and from label-free readouts to targeted probes. Integration with miniaturized endoscopes, multimodal modalities like Raman scattering which was demonstrated to detect glucose molecules recently[319] or OCT, and data-driven analysis is expected to further enhance its role in personalized medicine, enabling earlier detection, precise disease grading, and real-time therapy guidance across diverse pathological conditions.

V. CONCLUSION AND OUTLOOK

FLIM has evolved from a specialized physical measurement method into a versatile and essential tool in biomedical imaging. This review has outlined the conceptual foundations of FLIM and highlighted major breakthroughs in instrumentation and algorithms that have substantially improved its practicality and functionality in biomedical research. A prominent trend has been the merging of high-throughput data acquisition with increasingly advanced analytical methods.

Time-domain FLIM, particularly time-correlated single-photon counting (TCSPC), offers exceptional temporal resolution but has traditionally been limited by low frame rates and photon pile-up. Recent detector advances—such as hybrid photomultiplier tubes (PMTs), single-photon avalanche diode (SPAD) arrays, and superconducting nanowire single-photon detectors (SNSPDs)—now facilitate real-time TCSPC performance, even in highly scattering tissues. Concurrent improvements in multifocal excitation, acousto-optic deflectors (AODs), and

compressed sensing have further accelerated data acquisition. Frequency-domain FLIM, empowered by FPGA-based phasor analysis, lowers hardware complexity and enables rapid, fit-free lifetime visualization.

Artificial intelligence (AI) is profoundly reshaping FLIM data analysis and system control. Data-driven models can now derive fluorescence lifetimes directly from raw photon events or phasor coordinates, effectively separating multi-exponential decays and denoising low-signal data. Beyond analysis, AI-driven scanning and adaptive photon routing allow dynamic resource allocation, supporting real-time decision-making in applications such as intraoperative guidance, flow cytometry, and high-content screening.

Integration with complementary imaging modalities represents a key future direction for FLIM. Combining FLIM with Raman spectroscopy, optical coherence tomography (OCT), or photoacoustics provides multidimensional insight into biological systems. Hybrid approaches incorporating hyperspectral imaging or second-harmonic generation have already improved tumor margin identification. Furthermore, the ongoing miniaturization of FLIM into endoscopic and handheld formats extends its potential for non-invasive, point-of-care diagnostics.

Despite substantial progress, several challenges remain. Photon scarcity in deep tissue or rapidly dynamic contexts still limits measurement accuracy, especially for multi-exponential decay processes. The development of brighter, more photostable probes, with larger dynamic range lifetimes would greatly enhance signal quality. There is also a critical need for standardization in calibration practices, detector characteristics, and analysis methods to improve reproducibility and facilitate cross-platform comparisons. Creating unified reference standards, public benchmark datasets, and open-source processing tools will be essential for broader clinical adoption.

As FLIM systems become faster and more compact, their applications are expanding from basic research into translational and clinical settings. In oncology, FLIM is being tested for real-time tumor margin delineation, pathological grading, and therapy response monitoring. In neurology, it shows potential for early detection of neurodegenerative diseases by assessing metabolic shifts or aggregation of amyloid-β plaque. In cardiology, FLIM-based sensors may allow real-time mapping of myocardial redox states, guiding interventions for ischemia or arrhythmias. FLIM also offers novel approaches in immunology—evaluating T-cell activation, phagocytic activity, and microglial behavior—which can inform therapies in autoimmunity, infection, and immuno-oncology.

We envision a future generation of FLIM platforms characterized by four key attributes: speed, specificity, scalability, and intelligence. These systems will combine high-speed photon detection with AI-enhanced interpretation, operating across spatial scales—from subcellular structures to entire organisms—and offering either user-directed or fully autonomous real-time feedback. Importantly, they will be modular and portable, designed for integration into routine clinical practice or field-deployable diagnostics. In this new paradigm, FLIM will transition from a static imaging technology into a dynamic decision-support tool capable of real-time phenotyping, therapy guidance, and precision medicine.

In summary, FLIM provides unparalleled capability for resolving the spatiotemporal dynamics of molecular interactions, metabolic activity, and microenvironmental changes, making it an indispensable tool in both basic and translational science. As advances in optics, electronics, probe chemistry, computing, and machine learning continue to converge, FLIM is positioned to

play a central role in the next generation of bioimaging and diagnostic technologies. By addressing current limitations through sustained interdisciplinary innovation, the FLIM community can unlock deeper understanding of biological mechanisms and accelerate clinical applications.

ACKNOWLEDGMENTS

This work was supported by the Shenzhen Medical Research Fund (Grant No. D2404003), the National Natural Science Foundation of China (Grant Nos. T2421003, 62127819, 62435011, 62305227, and 62305226), and the Shenzhen Science and Technology Program (Grant No. JCYJ20220818100202005).

AUTHOR DECLARATIONS

Conflict of Interest

The authors have no conflicts to disclose.

Author Contributions

Fangrui Lin and Chenshuang Zhang contributed equally to this paper.

DATA AVAILABILITY

The data that support the findings of this study are available from the corresponding author upon reasonable request.

REFERENCES

1. A. Weber, R. Hartig and W. Zuschratter, Methods in Microscopy **2** (1), 73-84 (2025).
2. S. Wang, B. Shen, S. Ren, Y. Zhao, S. Zhang, J. Qu and L. Liu, Journal of Innovative Optical Health Sciences **12** (05), 1930010 (2019).
3. M. Huang, X. Liang, Z. Zhang, J. Wang, Y. Fei, J. Ma, S. Qu and L. Mi, Nanomaterials **10** (4), 604 (2020).
4. J. Sha, W. Liu, X. Zheng, Y. Guo, X. Li, H. Ren, Y. Qin, J. Wu, W. Zhang, C.-S. Lee and P. Wang, Analytical Chemistry **95** (41), 15350-15356 (2023).
5. G. Zou, W. Yu, Y. Xu, Y. Li, R. Hu, J. Qu and L. Liu, RSC Advances **11** (61), 38750-38758 (2021).
6. C. Roffay, J. M. García-Arcos, P. Chapuis, J. López-Andarias, F. Schneider, A. Colom, C. Tomba, I. Di Meglio, K. Barrett, V. Dunsing, S. Matile, A. Roux and V. Mercier, Nature Protocols **19**, 3457–3469 (2024).
7. A. Pliss and P. N. Prasad, Methods and Applications in Fluorescence **8** (3), 032001 (2020).
8. K. Okabe, N. Inada, C. Gota, Y. Harada, T. Funatsu and S. Uchiyama, Nature communications **3** (1), 1-9 (2012).
9. A. Celli, S. Sanchez, M. Behne, T. Hazlett, E. Gratton and T. Mauro, Biophysical journal **98** (5), 911-921 (2010).
10. K. Zheng, T. P. Jensen and D. A. Rusakov, Nature Protocols **13** (3), 581-597 (2018).
11. M. Zhang, M. Wen, Y. Xiong, L. Zhang and C. Tian, Chinese Chemical Letters **29** (10), 1509-1512 (2018).
12. F. Lin, P. Das, Y. Zhao, B. Shen, R. Hu, F. Zhou, L. Liu and J. Qu, Biomedical Optics Express **11** (1), 149-159 (2020).
13. R. Yi, P. Das, F. Lin, B. Shen, Z. Yang, Y. Zhao, L. Hong, Y. He, R. Hu and J. Song, Optics express **27** (9), 12360-12372 (2019).

14. S. Kinoshita, H. Ohta and T. Kushida, Review of Scientific Instruments **52** (4), 572-575 (1981).
15. R. W. Van Resandt, R. Vogel and S. Provencher, Review of Scientific Instruments **53** (9), 1392-1397 (1982).
16. X. F. Wang, T. Uchida and S. Minami, Applied Spectroscopy **43** (5), 840-845 (1989).
17. J. R. Lakowicz, E. Gratton, H. Cherek, B. P. Maliwal and G. Laczko, Journal of Biological Chemistry **259** (17), 10967-10972 (1984).
18. B. Torrado, B. Pannunzio, L. Malacrida and M. A. Digman, Nature Reviews Methods Primers **4** (1), 80 (2024).
19. K. Hiroshi, L. Fan, P. Jongchan, E. Hidenori, N. Kuniyasu, G. Liang and G. Keisuke, Biophotonics Discovery **2** (3), 030901 (2025).
20. J. Park and L. Gao, Current Opinion in Solid State and Materials Science **30**, 101147 (2024).
21. F. Ali and S. Kundu, Chemistry of Materials **37** (11), 3903-3926 (2025).
22. A. Sillen and Y. Engelborghs, Photochemistry and Photobiology **67** (5), 475-486 (1998).
23. D. J. S. Birch and R. E. Imhof, in *Topics in Fluorescence Spectroscopy: Techniques* (Springer US, Boston, MA, 1999), pp. 1-95.
24. L. M. Hirvonen and K. Suhling, Measurement Science and Technology **28** (1), 012003 (2017).
25. W. Becker, *Advanced time-correlated single photon counting applications*. (Springer, 2015).
26. K. Levenberg, Quarterly of Applied Mathematics **2** (2), 164-168 (1944).
27. W. Becker, *The bh TCSPC handbook 10th ed.* (2023).
28. X. F. Wang, T. Uchida, D. M. Coleman and S. Minami, Applied Spectroscopy **45** (3), 360-366 (1991).
29. C. J. De Grauw and H. C. Gerritsen, Applied Spectroscopy **55** (6), 670-678 (2001).
30. R. V. Krishnan, H. Saitoh, H. Terada, V. E. Centonze and B. Herman, Review of Scientific Instruments **74** (5), 2714-2721 (2003).
31. H. Kawaguchi and Y. Ito, IEEE Transactions on Magnetics **48** (2), 411-414 (2012).
32. T. M. Nordlund, in *Topics in Fluorescence Spectroscopy: Techniques*, edited by J. R. Lakowicz (Springer US, Boston, MA, 1999), pp. 183-260.
33. O. J. Steingraber and I. B. Berlman, Review of Scientific Instruments **34** (5), 524-529 (1963).
34. J.-M. I. Maarek, L. Marcu, W. J. Snyder and W. S. Grundfest, Photochemistry and Photobiology **71** (2), 178-187 (2000).
35. G. Enrico, B. Sophie, D. B. S. Jason, R. Qiaoaio and P. B. Nicholas, Journal of Biomedical Optics **8** (3), 381-390 (2003).
36. A. H. Clayton, Q. S. Hanley, D. J. Arndt-Jovin, V. Subramaniam and T. M. Jovin, Biophysical journal **83** (3), 1631-1649 (2002).
37. A. D. Elder, J. H. Frank, J. Swartling, X. Dai and C. F. Kaminski, Journal of Microscopy **224** (2), 166-180 (2006).
38. A. Esposito, T. Oggier, H. C. Gerritsen, F. Lustenberger and F. S. Wouters, Optics Express **13** (24), 9812-9821 (2005).
39. Z. Qiaole, S. Ben, S. Raymond, O. Rein van den, L. Rene, K. Harry van, M. P. Inge, P. Frank, T. B. Jan, R. Marcel, J. Kees, J. Jan Geert Sander de, G. Bert van, S. Karel and T. Y. Ian, Journal of Biomedical Optics **17** (12), 126020 (2012).
40. M. A. Digman, V. R. Caiolfa, M. Zamai and E. Gratton, Biophysical journal **94** (2), L14-L16 (2008).
41. G. I. Redford and R. M. Clegg, Journal of fluorescence **15** (5), 805-815 (2005).
42. A. Clayton, Q. Hanley and P. Verveer, Journal of microscopy **213** (1), 1-5 (2004).

43. D. Reichert, M. T. Erkkilä, G. Holst, N. Hecker-Denschlag, M. Wilzbach, C. Hauger, W. Drexler, J. Gesperger, B. Kiesel, T. Roetzer, A. Unterhuber, G. Widhalm, R. A. Leitgeb and M. Andreana, Biomedical Optics Express **11** (3), 1598-1616 (2020).
44. M. T. Erkkilä, B. Bauer, N. Hecker-Denschlag, M. J. Madera Medina, R. A. Leitgeb, A. Unterhuber, J. Gesperger, T. Roetzer, C. Hauger, W. Drexler, G. Widhalm and M. Andreana, Journal of Biophotonics **12** (6), e201800378 (2019).
45. M. Raspe, K. M. Kedziora, B. van den Broek, Q. Zhao, S. de Jong, J. Herz, M. Mastop, J. Goedhart, T. W. J. Gadella, I. T. Young and K. Jalink, Nature Methods **13** (6), 501-504 (2016).
46. Y. Zhang, I. H. Guldner, E. L. Nichols, D. Benirschke, C. J. Smith, S. Zhang and S. S. Howard, Optica **8** (6), 885-897 (2021).
47. Y. Zhang, A. A. Khan, G. D. Vigil and S. S. Howard, Journal of the Optical Society of America A **33** (7), B1-B11 (2016).
48. L. M. Hirvonen and K. Suhling, Frontiers in Physics **8**, 161 (2020).
49. W. Becker, B. Su, O. Holub and K. weisshart, Microscopy Research and Technique **74** (9), 804-811 (2011).
50. A. L. Trinh, S. Ber, A. Howitt, P. O. Valls, M. W. Fries, A. R. Venkitaraman and A. Esposito, Methods and Applications in Fluorescence **7** (4), 044001 (2019).
51. M. Koenig, S. Orthaus-Mueller, R. Dowler, B. Kraemer, A. Tannert, O. Schulz, T. Roehlicke, M. Wahl, H.-J. Rahn and M. Patting, Biophysical Journal **112** (3), 298a (2017).
52. M. Wahl, T. Röhlicke, S. Kulisch, S. Rohilla, B. Krämer and A. C. Hocke, Review of Scientific Instruments **91** (1), 013108 (2020).
53. B. Wolfgang, B. Axel and S. Stefan, presented at the Proc.SPIE, 2019 (unpublished).
54. M. Castello, G. Tortarolo, M. Buttafava, T. Deguchi, F. Villa, S. Koho, L. Pesce, M. Oneto, S. Pelicci, L. Lanzanó, P. Bianchini, C. J. R. Sheppard, A. Diaspro, A. Tosi and G. Vicidomini, Nature Methods **16** (2), 175-178 (2019).
55. S. Liu, Z. Zhang, J. Zheng, L. Xu, C. Kuang and X. Liu, Optics Communications **421**, 83-89 (2018).
56. W. Dong, Y. Huang, W. Tao, L. Xu, Y. Han, X. Hao, C. Kuang and X. Liu, Optics and Lasers in Engineering **184**, 108547 (2025).
57. Q. Pian, R. Yao, N. Sinsuebphon and X. Intes, Nature photonics **11** (7), 411-414 (2017).
58. F. Guo, F. Lin, B. Shen, S. Wang, Y. Li, J. Guo, Y. Chen, Y. Liu, Y. Lu, R. Hu, J. He, C. Liao, Y. Wang, J. Qu and L. Liu, Nanophotonics **13** (2), 217-227 (2024).
59. A. Batista, H. G. Breunig, C. Donitzky and K. König, in *Multiphoton Microscopy and Fluorescence Lifetime Imaging* (De Gruyter, 2018), pp. 301-320.
60. T. Wu, J. Liao, F. Xiang, J. Yu, Y. Gao, L. Liu, S. Ye, H. Li, K. Shi and W. Zheng, Biomedical Optics Express **14** (7), 3380-3396 (2023).
61. T. Wu, W. Geng, Y. Zhang, Q. Xia, M. Zhang, J. Li, M. Chen, W. Xi, S. Peng, Z. Feng and J. Qian, Progress In Electromagnetics Research **180**, 115-126 (2024).
62. A. Tamimi, M. Caldarola, S. Hambura, J. C. Boffi, N. Noordzij, J. W. N. Los, A. Guardiani, H. Kooiman, L. Wang, C. Kieser, F. Braun, M. A. U. Castaneda, A. Fognini and R. Prevedel, ACS Photonics **11** (10), 3960-3971 (2024).
63. F. Wang, F. Ren, Z. Ma, L. Qu, R. Gourgues, C. Xu, A. Baghdasaryan, J. Li, I. E. Zadeh, J. W. Los, A. Fognini, J. Qin-Dregely and H. Dai, Nature Nanotechnology **17**, 653-660 (2022).
64. I. Holzman and Y. Ivry, Advanced Quantum Technologies **2** (3-4), 1800058 (2019).

65. Z. Feng, T. Tang, T. Wu, X. Yu, Y. Zhang, M. Wang, J. Zheng, Y. Ying, S. Chen, J. Zhou, X. Fan, D. Zhang, S. Li, M. Zhang and J. Qian, Light: Science & Applications **10** (1), 197 (2021).
66. S. Golovynskyi, I. Golovynska, L. I. Stepanova, O. I. Datsenko, L. Liu, J. Qu and T. Y. Ohulchanskyy, Journal of biophotonics **11** (12), e201800141 (2018).
67. J. Yu, R. Zhang, Y. Gao, Z. Sheng, M. Gu, Q. Sun, J. Liao, T. Wu, Z. Lin and P. Wu, Optics Letters **45** (12), 3305-3308 (2020).
68. B. Korzh, Q.-Y. Zhao, J. P. Allmaras, S. Frasca, T. M. Autry, E. A. Bersin, A. D. Beyer, R. M. Briggs, B. Bumble, M. Colangelo, G. M. Crouch, A. E. Dane, T. Gerrits, A. E. Lita, F. Marsili, G. Moody, C. Peña, E. Ramirez, J. D. Rezac, N. Sinclair, M. J. Stevens, A. E. Velasco, V. B. Verma, E. E. Wollman, S. Xie, D. Zhu, P. D. Hale, M. Spiropulu, K. L. Silverman, R. P. Mirin, S. W. Nam, A. G. Kozorezov, M. D. Shaw and K. K. Berggren, Nature Photonics **14** (4), 250-255 (2020).
69. B. G. Oripov, D. S. Rampini, J. Allmaras, M. D. Shaw, S. W. Nam, B. Korzh and A. N. McCaughan, Nature **622** (7984), 730-734 (2023).
70. B. Wolfgang and S. Vladislav, presented at the Proc.SPIE, 2013 (unpublished).
71. V. Buschmann, E. Ermilov, F. Koberling, M. Loidolt-Krüger, J. Breitlow, H. Kooiman, J. W. N. Los, J. van Willigen, M. Caldarola, A. Fognini, M. U. Castaneda, J. de Wild, B. Vermang, G. Brammertz and R. Erdmann, Review of Scientific Instruments **94** (3), 033703 (2023).
72. S. Farina, A. Ghezzi, I. Labanca, G. Acconcia, C. D'Andrea, A. Farina and I. Rech, Optics Express **33** (11), 22296-22307 (2025).
73. J. A. Richardson, E. A. G. Webster, L. A. Grant and R. K. Henderson, IEEE Transactions on Electron Devices **58** (7), 2028-2035 (2011).
74. M. Wayne, A. Ulku, A. Ardelean, P. Mos, C. Bruschini and E. Charbon, IEEE Transactions on Electron Devices **69** (6), 2865-2872 (2022).
75. A. C. Ulku, C. Bruschini, I. M. Antolović, Y. Kuo, R. Ankri, S. Weiss, X. Michalet and E. Charbon, IEEE Journal of Selected Topics in Quantum Electronics **25** (1), 1-12 (2019).
76. A. T. Erdogan, R. Walker, N. Finlayson, N. Krstajić, G. Williams, J. Girkin and R. Henderson, IEEE Journal of Solid-State Circuits **54** (6), 1705-1719 (2019).
77. J. Richardson, R. Walker, L. Grant, D. Stoppa, F. Borghetti, E. Charbon, M. Gersbach and R. K. Henderson, presented at the 2009 IEEE Custom Integrated Circuits Conference, 2009 (unpublished).
78. D. Bronzi, F. Villa, S. Tisa, A. Tosi and F. Zappa, IEEE Sensors Journal **16** (1), 3-12 (2016).
79. J. M. Pavia, M. Wolf and E. Charbon, Optics Express **22** (4), 4202-4213 (2014).
80. S. Burri, Y. Maruyama, X. Michalet, F. Regazzoni, C. Bruschini and E. Charbon, Optics Express **22** (14), 17573-17589 (2014).
81. I. Gyongy, A. Davies, B. Gallinet, N. A. W. Dutton, R. R. Duncan, C. Rickman, R. K. Henderson and P. A. Dalgarno, Optics Express **26** (3), 2280-2291 (2018).
82. C. Bruschini, H. Homulle, I. M. Antolovic, S. Burri and E. Charbon, Light: Science & Applications **8** (1), 87 (2019).
83. N. Krstajić, J. Levitt, S. Poland, S. Ameer-Beg and R. Henderson, Optics Express **23** (5), 5653-5669 (2015).
84. T. Milanese, C. Bruschini, S. Burri, E. Bernasconi, A. C. Ulku and E. Charbon, Optics Express **31** (26), 44295-44314 (2023).
85. G. O. S. Williams, E. Williams, N. Finlayson, A. T. Erdogan, Q. Wang, S. Fernandes, A. R. Akram, K. Dhaliwal, R. K. Henderson, J. M. Girkin and M. Bradley, Nature Communications **12** (1), 6616 (2021).

86. W. Becker, L. M. Hirvonen, J. Milnes, T. Conneely, O. Jagutzki, H. Netz, S. Smietana and K. Suhling, Review of Scientific Instruments **87** (9), 093710 (2016).
87. N. Oleksiievets, J. C. Thiele, A. Weber, I. Gregor, O. Nevskyi, S. Isbaner, R. Tsukanov and J. Enderlein, The Journal of Physical Chemistry A **124** (17), 3494-3500 (2020).
88. L. M. Hirvonen, W. Becker, J. Milnes, T. Conneely, S. Smietana, A. Le Marois, O. Jagutzki and K. Suhling, Applied Physics Letters **109** (7), 071101 (2016).
89. J. Nedbal, F. Mattioli Della Rocca, I. T. Ivanova, A. Allan, J. Graham, R. Walker, R. K. Henderson and K. Suhling, Scientific Reports **14** (1), 7247 (2024).
90. Liisa, Hirvonen, Frederic, Festy, Klaus and Suhling, Optics Letters **39** (19), 5602-5605 (2014).
91. M. Wang, L. Zhou, J. Hu, H. Cao, D. Lin, B. Yu and J. Qu, Optics Letters **48** (5), 1144-1147 (2023).
92. L. M. Hirvonen, J. Nedbal, N. Almutairi, T. A. Phillips, W. Becker, T. Conneely, J. Milnes, S. Cox, S. Stürzenbaum and K. Suhling, Journal of Biophotonics **13** (2), e201960099 (2020).
93. S. Kayvan, E. D. Danielle, L. Wei, W. Kurt, L. Joe, H. Jan, M. Veronika, H. Anna, V. C. Jenu, V. Andreas, D. R. Jeremy, W. E. Kevin and C. S. Melissa, Journal of Biomedical Optics **28** (6), 066502 (2023).
94. C. Xu, M. Nedergaard, D. J. Fowell, P. Friedl and N. Ji, Cell **187** (17), 4458-4487 (2024).
95. K. M. N. S. Nadella, H. Roš, C. Baragli, V. A. Griffiths, G. Konstantinou, T. Koimtzis, G. J. Evans, P. A. Kirkby and R. A. Silver, Nature Methods **13** (12), 1001-1004 (2016).
96. D. Lin, D. Chen, Z. Dong, L. Zhou, M. Nie, J. Qu and B. Yu, Optics Letters **49** (21), 6193-6196 (2024).
97. A. Li, *Double-Prism Multi-mode Scanning: Principles and Technology*. (Springer Singapore, Singapore, 2018).
98. N. Kirkpatrick, E. Chung, D. Cook, X. Han, G. Gruionu, S. Liao, L. Munn, T. Padera, D. Fukumura and R. K. Jain, IntraVital **1** (1), 60-68 (2012).
99. Y. Wei, P. Xiao, Q. Jing, G. Jian, F. Shunping, W. Qi, Q. Junle and N. Hanben, Journal of Biomedical Optics **19** (11), 116004 (2014).
100. J. Qi, Y. Shao, L. Liu, K. Wang, T. Chen, J. Qu and H. Niu, Optics Letters **38** (10), 1697-1699 (2013).
101. W. Qianqian, Q. Jing, L. Danying, Y. Wei, H. Rui, P. Xiao and Q. Junle, presented at the Proc.SPIE, 2017 (unpublished).
102. P. Chen, Q. Kang, J. Niu, Y. Jing, X. Zhang, B. Yu, J. Qu and D. Lin, Biomedical Optics Express **14** (4), 1718-1731 (2023).
103.P. Ricci, G. Sancataldo, V. Gavryusev, F. S. Pavone, P. Saggau and M. Duocastella, Journal of Physics: Photonics **6** (2), 022001 (2024).
104. R. Jiang, Z. Zhou, X. Lv and S. Zeng, Review of Scientific Instruments **83** (4), 043709 (2012).
105. T. Nielsen, M. Fricke, D. Hellweg and P. Andresen, Journal of Microscopy **201** (3), 368-376 (2001).
106. S. A. Suresh, S. Vyas, C. H. Chu, T. Yamaguchi, T. Tanaka, J. A. Yeh, D. P. Tsai and Y. Luo, Laser & Photonics Reviews **19** (6), 2401314 (2025).
107. Y. Yang, C. Liu, B. Dong and C. Xue, Optics Express **33** (14), 29270-29280 (2025).
108. C. Zhang, B. Yu, F. Lin, S. Samanta, H. Yu, W. Zhang, Y. Jing, C. Shang, D. Lin, K. Si, W. Gong and J. Qu, PhotoniX **4** (1), 38 (2023).
109. S. Li, J. Wu, H. Li, D. Lin, B. Yu and J. Qu, Optics Express **26** (18), 23585-23593 (2018).
110. J. L. Rinnenthal, C. Börnchen, H. Radbruch, V. Andresen, A. Mossakowski, V. Siffrin, T. Seelemann, H. Spiecker, I. Moll, J. Herz, A. E. Hauser, F. Zipp, M. J. Behne and R. Niesner, PLOS ONE **8** (4), e60100 (2013).

111. S. Kumar, C. Dunsby, P. A. A. D. Beule, D. M. Owen, U. Anand, P. M. P. Lanigan, R. K. P. Benninger, D. M. Davis, M. A. A. Neil, P. Anand, C. Benham, A. Naylor and P. M. W. French, Optics Express **15** (20), 12548-12561 (2007).

112. S. P. Poland, N. Krstajić, S. Coelho, D. Tyndall, R. J. Walker, V. Devauges, P. E. Morton, N. S. Nicholas, J. Richardson, D. D.-U. Li, K. Suhling, C. M. Wells, M. Parsons, R. K. Henderson and S. M. Ameer-Beg, Optics Letters **39** (20), 6013-6016 (2014).

113. S. P. Poland, N. Krstajić, J. Monypenny, S. Coelho, D. Tyndall, R. J. Walker, V. Devauges, J. Richardson, N. Dutton, P. Barber, D. D.-U. Li, K. Suhling, T. Ng, R. K. Henderson and S. M. Ameer-Beg, Biomedical Optics Express **6** (2), 277-296 (2015).

114. S. P. Poland, A. T. Erdogan, N. Krstajić, J. Levitt, V. Devauges, R. J. Walker, D. D.-U. Li, S. M. Ameer-Beg and R. K. Henderson, Optics Express **24** (7), 6899-6915 (2016).

115. J. A. Levitt, S. P. Poland, N. Krstajic, K. Pfisterer, A. Erdogan, P. R. Barber, M. Parsons, R. K. Henderson and S. M. Ameer-Beg, Scientific Reports **10** (1), 5146 (2020).

116. H. Mai, A. Jarman, A. T. Erdogan, C. Treacy, N. Finlayson, R. K. Henderson and S. P. Poland, Optics Letters **48** (8), 2042-2045 (2023).

117. S. P. Poland, N. Krstajić, R. D. Knight, R. K. Henderson and S. M. Ameer-Beg, Optics Letters **39** (8), 2431-2434 (2014).

118. S. P. Poland, G. K. Chan, J. A. Levitt, N. Krstajić, A. T. Erdogan, R. K. Henderson, M. Parsons and S. M. Ameer-Beg, Optics Letters **43** (24), 6057-6060 (2018).

119. N. Krstajić, S. Poland, J. Levitt, R. Walker, A. Erdogan, S. Ameer-Beg and R. K. Henderson, Optics Letters **40** (18), 4305-4308 (2015).

120. D. R. Matthews, G. O. Fruhwirth, G. Weitsman, L. M. Carlin, E. Ofo, M. Keppler, P. R. Barber, I. D. C. Tullis, B. Vojnovic, T. Ng and S. M. Ameer-Beg, PLOS ONE **7** (4), e33231 (2012).

121. L. Marcu, Annals of biomedical engineering **40**, 304-331 (2012).

122. J. Nedbal, V. Visitkul, E. Ortiz-Zapater, G. Weitsman, P. Chana, D. R. Matthews, T. Ng and S. M. Ameer-Beg, Cytometry Part A **87** (2), 104-118 (2015).

123. L. Day-Uei, R. R. Bruce, A. Robin, A. Jochen and K. H. Robert, Journal of Biomedical Optics **15** (1), 017006 (2010).

124. D. D.-U. Li, H. Yu and Y. Chen, Optics Letters **40** (3), 336-339 (2015).

125. W. Nevens, T. Lapauw, J. Vrijsen, T. V. d. Dries, H. Ingelberts and M. Kuijk, IEEE Sensors Letters **9** (8), 1-4 (2025).

126. L. Yahui, L. Lixin, X. Dong, L. Hang, S. Natakorn, T. Jinshou, C. Yu and L. David Day-Uei, in *Fluorescence Imaging - Recent Advances and Applications*, edited by P. Dr. Raffaello (IntechOpen, Rijeka, 2022), pp. Ch. 3.

127. R. Datta, T. M. Heaster, J. T. Sharick, A. A. Gillette and M. C. Skala, Journal of biomedical optics **25** (7), 071203 (2020).

128. Y. Li, N. Sapermsap, J. Yu, J. Tian, Y. Chen and D. Day-Uei Li, Biomedical Optics Express **12** (7), 4293-4307 (2021).

129. S. Wang, J. V. Chacko, A. K. Sagar, K. W. Eliceiri and M. Yuan, Biomedical Optics Express **10** (11), 5497-5517 (2019).

130. X. Li, Y. Huang, Y. Guo, H. Guo, M. Pu, R. Zhang, Q. Zhang, F. Zhang, M. Xu, N. Chi and X. Luo, Laser & Photonics Reviews **19** (15), 2401837 (2025).

131. M.-J. Sun, Y.-C. Zhang, F.-R. Lin, S. Wang, L.-W. Liu and J.-L. Qu, APL Photonics **9** (1), 016108 (2024).

132. S. F. Silva, J. P. Domingues and A. M. Morgado, PLOS ONE **14** (5), e0216894 (2019).
133. G. Wu, T. Nowotny, Y. Zhang, H.-Q. Yu and D. D.-U. Li, Optics Letters **41** (11), 2561-2564 (2016).
134. R. Yao, M. Ochoa, P. Yan and X. Intes, Light: Science & Applications **8** (1), 26 (2019).
135. J. T. Smith, R. Yao, N. Sinsuebphon, A. Rudkouskaya, N. Un, J. Mazurkiewicz, M. Barroso, P. Yan and X. Intes, Proceedings of the National Academy of Sciences **116** (48), 24019-24030 (2019).
136. D. Xiao, Y. Chen and D. D. U. Li, IEEE Journal of Selected Topics in Quantum Electronics **27** (4), 1-10 (2021).
137. D. Xiao, Z. Zang, W. Xie, N. Sapermsap, Y. Chen and D. D. Uei Li, Optics Express **30** (7), 11479-11494 (2022).
138. Y.-I. Chen, Y.-J. Chang, S.-C. Liao, T. D. Nguyen, J. Yang, Y.-A. Kuo, S. Hong, Y.-L. Liu, H. G. Rylander III and S. R. Santacruz, Communications Biology **5** (1), 18 (2022).
139. D. Xiao, N. Sapermsap, Y. Chen and D. D. U. Li, Optica **10** (7), 944-951 (2023).
140. B. Shen, Y. Lu, F. Guo, F. Lin, R. Hu, F. Rao, J. Qu and L. Liu, Communications Biology **7** (1), 1359 (2024).
141. A. J. Bowman, C. Huang, M. J. Schnitzer and M. A. Kasevich, Science **380** (6651), 1270-1275 (2023).
142. A. J. Bowman, B. B. Klopfer, T. Juffmann and M. A. Kasevich, Nature Communications **10** (1), 4561 (2019).
143. V. Kapitany, V. Zickus, A. Fatima, G. Carles and D. Faccio, Proceedings of the National Academy of Sciences **120** (16), e2214617120 (2023).
144. M. Popleteeva, K. T. Haas, D. Stoppa, L. Pancheri, L. Gasparini, C. F. Kaminski, L. D. Cassidy, A. R. Venkitaraman and A. Esposito, Optics Express **23** (18), 23511-23525 (2015).
145. D. M. Grant, J. McGinty, E. J. McGhee, T. D. Bunney, D. M. Owen, C. B. Talbot, W. Zhang, S. Kumar, I. Munro, P. M. P. Lanigan, G. T. Kennedy, C. Dunsby, A. I. Magee, P. Courtney, M. Katan, M. A. A. Neil and P. M. W. French, Optics Express **15** (24), 15656-15673 (2007).
146. A. Margineanu, J. J. Chan, D. J. Kelly, S. C. Warren, D. Flatters, S. Kumar, M. Katan, C. W. Dunsby and P. M. French, Scientific reports **6** (1), 1-17 (2016).
147. S. F. Silva, J. P. Domingues and A. M. Morgado, Journal of Healthcare Engineering **2018** (1), 1371386 (2018).
148. M. J. Cole, J. Siegel, S. E. D. Webb, R. Jones, K. Dowling, P. M. W. French, M. J. Lever, L. O. D. Sucharov, M. A. A. Neil, R. Juškaitis and T. Wilson, Optics Letters **25** (18), 1361-1363 (2000).
149. P. Weber, S. Schickinger, M. Wagner, B. Angres, T. Bruns and H. Schneckenburger, in *International Journal of Molecular Sciences* (2015), Vol. 16, pp. 5375-5385.
150. M. Paul, A. W. Michael, A. Andrei, C. U. Arin, C. Edoardo and B. Claudio, presented at the Proc.SPIE, 2024 (unpublished).
151. L. Thomas, I. Hans, D. Thomas Van den and K. Maarten, presented at the Proc.SPIE, 2019 (unpublished).
152. B. J. Little, Review of Scientific Instruments **89** (10), 10E117 (2018).
153. A. V. Agronskaia, L. Tertoolen and H. C. Gerritsen, Journal of Physics D: Applied Physics **36** (14), 1655 (2003).
154. D. S. Elson, I. Munro, J. Requejo-Isidro, J. McGinty, C. Dunsby, N. Galletly, G. W. Stamp, M. A. A. Neil, M. J. Lever, P. A. Kellett, A. Dymoke-Bradshaw, J. Hares and P. M. W. French, New Journal of Physics **6** (1), 180 (2004).

155. S. Lévêque-Fort, M. P. Fontaine-Aupart, G. Roger and P. Georges, Optics Letters **29** (24), 2884-2886 (2004).
156. S. F. Silva, A. Batista, O. C. Castejón, M. J. Quadrado, J. P. Domingues and M. Morgado, presented at the Clinical and Biomedical Spectroscopy and Imaging IV, Munich, 2015 (unpublished).
157. R. Li, A. Liu, T. Wu, W. Xiao, L. I. Tang and L. Chen, Journal of Microscopy **279** (1), 69-76 (2020).
158. X. Feng, Y. Ma and L. Gao, Nature Communications **13** (1), 3333 (2022).
159. Q. Cui, J. Park, Y. Ma and L. Gao, Optica **8** (12), 1552-1558 (2021).
160.Y. Ma, J. Park, L. Huang, C. Sen, S. Burri, C. Bruschini, X. Yang, Q. Cui, R. B. Cameron, G. A. Fishbein, B. N. Gomperts, A. Ozcan, E. Charbon and L. Gao, Proceedings of the National Academy of Sciences **121** (40), e2402556121 (2024).
161. A. Ghezzi, A. Farina, A. Bassi, G. Valentini, I. Labanca, G. Acconcia, I. Rech and C. D'Andrea, Optics Letters **46** (6), 1353-1356 (2021).
162. J. L. Lagarto, F. Villa, S. Tisa, F. Zappa, V. Shcheslavskiy, F. S. Pavone and R. Cicchi, Scientific Reports **10** (1), 8116 (2020).
163. Y. Yang, Y. Gou, P. Feng, Y. Xu, B. Wang, B. Liu, J. Tian, X. Wang and H. Liu, Nuclear Instruments and Methods in Physics Research Section A: Accelerators, Spectrometers, Detectors and Associated Equipment **1070**, 170023 (2025).
164. A. T. Erdogan, R. Walker, N. Finlayson, N. Krstajic, G. O. S. Williams and R. K. Henderson, presented at the 2017 Symposium on VLSI Circuits, 2017 (unpublished).
165. K. Morimoto, A. Ardelean, M.-L. Wu, A. C. Ulku, I. M. Antolovic, C. Bruschini and E. Charbon, Optica **7** (4), 346-354 (2020).
166. N. Ronceray, S. Bennani, M. F. Mitsioni, N. Siegel, M. J. Marcaida, C. Bruschini, E. Charbon, R. Roy, M. Dal Peraro, G. P. Acuna and A. Radenovic, Light: Science & Applications **14** (1), 258 (2025).
167. J. T. Smith, A. Rudkouskaya, S. Gao, J. M. Gupta, A. Ulku, C. Bruschini, E. Charbon, S. Weiss, M. Barroso, X. Intes and X. Michalet, Optica **9** (5), 532-544 (2022).
168. A. B. Matheson, A. T. Erdogan, C. Hopkinson, S. Borrowman, G. J. Loake, M. G. Tanner and R. K. Henderson, Optics Express **31** (14), 22766-22775 (2023).
169. D. Angelone, N. Nudds, A. B. Matheson, A. T. Erdogan, W. Messina, R. Burke, R. K. Henderson, S. Andersson-Engels and S. K. Venkata Sekar, Optics Letters **50** (13), 4230-4233 (2025).
170. B. Saleh and M. Teich, *Fundamentals of Photonics*, Third ed. (Wiley, 2019).
171. A. J. Bowman and M. A. Kasevich, ACS Nano **15** (10), 16043-16054 (2021).
172. J. Qu, L. Liu, D. Chen, Z. Lin, G. Xu, B. Guo and H. Niu, Optics Letters **31** (3), 368-370 (2006).
173. L. Liu, J. Qu, Z. Lin, L. Wang, Z. Fu, B. Guo and H. Niu, Applied Physics B **84** (3), 379-383 (2006).
174. L. Lixin, L. Yahui, S. Luogeng, L. Heng, P. Xiao and Q. Junle, presented at the Proc.SPIE, 2014 (unpublished).
175. Y. Ma, Y. Lee, C. Best-Popescu and L. Gao, Proceedings of the National Academy of Sciences **118** (3), e2004176118 (2021).
176. H. Li, Y. Xue, J. Tian, S. Li, J. Wang, P. Chen, L. Tian, J. He, M. Zhang, B. Liu, Y. Gou, X. Xu, Y. Li and L. Xin, Review of Scientific Instruments **93** (11), 113303 (2022).
177. D. Chen, H. Li, B. Yu and J. Qu, Nanophotonics **11** (8), 1537-1547 (2022).
178. G. Grover, S. Quirin, C. Fiedler and R. Piestun, Biomedical Optics Express **2** (11), 3010-3020 (2011).
179. M. Eibl, S. Karpf, D. Weng, H. Hakert, T. Pfeiffer, J. P. Kolb and R. Huber, Biomedical Optics Express **8** (7), 3132-3142 (2017).

180. J.-M. I. Maarek, L. Marcu, M. C. Fishbein and W. S. Grundfest, Lasers in Surgery and Medicine **27** (3), 241-254 (2000).
181. A. Alfonso‐Garcia, J. Bec, B. Weyers, M. Marsden, X. Zhou, C. Li and L. Marcu, Journal of Biophotonics **14** (6), e202000472 (2021).
182. A. Alfonso‐Garcia, J. Bec, S. Sridharan Weaver, B. Hartl, J. Unger, M. Bobinski, M. Lechpammer, F. Girgis, J. Boggan and L. Marcu, Journal of biophotonics **13** (1), e201900108 (2020).
183. D. R. Yankelevich, D. Ma, J. Liu, Y. Sun, Y. Sun, J. Bec, D. S. Elson and L. Marcu, Review of Scientific Instruments **85** (3), 034303 (2014).
184. J. Liu, Y. Sun, J. Qi and L. Marcu, Physics in Medicine & Biology **57** (4), 843 (2012).
185. J. R. Lakowicz, *Principles of fluorescence spectroscopy*. (Springer, 2006).
186. M. Marsden, T. Fukazawa, Y. C. Deng, B. Weyers and L. Marcu, Biomedical optics express **11** (9), 5166-5180 (2020).
187. J. L. Lagarto, J. E. Phipps, L. Faller, D. Ma, J. Unger, J. Bec, S. Griffey, J. Sorger, D. G. Farwell and L. Marcu, Journal of Photochemistry and Photobiology B: Biology **185**, 90-99 (2018).
188. D. Gorpas, J. Phipps, J. Bec, D. Ma, S. Dochow, D. Yankelevich, J. Sorger, J. Popp, A. Bewley, R. Gandour-Edwards, L. Marcu and D. G. Farwell, Scientific Reports **9** (1), 1187 (2019).
189. M. Marsden, B. W. Weyers, J. Bec, T. Sun, R. F. Gandour-Edwards, A. C. Birkeland, M. Abouyared, A. F. Bewley, D. G. Farwell and L. Marcu, IEEE Transactions on Biomedical Engineering **68** (3), 857-868 (2021).
190. B. E. Sherlock, J. E. Phipps, J. Bec and L. Marcu, Optics Letters **42** (19), 3753-3756 (2017).
191. P. Pande, S. Shrestha, J. Park, I. Gimenez-Conti, J. Brandon, B. E. Applegate and J. A. Jo, Biomedical Optics Express **7** (5), 2000-2015 (2016).
192. J. Bec, X. Zhou, M. Villiger, J. A. Southard, B. Bouma and L. Marcu, Biomedical Optics Express **15** (4), 2114-2132 (2024).
193. J. Bec, J. E. Phipps, D. Gorpas, D. Ma, H. Fatakdawala, K. B. Margulies, J. A. Southard and L. Marcu, Scientific Reports **7** (1), 8960 (2017).
194. H. Fatakdawala, S. Poti, F. Zhou, Y. Sun, J. Bec, J. Liu, D. R. Yankelevich, S. P. Tinling, R. F. Gandour-Edwards, D. G. Farwell and L. Marcu, Biomedical Optics Express **4** (9), 1724-1741 (2013).
195. T. A. Shaik, A. Alfonso-García, X. Zhou, K. M. Arnold, A. K. Haudenschild, C. Krafft, L. G. Griffiths, J. Popp and L. Marcu, Analytical Chemistry **92** (15), 10659-10667 (2020).
196. J. Bec, T. A. Shaik, C. Krafft, T. W. Bocklitz, A. Alfonso-Garcia, K. B. Margulies, J. Popp and L. Marcu, Frontiers in Cardiovascular Medicine **7**, 122 (2020).
197. X. Liu, J. Bec, X. Zhou, A. A. Garcia and L. Marcu, Optics Letters **50** (3), 900-903 (2025).
198. X. Zhou, J. Bec, D. Yankelevich and L. Marcu, Optics Express **29** (13), 20105-20120 (2021).
199. X. Zhou, J. Bec, K. Ehrlich, A. A. Garcia and L. Marcu, Optics Letters **48** (17), 4578-4581 (2023).
200. S. Moon, Y. Won and D. Y. Kim, Optics Express **17** (4), 2834-2849 (2009).
201. Y. Won, S. Moon, W. Yang, D. Kim, W.-T. Han and D. Y. Kim, Optics Express **19** (4), 3396-3405 (2011).
202. J. Kim, J. Ryu and D. Gweon, Applied Microscopy **46** (1), 6-13 (2016).
203. J. Ryu, U. Kang, J. Kim, H. Kim, J. H. Kang, H. Kim, D. K. Sohn, J.-h. Jeong, H. Yoo and B. Gweon, Biomedical Optics Express **9** (7), 3449-3463 (2018).
204. J. Han, S. Kim, H. Jung Kim, H. Soo Nam, M. W. Lee, J. W. Song, J. W. Kim and H. Yoo, Arteriosclerosis, Thrombosis, and Vascular Biology **43** (7), 1295-1307 (2023).

205. H. S. Nam, W. J. Kang, M. W. Lee, J. W. Song, J. W. Kim, W.-Y. Oh and H. Yoo, Biomedical Optics Express **9** (4), 1930-1947 (2018).
206. W. Hwang, D. Kim, S. Lee, Y. J. Won, S. Moon and D. Y. Kim, Optics Communications **443**, 136-143 (2019).
207. X. Y. Dow, S. Z. Sullivan, R. D. Muir and G. J. Simpson, Optics Letters **40** (14), 3296-3299 (2015).
208. R. D. Muir, D. J. Kissick and G. J. Simpson, Optics Express **20** (9), 10406-10415 (2012).
209. A. J. Bower, J. E. Sorrells, J. Li, M. Marjanovic, R. Barkalifa and S. A. Boppart, Biomedical Optics Express **10** (12), 6408-6421 (2019).
210. A. J. Bower, J. Li, E. J. Chaney, M. Marjanovic, D. R. Spillman and S. A. Boppart, Optica **5** (10), 1290-1296 (2018).
211. F. Di Giacinto, C. Serantoni, M. De Spirito and G. Maulucci, Microscopy and Microanalysis **31** (2), ozaf014 (2025).
212. J. E. Sorrells, R. R. Iyer, L. Yang, A. J. Bower, D. R. Spillman, E. J. Chaney, H. Tu and S. A. Boppart, Biomedical optics express **12** (7), 4003-4019 (2021).
213. J. E. Sorrells, R. R. Iyer, L. Yang, E. J. Chaney, M. Marjanovic, H. Tu and S. A. Boppart, Optics Express **29** (23), 37759-37775 (2021).
214. J. E. Sorrells, R. R. Iyer, L. Yang, E. M. Martin, G. Wang, H. Tu, M. Marjanovic and S. A. Boppart, ACS Photonics **9** (8), 2748-2755 (2022).
215. R. R. Iyer, J. E. Sorrells, L. Yang, E. J. Chaney, D. R. Spillman, B. E. Tibble, C. A. Renteria, H. Tu, M. Žurauskas, M. Marjanovic and S. A. Boppart, Scientific Reports **12** (1), 3438 (2022).
216. R. R. Iyer, J. E. Sorrells, K. K. D. Tan, L. Yang, G. Wang, H. Tu and S. A. Boppart, Biomedical Optics Express **15** (4), 2048-2062 (2024).
217. D. Su, X. Li, W. Gao, Q. Wei, H. Li, C. Guo and W. Zhao, Opto-Electronic Science **2** (12), 230018 (2023).
218. M. A. Condrau, R. A. Schwendener, P. Niederer and M. Anliker, Cytometry **16** (3), 187-194 (1994).
219. S. Karpf, C. T. Riche, D. Di Carlo, A. Goel, W. A. Zeiger, A. Suresh, C. Portera-Cailliau and B. Jalali, Nature Communications **11** (1), 2062 (2020).
220. S. Karpf and B. Jalali, Optics Letters **44** (8), 1952-1955 (2019).
221. A. Vallmitjana, A. Dvornikov, B. Torrado, D. M. Jameson, S. Ranjit and E. Gratton, Methods and Applications in Fluorescence **8** (3), 035001 (2020).
222. M. J. Serafino, B. E. Applegate and J. A. Jo, Review of Scientific Instruments **91** (3), 033708 (2020).
223. M. J. Serafino and J. A. Jo, Biomedical Optics Express **14** (4), 1608-1625 (2023).
224. Y. Li, X. Xu, C. Zhang, X. Sun, S. Zhou, X. Li, J. Guo, R. Hu, J. Qu and L. Liu, Advanced Science **12** (7), 2410605 (2025).
225. K. Suhling, D. M. Davis and D. Phillips, Journal of Fluorescence **12** (1), 91-95 (2002).
226. Y. Teijeiro-Gonzalez, A. Crnjar, A. J. Beavil, R. L. Beavil and K. Suhling, Biophysical Journal **120**, 254–269 (2020).
227. K. Suhling, J. Siegel, P. Lanigan, S. Lévêque-Fort and P. French, Optics Letters **29** (6), 584-586 (2004).
228. Y. Gilad, P. Shweta, W. Yitzchak, A. Bar, D. Hamootal and F. Dror, Journal of Biomedical Optics **28** (5), 056001 (2023).
229. A. V. Gohar, R. Cao, P. Jenkins, W. Li, J. P. Houston and K. D. Houston, Biomedical Optics Express **4** (8), 1390-1400 (2013).
230. R. Cao, V. Pankayatselvan and J. P. Houston, Optics Express **21** (12), 14816-14831 (2013).

231. J. A. Steinkamp, T. M. Yoshida and J. C. Martin, Review of Scientific Instruments **64** (12), 3440-3450 (1993).
232. H. Kanno, K. Hiramatsu, H. Mikami, A. Nakayashiki, S. Yamashita, A. Nagai, K. Okabe, F. Li, F. Yin, K. Tominaga, O. F. Bicer, R. Noma, B. Kiani, O. Efa, M. Büscher, T. Wazawa, M. Sonoshita, H. Shintaku, T. Nagai, S. Braun, J. P. Houston, S. Rashad, K. Niizuma and K. Goda, Nature Communications **15** (1), 7376 (2024).
233. A. Mandelis, Physics Today **76** (10), 62-64 (2023).
234. H. Mikami, J. Harmon, H. Kobayashi, S. Hamad, Y. Wang, O. Iwata, K. Suzuki, T. Ito, Y. Aisaka, N. Kutsuna, K. Nagasawa, H. Watarai, Y. Ozeki and K. Goda, Optica **5** (2), 117-126 (2018).
235. J. Su, Y. Song, Z. Zhu, X. Huang, J. Fan, J. Qiao and F. Mao, Signal Transduction and Targeted Therapy **9** (1), 196 (2024).
236. O. I. Kolenc and K. P. Quinn, Antioxidants & Redox Signaling **30** (6), 875-889 (2017).
237. N. Ma, M. A. Digman, L. Malacrida and E. Gratton, Biomedical Optics Express **7** (7), 2441 (2016).
238. T. P. L. Ung, S. Lim, X. Solinas, P. Mahou, A. Chessel, C. Marionnet, T. Bornschlgl, E. Beaurepaire, F. Bernerd and A. M. Pena, Scientific Reports **11** (1), 1-15 (2021).
239. E. Sánchez-Ramírez, T. P. L. Ung, A. Alarcón del Carmen, X. del Toro-Ríos, G. R. Fajardo-Orduña, L. G. Noriega, V. A. Cortés-Morales, A. R. Tovar, J. J. Montesinos, R. Orozco-Solís, C. Stringari and L. Aguilar-Arnal, Journal of Cell Biology **221** (12), e202111137 (2022).
240. H. Nakamura and K. Takada, Cancer Science **112** (10), 3945-3952 (2021).
241. M. V. Shirmanova, A. I. Gavrina, T. F. Kovaleva, V. V. Dudenkova, E. E. Zelenova, V. I. Shcheslavskiy, A. M. Mozherov, L. B. Snopova, K. A. Lukyanov and E. V. Zagaynova, Scientific Reports **12** (1), 4476 (2022).
242. N. Paillon, T. P. L. Ung, S. Dogniaux, C. Stringari, C. Hivroz and A. August, Molecular Biology of the Cell **35** (1), ar11 (2024).
243. G. Oliveira and C. J. Wu, Nature Reviews Cancer **23** (5), 295-316 (2023).
244. N. G. Rummel and D. A. Butterfield, Antioxidants & Redox Signaling **36** (16-18), 1289-1305 (2022).
245. M. E. Migaud, M. Ziegler and J. A. Baur, Nature Reviews Molecular Cell Biology **25** (10), 822-840 (2024).
246. Y. Dong, S. Sameni, M. A. Digman and G. J. Brewer, Scientific Reports **9** (1), 11274 (2019).
247. C. A. Gómez, J. Sutin, W. Wu, B. Fu and M. A. Yaseen, PLoS ONE **13** (3), e0194578 (2018).
248. E. S. Jung, H. Choi and I. Mook-Jung, Molecular Neurodegeneration **20** (1), 37 (2025).
249. C. Lauro and C. Limatola, Frontiers in Immunology **11**, 493 (2020).
250. M. A. K. Sagar, J. N. Ouellette, K. P. Cheng, J. C. Williams, J. J. Watters and K. W. Eliceiri, Neurophotonics **7** (3), 035003 (2020).
251. Y. Zhao, J. Jin, Q. Hu, H.-M. Zhou, J. Yi, Z. Yu, L. Xu, X. Wang, Y. Yang and J. Loscalzo, Cell Metabolism **14** (4), 555-566 (2011).
252. P. Sun, H. Zhang, Y. Sun and J. Liu, Spectrochimica Acta Part A: Molecular and Biomolecular Spectroscopy **245**, 118919 (2021).
253. M. Li, C. Liu, W. Zhang, L. Xu, M. Yang, Z. Chen, X. Wang, L. Pu, W. Liu, X. Zeng and T. Wang, Journal of Materials Chemistry B **9** (46), 9547-9552 (2021).
254. Y. Zhao, K. Wei, F. Kong, X. Gao, K. Xu and B. Tang, Analytical Chemistry **91** (2), 1368-1374 (2018).
255. S. Kalinina, C. Freymueller, N. Naskar, B. von Einem, K. Reess, R. Sroka and A. Rueck, International Journal of Molecular Sciences **22** (11), 5952 (2021).

256. D. Gottlieb, B. Asadipour, P. Kostina, T. P. L. Ung and C. Stringari, Biological Imaging **3**, e21 (2023).
257. G. Rinaldi, M. Rossi and S. M. Fendt, WIREs Systems Biology and Medicine **10** (1), e1397 (2018).
258. J. J. Rennick, C. J. Nowell, C. W. Pouton and A. P. R. Johnston, Nature Communications **13** (1), 6023 (2022).
259. Y. Won, B. Park, I. Kim and S. J. H. Lee, Heliyon **2** (8), e00139 (2016).
260. J. M. Buschhaus, B. Humphries, K. E. Luker and G. D. Luker, in *Cells* (2018), Vol. 7.
261. A. C. E. Shibata, H. H. Ueda, K. Eto, M. Onda, A. Sato, T. Ohba, J. Nabekura and H. Murakoshi, Nature Communications **12** (1), 751 (2021).
262. R. Pal, T. M. Lwin, M. Krishnamoorthy, H. R. Collins, C. D. Chan, A. Prilutskiy, M. P. Nasrallah, T. H. Dijkhuis, S. Shukla, A. L. Kendall, M. S. Marshall, S. A. Carp, Y. P. Hung, A. R. Shih, M. Martinez-Lage, L. Zukerberg, P. M. Sadow, W. C. Faquin, B. V. Nahed, A. L. Feng, K. S. Emerick, J. S. D. Mieog, A. L. Vahrmeijer, K. Rajasekaran, J. Y. K. Lee, K. S. Rankin, S. Lozano-Calderon, M. A. Varvares, K. K. Tanabe and A. T. N. Kumar, Nature Biomedical Engineering **7** (12), 1649-1666 (2023).
263. S. S. Hou, J. Yang, J. H. Lee, Y. Kwon, M. Calvo-Rodriguez, K. Bao, S. Ahn, S. Kashiwagi, A. T. N. Kumar, B. J. Bacskai and H. S. Choi, Nature Biomedical Engineering **7** (3), 270-280 (2023).
264. C. Zhong, S. Arai and Y. Okada, Cell Reports Methods **4** (11), 100902 (2024).
265. Y. Li, Q. Zhang, Q. Wang, X. Wang, J. Wang, X. Zhu, X. Chen, S. Wang, X. Sun and H. Zhou, Analytical Chemistry **96** (8), 3535-3543 (2024).
266.H. Farrants, Y. Shuai, W. C. Lemon, C. Monroy Hernandez, D. Zhang, S. Yang, R. Patel, G. Qiao, M. S. Frei, S. E. Plutkis, J. B. Grimm, T. L. Hanson, F. Tomaska, G. C. Turner, C. Stringer, P. J. Keller, A. G. Beyene, Y. Chen, Y. Liang, L. D. Lavis and E. R. Schreiter, Nature Methods **21** (10), 1916-1925 (2024).
267. K. Joron, J. O. Viegas, L. Haas-Neill, S. Bier, P. Drori, S. Dvir, P. S. L. Lim, S. Rauscher, E. Meshorer and E. Lerner, Nature Communications **14** (1), 4885 (2023).
268. S. M. Levchenko, A. Pliss, X. Peng, P. N. Prasad and J. Qu, Light-Science & Applications **10** (1), 224 (2021).
269. H. Gao, C. Kam, T. Y. Chou, M.-Y. Wu, X. Zhao and S. Chen, Nanoscale Horizons **5** (3), 488-494 (2020).
270. A. S. Kashirina, I. López-Duarte, M. Kubánková, A. A. Gulin, V. V. Dudenkova, S. A. Rodimova, H. G. Torgomyan, E. V. Zagaynova, A. V. Meleshina and M. K. J. S. r. Kuimova, Scientific reports **10** (1), 1-12 (2020).
271. Z. Huang, Y. Wang, F. Lin, Z. Luo, H. Xu, N. Alifu, J. Li, X. Weng, J. Song, L. Liu, Y. Chen and J. Qu, Matter **8**, 102102 (2025).
272. J. Ma, R. Sun, K. Xia, Q. Xia, Y. Liu and X. Zhang, Chemical Reviews **124** (4), 1738-1861 (2024).
273. X. Qin, T. Li, S. Li, H. Yang, C. Wu, C. Zheng, F. You and Y. Liu, Cellular & Molecular Immunology **17** (11), 1186-1187 (2020).
274. C. Paviolo, A. Clayton, S. Mcarthur and P. Stoddart, Journal of microscopy **250** (3), 179-188 (2013).
275. C. Ward, J. Meehan, M. E. Gray, A. F. Murray, D. J. Argyle, I. H. Kunkler and S. P. Langdon, Exploration of Targeted Anti-tumor Therapy **1** (2), 71-100 (2020).
276. A. Orte, J. M. Alvarez-Pez and M. J. Ruedas-Rama, ACS nano **7** (7), 6387-6395 (2013).
277. K. Zheng, L. Bard, J. P. Reynolds, C. King, Thomas P. Jensen, Alexander V. Gourine and Dmitri A. Rusakov, Neuron **88** (2), 277-288 (2015).
278. D. A. Fletcher and R. D. Mullins, Nature **463** (7280), 485-492 (2010).

279. D. Eisner, E. Neher, H. Taschenberger and G. Smith, Physiological Reviews **103** (4), 2767-2845 (2023).
280. M. I. Angelova, A.-F. Bitbol, M. Seigneuret, G. Staneva, A. Kodama, Y. Sakuma, T. Kawakatsu, M. Imai and N. Puff, Biochimica et Biophysica Acta -Biomembranes **1860** (10), 2042-2063 (2018).
281. I. Tortorella, C. Argentati, C. Emiliani, F. Morena and S. Martino, Cells **11** (19), 3093 (2022).
282. M. K. Mofrad, N. Abdul-Rahim, H. Karcher, P. Mack, B. Yap and R. Kamm, Acta biomaterialia **1** (3), 281-293 (2005).
283. X. Liang, Y. Zhao, J. Yan, Q. Zhang, T. D. James and W. Lin, Proceedings of the National Academy of Sciences **121** (41), e2316450121 (2024).
284. Y. Wu, F. Li, Y. Wu, H. Wang, L. Gu, J. Zhang, Y. Qi, L. Meng, N. Kong, Y. Chai, Q. Hu, Z. Xing, W. Ren, F. Li and X. Zhu, Nature Communications **15** (1), 2341 (2024).
285. W. J. Van Blitterswijk, B. W. Van der Meer and H. Hilkmann, Biochemistry **26** (6), 1746-1756 (1987).
286. M. K. Kuimova, G. Yahioglu, J. A. Levitt and K. Suhling, Journal of the American Chemical Society **130** (21), 6672–6673 (2008).
287. M. Kubánková, P. A. Summers, I. López-Duarte, D. Kiryushko and M. K. Kuimova, ACS Applied Materials & Interfaces **11** (40), 36307-36315 (2019).
288. L. E. Shimolina, A. A. Gulin, M. Paez-Perez, I. López-Duarte, I. N. Druzhkova, M. M. Lukina, M. V. Gubina, N. J. Brooks, E. V. Zagaynova, M. K. Kuimova and M. V. Shirmanova, Journal of Biomedical Optics **25** (12), 126004 (2020).
289. S. Das, A. Batra, S. Kundu, R. Sharma and A. Patra, Chemical Science **15** (1), 102-112 (2024).
290. Y. Ouyang, Y. Liu, Z. M. Wang, Z. Liu and M. Wu, Nano-Micro Letters **13** (1), 133 (2021).
291. N. R. W. Cleland, S. I. Al-Juboori, E. Dobrinskikh and K. D. Bruce, Journal of Neuroinflammation **18** (1), 248 (2021).
292. X. Liu, L. Liu, X. Hu, S. Zhou, R. Ankri, D. Fixler and Z. Xie, Nano Research **11** (3), 1262-1273 (2018).
293. M. W. Conklin, P. P. Provenzano, K. W. Eliceiri, R. Sullivan and P. J. Keely, Cell biochemistry biophysics **53** (3), 145-157 (2009).
294. J. Lu, M. Tan and Q. Cai, Cancer Letters **356** (2), 156-164 (2015).
295. M. Lukina, K. Yashin, E. E. Kiseleva, A. Alekseeva, V. Dudenkova, E. V. Zagaynova, E. Bederina, I. Medyanic, W. Becker, D. Mishra, M. Berezin, V. I. Shcheslavskiy and M. Shirmanova, Frontiers in Oncology **11**, 666059 (2021).
296. C. Li, J. Shklover, M. Parvizi, B. E. Sherlock, A. Alfonso Garcia, A. K. Haudenschild, L. G. Griffiths and L. Marcu, Annals of Biomedical Engineering **46** (11), 1870-1881 (2018).
297. P. J. Tadrous, J. Siegel, P. M. W. French, S. Shousha, E. N. Lalani and G. W. H. Stamp, The Journal of Pathology **199** (3), 309-317 (2003).
298. A. I. Herrando, L. M. Fernandez, J. Azevedo, P. Vieira, H. Domingos, A. Galzerano, V. Shcheslavskiy, R. J. Heald, A. Parvaiz, P. G. da Silva, M. Castillo-Martin and J. L. Lagarto, Scientific Reports **14** (1), 24575 (2024).
299. M. B. Różanowska, Antioxidants **12** (12), 2111 (2023).
300. Y. Yan, F. Xing, J. Cao, Y. Hu, L. Li, Z. Gao, H. Jia, K. Miao, F. Shao, C.-X. Deng, K. Q. Luo, L. T. o. Lee and T.-M. Liu, Redox Biology **59**, 102578 (2023).
301. R. Cao, H. K. Wallrabe and A. Periasamy, Journal of Biomedical Optics **25** (1), 1 (2020).

302. L. Shimolina, A. Gulin, A. Khlynova, N. Ignatova, I. Druzhkova, M. Gubina, E. Zagaynova, M. K. Kuimova and M. Shirmanova, International Journal of Molecular Sciences **24** (15), 12186 (2023).
303. F. Gorka, S. Daly, C. M. Pearson, E. Bulovaite, Y. P. Zhang, A. Handa, S. G. Grant, T. N. Snaddon, L.-M. Needham and S. F. Lee, The Journal of Physical Chemistry B **125** (50), 13710-13717 (2021).
304. T. Luo, Y. Lu, S. Liu, D. Lin and J. Qu, Analytical chemistry **89** (17), 9224-9231 (2017).
305. G. Weitsman, P. R. Barber, L. K. Nguyen, K. Lawler and T. Ng, Oncotarget **7** (32), 51012-51026 (2016).
306. Z. Chen, L. Huang, D. Gao, Z. Bao, D. Hu, W. Zheng, J. Chen, J. Liao, H. Zheng and Z. Sheng, Advanced Science **12** (5), 2411272 (2025).
307. A. Sánchez-Hernández, C. M. Polleys and I. Georgakoudi, Biomedical Optics Express **14** (10), 5238 (2023).
308. A. Alfonso-Garcia, S. N. Anbunesan, J. Bec, H. S. Lee, L.-W. Jin, O. Bloch and L. Marcu, Biomedical Optics Express **14** (5), 2196-2208 (2023).
309. E. A. Shirshin, Y. I. Gurfinkel, A. V. Priezzhev, V. V. Fadeev, J. Lademann and M. E. Darvin, Scientific Reports **7** (1), 1171 (2017).
310. Z. Huang, Y. Wang, F. Lin, Z. Luo, H. Xu, N. Alifu, J. Li, X. Weng, Y. Sun, J. Song, L. Liu, Y. Chen and J. Qu, Matter **8** (5), 102102 (2025).
311. W. Liang, D. Chen, H. Guan, H.-C. Park, K. Li, A. Li, M.-J. Li, I. Gannot and X. Li, ACS Photonics **9** (12), 4017-4029 (2022).
312. B. W. Weyers, A. C. Birkeland, M. A. Marsden, A. Tam, J. Bec, R. P. Frusciante, D. Gui, A. F. Bewley, M. Abouyared, L. Marcu and D. G. Farwell, Head & Neck **44** (8), 1765-1776 (2022).
313. K. Young, E. Ma, S. Kejriwal, T. Nielsen, S. S. Aulakh and A. C. Birkeland, Cancers **14** (14), 3416 (2022).
314. C. A. Gómez, Neurophotonics **5** (04), 1 (2018).
315. L. Shimolina, E. Potekhina, I. Druzhkova, M. Lukina, V. Dudenkova, V. Belousov, V. Shcheslavskiy, E. Zagaynova and M. Shirmanova, Biophysical Journal **121** (7), 1156-1165 (2022).
316. G. L. Coté, S. Lee, Y. Won, J. Lee, B. Park and B. Kim, in *Optical Diagnostics and Sensing XIX: Toward Point-of-Care Diagnostics* (2019).
317. M. Hammer, D. Schweitzer, S. Richter and E. Königsdörffer, Physiological measurement **26** (4), N9 (2005).
318. S. Rodimova, V. Elagin, M. Karabut, I. Koryakina, A. Timin, V. Zagainov, M. Zyuzin, E. Zagaynova and D. Kuznetsova, Cells **10** (11), 2894 (2021).
319. Z. Xie, C. Meng, D. Yue, L. Xu, T. Mei and W. Zhang, Opto-Electronic Science **4** (5), 240027 (2025).